Dissertation

for Doctor of Philosophy

Carnot Battery System by using a Fluidized Bed Integrated with a Biomass Power Plant for Renewable Energy Utilization

Department of Chemical Engineering

Graduate School of Engineering

Tokyo University of Agriculture and Technology

by **Takayuki UCHINO**

directed by Chihiro FUSHIMI

March, 2023

Contents

Chapter 1

Introduction

1.1. Energy Problem

1.1.1. Renewable Energy

Figure 1.1 shows primary energy consumption in the world [1]. The primary energy usage has increased stably and the percentage of the organization for economic co-operation and development (OECD) countries decreased because the world population keeps increasing [2] and the economics keeps developing, in particular, the developing countries. It is required to increase the primary energy supply and establish effective energy conservation technologies.

In addition, CO_2 reduction has been required to alleviate the global warming. Figure 1.2 shows the world electricity generation [1]. Although the fossil fuels (coal and natural gas) have been largely used, recent years have witnessed the growing usage of renewable energy as a viable replacement of fossil fuels to reduce CO_2 emissions [1]. United Nations has reported that renewable energy is energy derived from natural sources that are replenished at a higher rate than they are consumed, for example, solar energy, wind energy, hydropower, ocean energy, bioenergy, geothermal energy [3]. Figure 1.3 shows the power generation by renewables [1]. Although the geothermal and biomass power generation was higher electricity generation than wind and solar energy power generation, wind and solar energy utilizations are dramatically expanded. Wind and solar energy sources feature supply fluctuations of the order of several seconds [4] and are therefore denoted as variable renewable energy (VRE) sources.

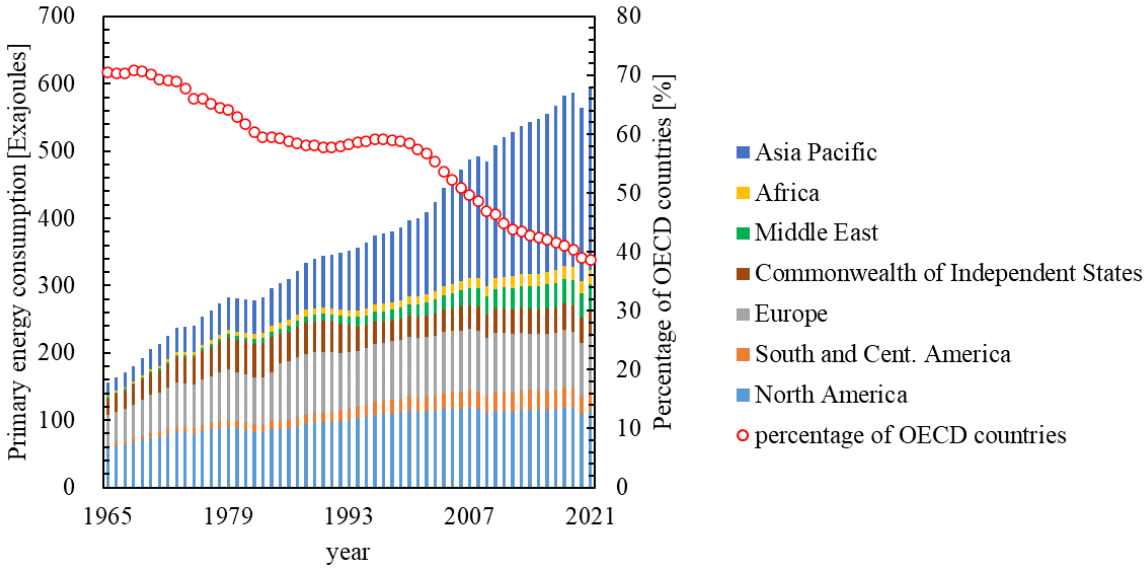

Figure 1.1 Primary energy consumption

Figure 1.1 Primary energy consumption (1965–2021) [1]

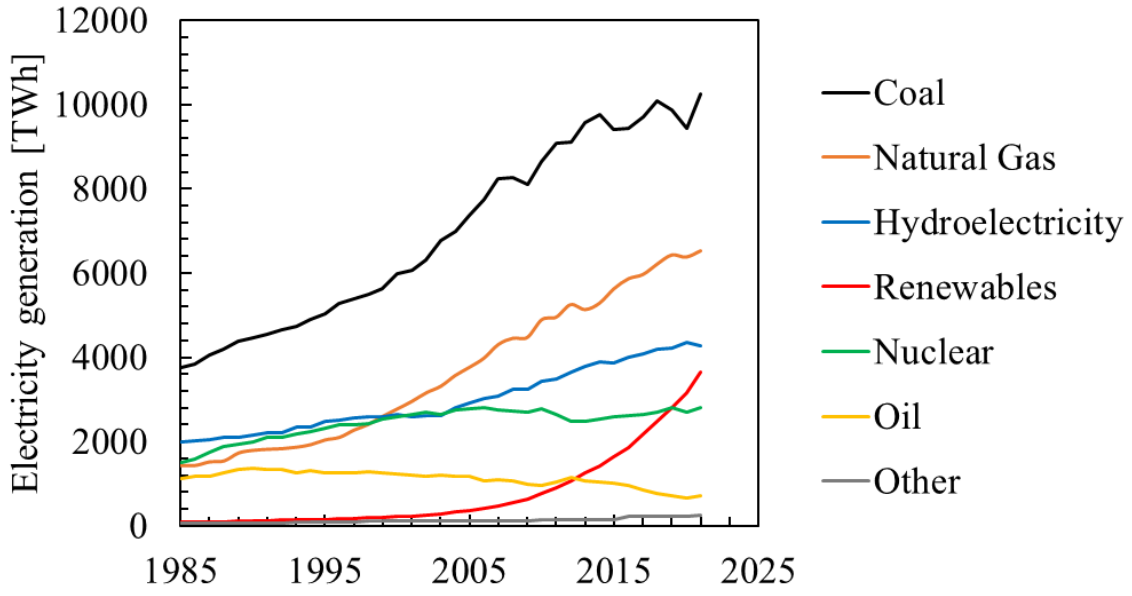

Figure 1.2 Electricity generation in the world (1985–2021) [1]

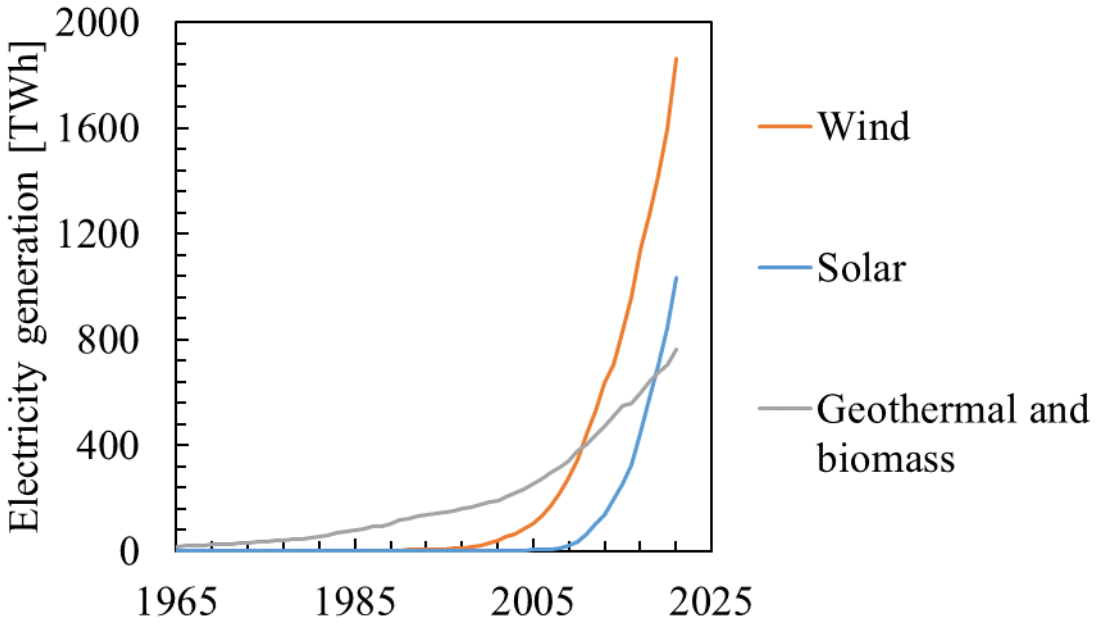

Figure 1.3 Electricity generation from renewables in the world (1965–2021) [1]

1.1.2. Power Generation by Variable Renewable Energy

Figure 1.4 shows the power generation variability in the area supplied by The Tokyo Electric Power Company in April (plot interval is 1 h). It is found that the power generation is fluctuated because their supply is intermittent and depending on climate. Figures 1.5 (a) and (b) show the seasonal inclination of wind and solar power generation in the area supplied by The Tokyo Electric Power Company, respectively. Wind power generation decreases in summer and increases in winter. Solar power generation during summer has wider than that of winter. However, the peak power generation of summer is lower than that of winter. The reason is that the solar power generation is inhibited at higher temperatures [5].

In the power generation, the supply and demand should be balanced at all times due to the electricity characteristics. If the balance is lost, it may lead to a blackout. If VRE power generation increases, a possibility of the blackout also increases. The International energy agency (IEA) reported that the measures to maintain cost-effectiveness and reliability of the power system differ over four stages (note that there are six stages) of VRE deployment [6]. In the report, phase three that the uncertainly and fluctuation of the power supply becomes large requires the power generation flexibility, and phase four that VRE accounts for almost or all power supply requires the power system stability. Although the power generation from VRE is fluctuated, the power generation cost by using VRE is low because there is no fuel cost. Thus, VRE is utilized preferentially. In Japan, only base load power has priority over VRE when it is necessary to restrict the power generation [7].

In the above situation, the net load that is the difference between forecasted load and expected electricity generation from VRE [8] is an important indicator, and some time profiles in a day are shown in Figures 1.5 (c), 1.6, and 1.7. The net load has generally two peaks in the morning and evening [8] because people start moving, solar power generation does not work in the morning and in the evening, and the decrease of solar power generation coincides with the increase of demand as people go home in the evening. In particular, the selling price of

electricity in the evening is high [9–11]. Figure 1.5 (c) shows the seasonal net load in the area supplied by The Tokyo Electric Power Company. The net load of winter has more dramatic change than that of summer. In winter, the room heating decreases in a daytime. This leads that the net load change of winter is larger than that of summer. In the future, the increase of solar power generation leads to low net load in a daytime (see Figure 1.7), and the net load may approach to zero. Note that the net load is not negative value because the supply and demand of the electricity must be balanced. However, the power generation is restricted. In the situation, the electricity cost will be free in a daytime. On the other hand, the net load dramatically increases in the evening due to the dramatic decrease of solar power generation. Thus, the electricity cost also increases in the evening. This tendency is predicted to become larger because of the spread of the solar power generation. However, in this situation, a possibility of blackout increases when the power supply does not meet the power demand. At present, the supply and demand are mainly adjusted by thermal power plants and hydroelectricity power generations. Above all, thermal power plants are required to increase the VRE usage to balance the problem of the VRE fluctuation although thermal power plants release many carbon dioxides. To solve the problem, the other adjusting power generation is necessary, and the energy storage technology is expected to be promising.

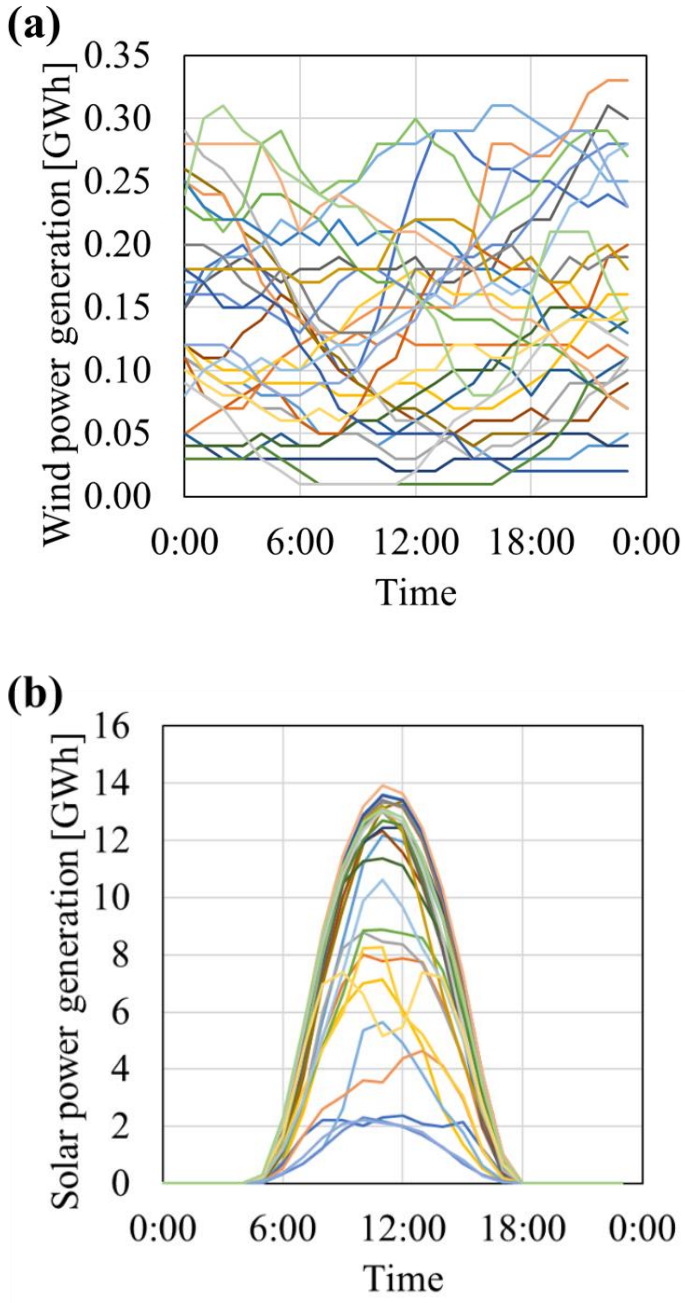

Figure 1.4 (a) Wind and (b) solar power generation of each day in the area supplied by Tokyo Electric Power Company (April, 2021) [12]

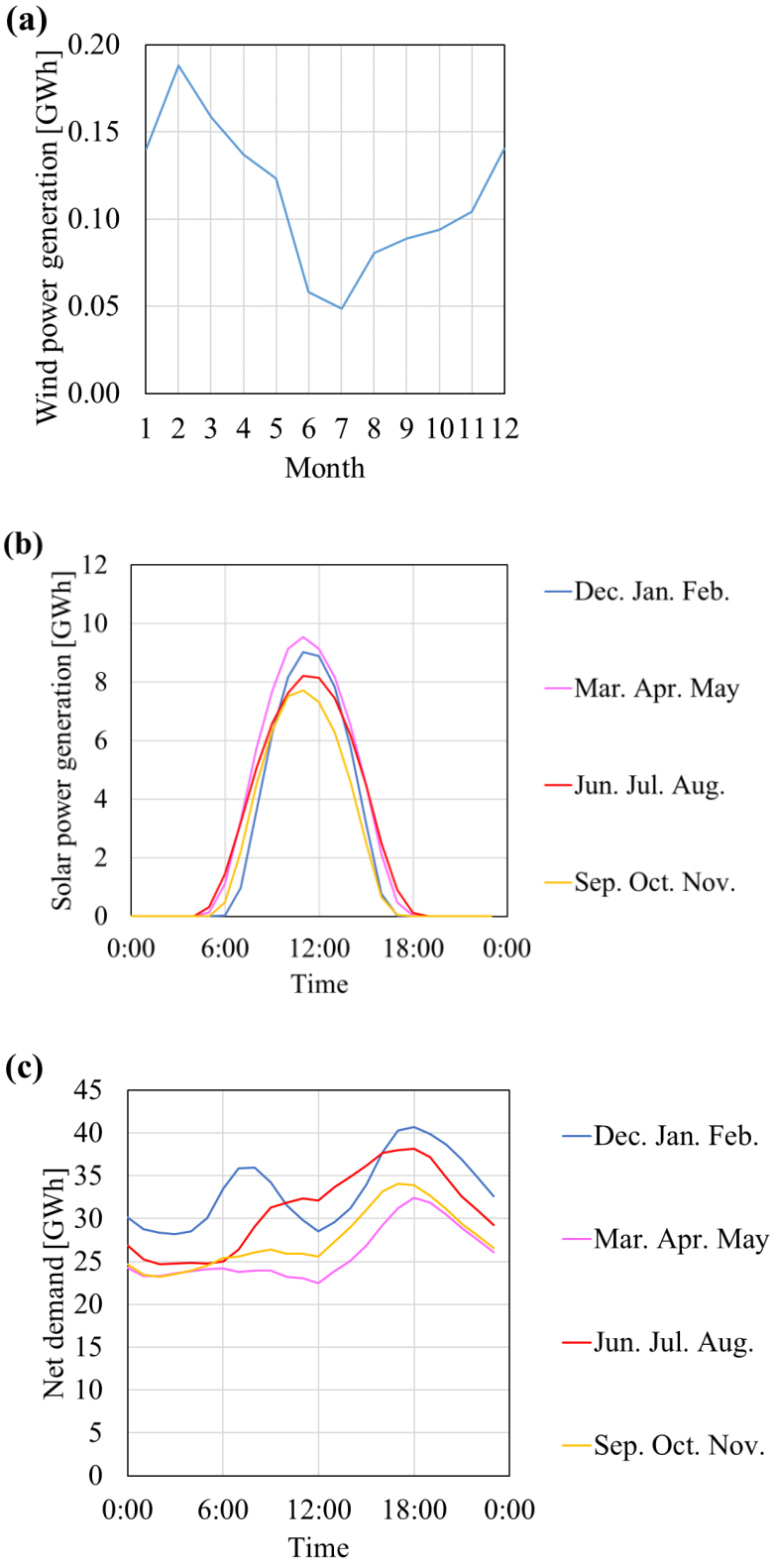

Figure 1.5 Seasonal (a) wind and (b) solar power generation and (c) net load in the area supplied by Tokyo Electric Power Company (2021) [12]

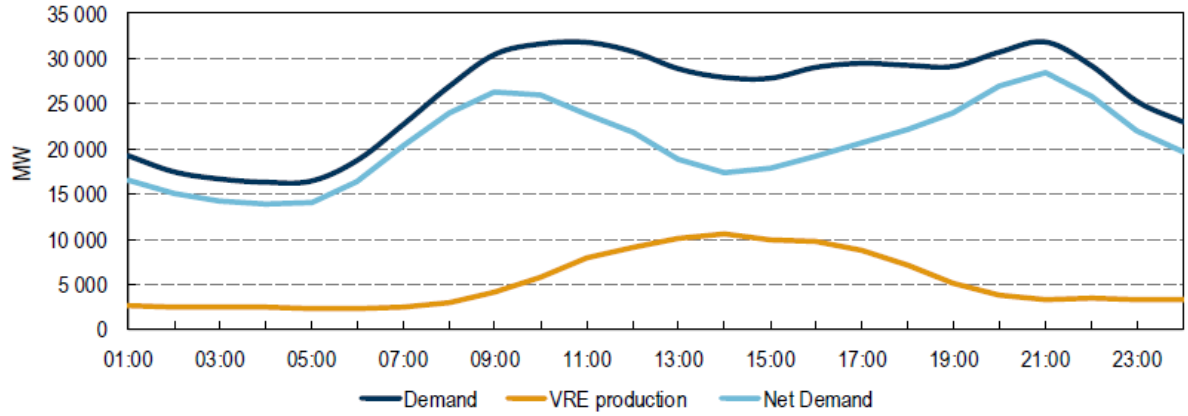

Figure 1.6 Demand, VRE power generation, and net demand (the same for net load) in Italy on Apr. 13, 2016 [6]

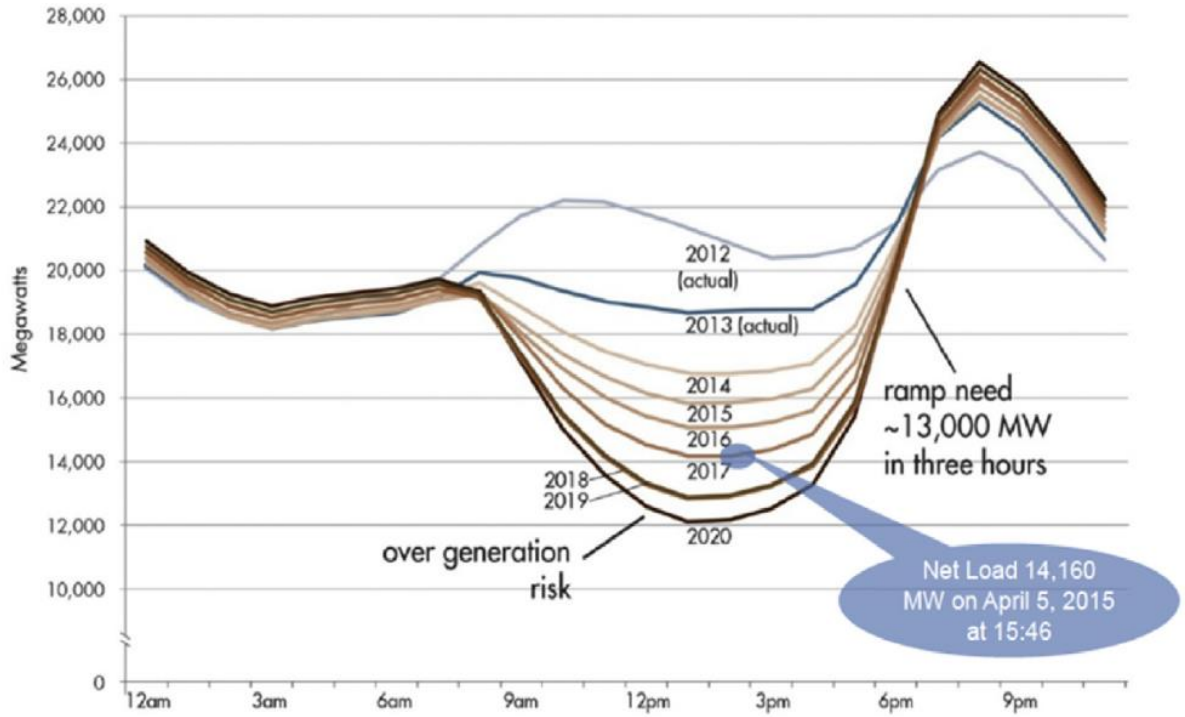

Figure 1.7 Net load of California in typical spring day (brown curves were predicted in 2013)

Reprinted with permission from ref. [8]. Copyright (2017) Elsevier B.V.

1.2. Energy Storage

1.2.1. Electric Energy Storage and Thermal Energy Storage

The energy storage technology is mainly classified as electric and thermal energy storages (EES and TES, respectively). The detailed classification is summarized in Figure 1.8. In addition, medium and large size energy storage systems are summarized in Table 1.1 [13]. These methods are chosen as the backup power sources and the leveling systems by considering the capacity, the startup time, the discharging time, etc [14]. EES is classified as mechanical, chemical, electrochemical, superconducting magnetic, and cryogenic energy storages. Pumped hydro energy storage has already been used as a large-scale and adjusting power generation method. Compressed air energy storage is also used as a large-scale energy storage method. Batteries have various types such as NaS, Li-ion, etc., and used for various aims by considering their characteristics [15]. Flywheels and capacitors have been used as small-scale energy storage methods, and flywheels are used for the second-order leveling systems. TES is classified as physical (sensible and latent) and chemical (sorption and thermochemical) energy storages. TES systems whose objective of the energy storage is power generation, are called as Carnot batteries [16]. TES based on sorption is not generally used as Carnot batteries because their operating temperatures are too low for power generation, but used as thermal energy usage [17–19]. Thus, Carnot batteries can be divided into those relying on sensible, latent, and thermochemical heat storage (TCS), with the related characteristics listed in Tables 1.1 and 1.2. Carnot batteries will provide the benefit of low-cost electricity storage and include on three processes, namely 1) electricity to heat conversion, 2) thermal (high-temperature) energy storage, and 3) heat to electricity conversion (i.e., power generation). In Carnot batteries, the conversion of electricity to heat results in a low (compared to that of secondary batteries) round-trip efficiency (< 50%) that is strongly temperature-dependent [20]. However, Carnot batteries employ inexpensive and abundant heating media and therefore have a relatively large energy storage capacity and lower cost than the others (see Table 1.2). In sensible heat storage,

solid and liquid are generally used because the heat conductivity of gas is low. In latent heat storage, the heat of condensing heat, melting heat, etc., is used, and the used materials are called as phase change material (PCM). Generally, solid-liquid and solid-solid changes are used because the volume change of the materials due to the phase change is low. Carnot batteries utilizing sensible and latent heat storages provide the benefits of simple processes [21] and low cost but suffer from low energy densities. Above all, this study focuses on TCS. Table 1.2 shows the advantages and disadvantages, and the details will be described in the next section.

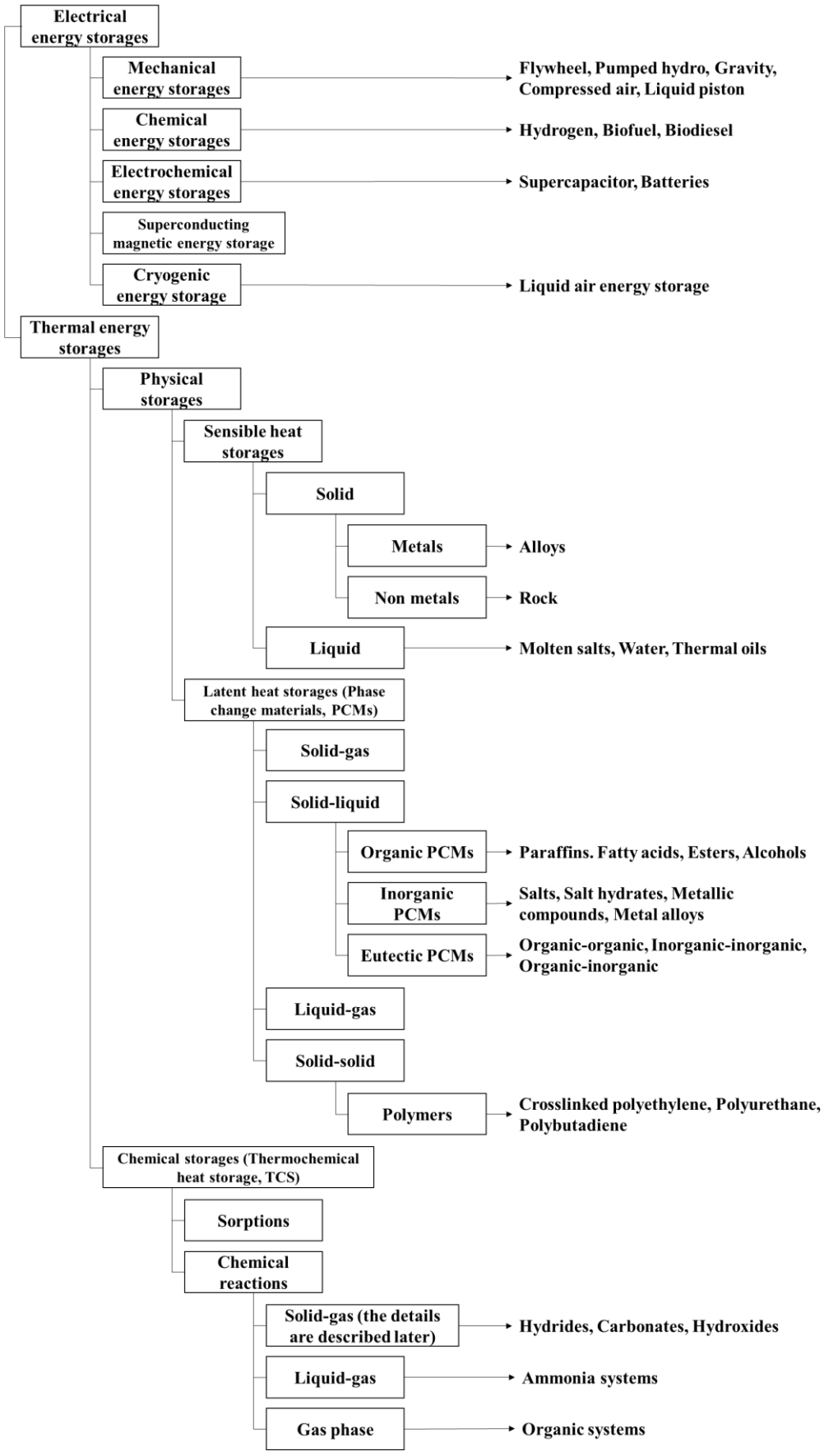

Figure 1.8 Classification of energy storage technologies [15,22]

Table 1.1 The medium and larger energy storage systems

Reprinted with permission from ref. [13]. Copyright (2018) Elsevier B.V.

Storage technologies	**Pumped hydro**	**Compressed air**	**Batteries**	**Sensible heat**	**Latent heat**	**TCS**
Energy storage form	Mechanical	Mechanical	Electro-chemical	Thermal	Thermal	Thermo-chemical
Efficiency [%]	50–85 (electrical)	27–70 (electrical)	75–95 (electrical)	50–90 (thermal)	75–90 (thermal)	75–100 (thermal)
Initial capital cost [USD/kW]	500–4600	500–1500	300–3500	3400–4500	6000–15000	1000–3000
Energy cost [USD/kWh]	80–100	50–100	150–2500	0.1–13	10–56	8–100
Durability [years]	40–100	20–100	3–20	10–30+	10–30+	10–30+
Durability [cycles]	10000–30000	8000–12000	1000–10000	2000–14600	2000–14600	2000–14600
Energy storage density [kWh/m^3]	0.5–1.5	3–6	15–600	25	100	< 500
Energy storage density [kWh/t]	0.5–1.5	30–60	10–250	10–50	50–150	< 120–250
Storage capacity [MW]	100–5000	1–400	0.001–50	0.1–300	0.1–300	0.1–300

Table 1.2 The Carnot batteries comparison among sensible, latent, and TCS

Reprinted with permission from ref. [23]. Copyright (2017) Elsevier B.V.

Technology	**Sensible**	**Latent**	**TCS**
Cost	Low cost materials	Low cost materials	Low cost materials High design and installation costs for reactors
Energy density	Low	Medium	High
Occupied area	High	Medium	Low
Temperature for storage	High	High	Low (ambient temperature)
Technology feedback	Large experimental feedback Majority of CSP[*1] plants in operation	More R & D work needed	No feedback
Flexibility charge/discharge	Switch within a short time	Switch within a short time	Switch within a medium time
Heat transfer	Quite good	Slow	Slow
Advantages	● Large experimental feedback ● Easy implementation	● Constant charge/discharge temperatures ● Medium energy density	● Long period storage without heat losses ● High energy density
Disadvantages	● Heat losses during storage ● Low energy density ● High freezing point for liquid materials ● Variable discharging temperature	● Low thermal conductivity ● Solid deposits on the PCM/heat exchanger area	● Incomplete reversibility ● Storage of gaseous products ● Necessity of heat and mass transfer enhancement

[*1]CSP: Concentrated Solar Power

1.2.2. Thermochemical Heat Storage (TCS)

In TCS, a reversible reaction (eq. (1.1)) that the reaction enthalpy of the forward step is the same as that of the backward step is used for the energy storage. The energy is stored as the chemical heat.

$A + \Delta H_r \rightleftarrows B + C$ (ΔH_r: reaction enthalpy) (1.1)

Figure 1.9 shows the energy flow of a Carnot battery with a TCS system. The electricity generated by thermal, solar, wind, and other power plants is supplied into power grid and used in houses and offices, etc. In charging time, the surplus and fluctuated power from VRE is converted into (high-temperature) heat and supplied to the TCS system. The heat is used for the endothermic reaction (the forward step reaction of eq. (1.1)), and A change to B and C. B and C are separated, and stored separately. In discharging time, B and C re-contact, and the exothermic reaction (the backward step reaction of eq. (1.1)) occurs. The reaction heat is converted into the electricity. The electricity returns to the power grid and is used for meeting the supply and demand.

TCS are required the following characteristics [24,25].

① Proper reaction temperature

② High reaction enthalpy

③ Fast reaction rate and high conversion

④ No byproducts (high reversibility)

⑤ Easy separation of products (B and C) and safe storage

⑥ No toxicity, no corrosiveness, no flammability, and no explosiveness

⑦ Cyclability and high stability (no agglomeration and no sintering)

⑧ Small volume change by reaction

⑨ Ease of scale-up, material abundance, and low material cost

The classification of TCS is as follows [15,22,24,26,27].

- Gas-gas reaction
  - Ammonium
  - Organic
  - Sulfur
- Liquid-gas reaction
  - Isopropanol/acetone
  - Ammonium hydrosulfide
- Solid-gas reaction
  - Metal hydride
  - Redox reaction
  - Carbohydrate
  - Hydroxide
  - Ammonium salt
  - Metal sulfide

The relation between the reaction enthalpy and turning temperature (that is the turning point between forward and backward step reactions) of some reactions are shown in Figure 1.10. In TCS, solid-gas reactions are generally used because separation of the products is easy. Figure 1.10 shows that metal oxides, carbonates, and sulfates have high turning temperatures and the reaction enthalpies. A high operating temperature leads to high heat loss and high capital cost for material resistance. Considering general usage, the toxic or corrosive components (e.g., sulfur dioxide and ammonia) should not be used. Note for hydroxides, H_2O is stored in the liquid state, and this leads to a smaller storage tank (generally, pure H_2O is used in a closed system). Thus, hydroxides are chosen in this study. Among hydroxides, $Ca(OH)_2$,

$Mg(OH)_2$, $Sr(OH)_2$, etc., are usually used for TCS. The present work focused on TCS based on the $Ca(OH)_2$ (s) to CaO (s) conversion [28], which can be represented as eq. (1.2).

$$CaO(s) + H_2O(g) \rightleftarrows Ca(OH)_2(s),\ \Delta H_r = -104\ \text{kJ/mol} \quad (1.2)$$

The dehydration-hydration cycle offers the benefits of high volumetric energy density (195 kWh_{th}/m^3-$Ca(OH)_2$-bulk), good reversibility, appropriate operating temperatures and pressures (400–600 °C at 0.1 MPa, see Figure 1.11), and good material availability and non-toxicity [29]. The reaction temperatures are higher than those of other hydroxides system such as $Mg(OH)_2$, leading to higher heat transfer rate because the temperature differences are larger. Figure 1.11 shows the relation between pressure and temperature at equilibrium. The equation is as follows (eq. (1.3)).

$$P_{\text{eq}}\ [\text{kPa}] = 2.0 \times 10^8 \exp\left(-\frac{11607}{T_{\text{eq}}\ [\text{K}]}\right) \quad (1.3)$$

where P_{eq} is equilibrium pressure of steam at T_{eq}, T_{eq} is equilibrium temperature. Figure 1.11 indicates that low steam pressure is preferable during dehydration. Nitrogen or air may be used for decreasing the steam partial pressure. On the other hand, during hydration, high steam pressure achieves high reaction temperature. Thus, TCS can be mainly controlled by the steam pressure and temperature.

The TCS cycle that uses a fluidized bed as a reactor is shown in Figure 1.12. Note the details will be described in section 1.3.2. There are a reactor and a water storage tank for the TCS cycle. Water is compressed and heated, and steam is generated. The electricity of the heater is supplied by VRE. The steam is used as fluidizing and reactant gas for a fluidized bed reactor. The reactor temperature become around 540 °C in charging time and around 450 °C in discharging time (in the case of around ambient pressure). The heat of outlet steam from the reactor is recovered, and the steam or water returns to the water tank.

TCS cycle has some types [30], first, which are open and closed modes. In an open mode, humid air at near ambient pressure is used. This mode is simple and requires low capital

cost. However, humid air contains impurity. For example, CO_2 has a negative influence on $CaO/Ca(OH)_2$ system because $CaCO_3$ is produced by a side-reaction. On the other hand, in a closed mode, pure gas is used. This mode provides better control of the operation conditions, and it is preferable for reaction kinetics. The problems are airtightness and accumulation of impurities. Second, integrated and separate reactors types. In the case of an integrated reactor type, exothermic and endothermic reactions occur in the same reactor. Note that the reactor is also used as a storage tank. In many studies of an integrated reactor type, the reactor contains a heat exchanger for recovery of the reaction heat, leading to low energy storage density. In the case of separate reactor type, there are multiple tanks such as reactors and solid storage tanks. In this type, it is necessary to transfer the solid reactants. This requires the mechanical strength of the solids. If solid reactants do not have sufficient mechanical strength, the cycling stability dramatically decreases. Although there are technical problems, it is possible to operate this type system at steady state, which can generate power constantly. This study adopts closed and integrated reactor type, and the details of the process will be described in Chapters 3 and 4.

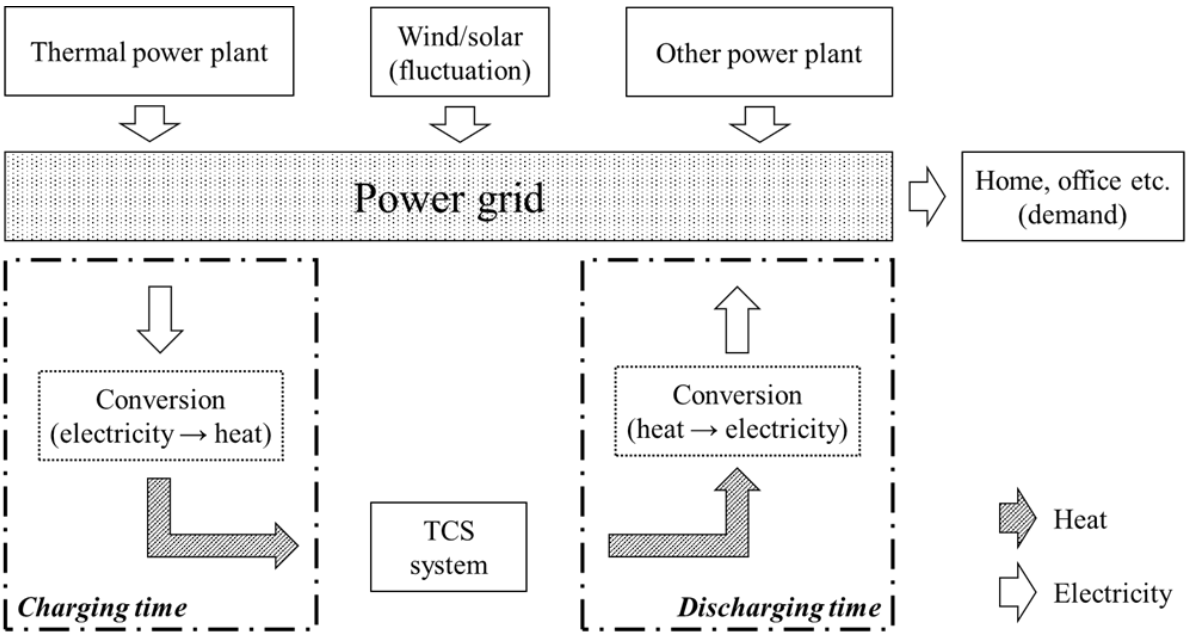

Figure 1.9 Energy flow concept of a Carnot battery with a TCS system

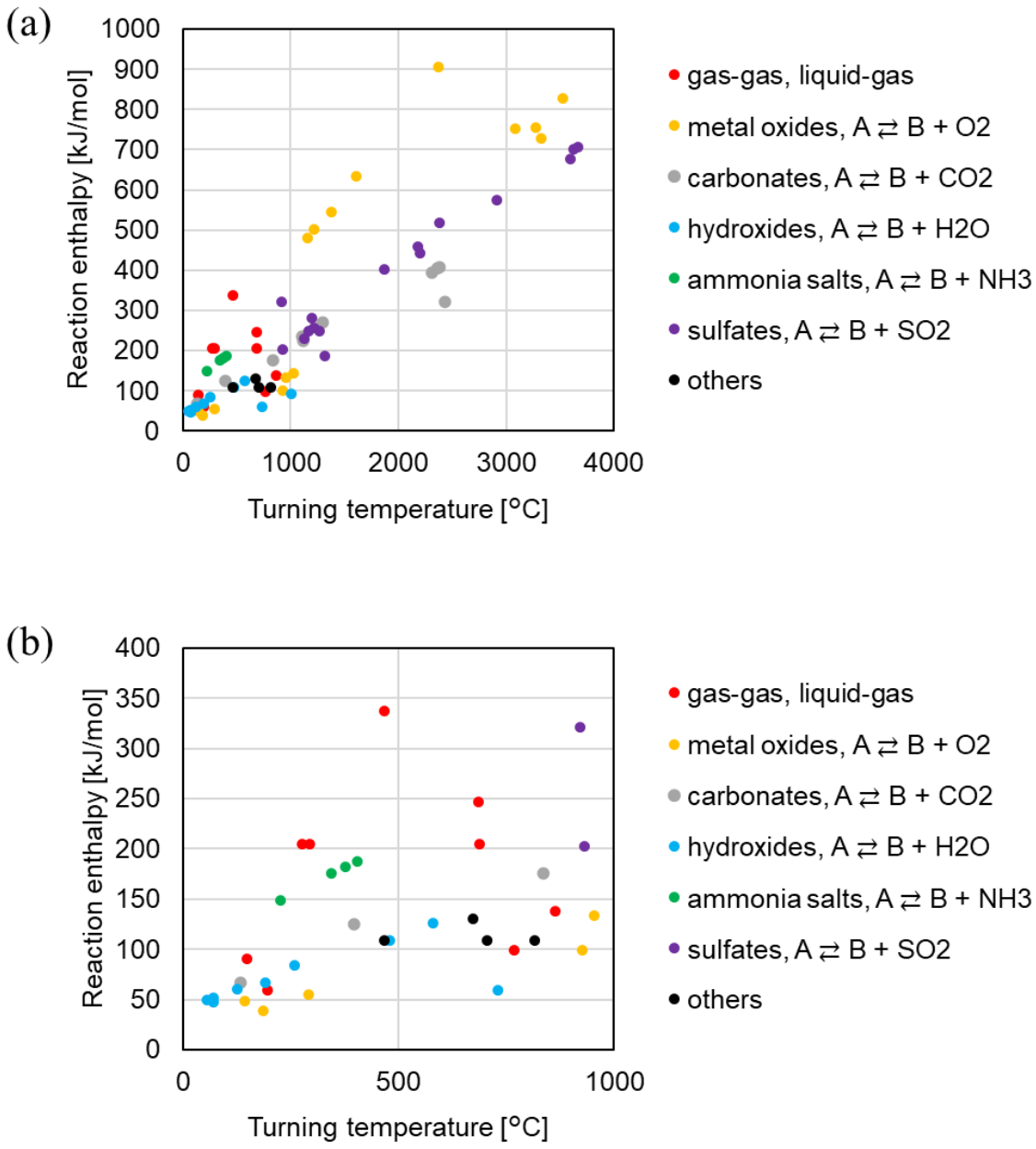

Figure 1.10 The relation between reaction enthalpy and turning temperature (b) enlarged figure from 0 to 1000 °C [24,26,31,32]

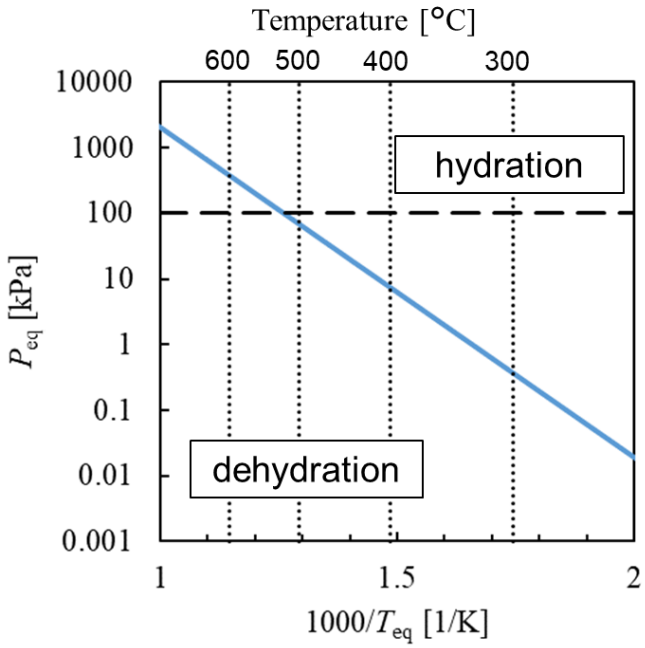

Figure 1.11 Relation between pressure and temperature at equilibrium of $CaO/Ca(OH)_2$ [33]

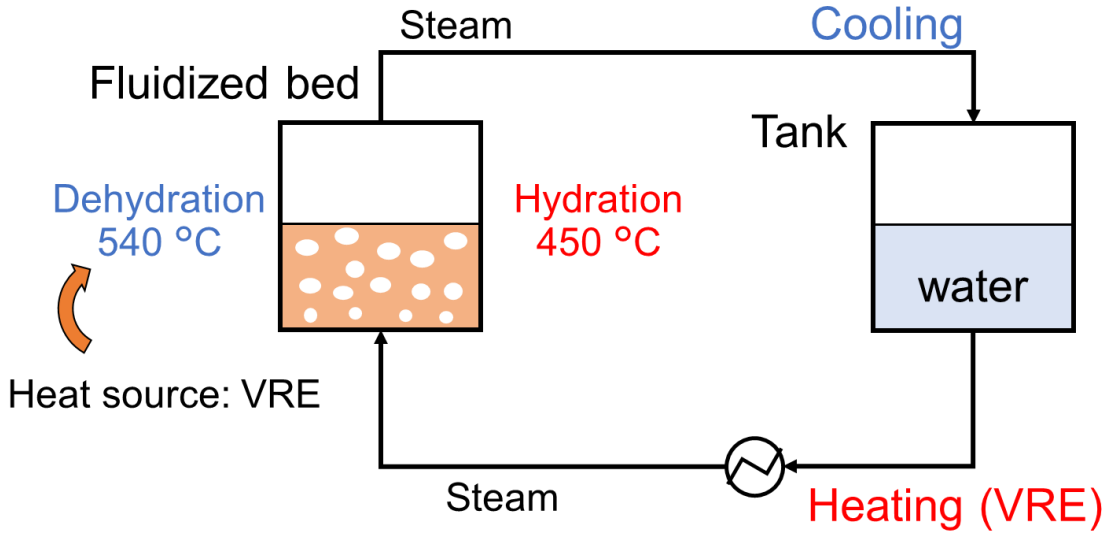

Figure 1.12 The TCS cycle (hydration and dehydration) in the case of using a fluidized bed reactor

1.3. Previous Studies

1.3.1. Previous Studies on Material Characteristics

To date, many research works have been conducted on the $CaO/Ca(OH)_2$ systems to understand its reaction kinetics and increase the reaction rate and stability. These studies are summarized in Table 1.3.

Matsuda et al. probed reaction kinetics by using a thermogravimetric reactor and derived an equation describing system behavior at a relatively low steam pressure (< 16.7 kPa) based on a grain model [34]. Schaube et al. analyzed the related kinetics for steam partial pressures up to 95.6 kPa [28]. Angerer et al. probed the reaction kinetics at higher steam pressures up to 0.5 MPa [35]. Zhang et al. studied the effects of CaO particle size on reaction kinetics, and the results are shown in Figure 1.13 [36]. It is shown that particle expansion greatly contributes to reaction deceleration. In particular, in the case that the particle size is bigger than 710 μm, the reaction rate dramatically decreases because the slow mass transfer inside of a particle inhibits the reaction.

In addition, the reaction kinetic was analyzed regarding different precursor of reactants. Abliz et al. used lime, scallop and coral powder as the precursor of reactants, and the results are shown in Figure 1.14 [37]. The conversion of CaO from scallop was lower than that of others. However, the conversion increases after seven repetitions of reaction. Yan et al. investigated the reaction kinetics under the high temperature conditions [38]. The reaction rate increased by increasing temperature. However, the risk of sintering due to carbonate formation becomes higher. The solution was also high temperature (900 °C). The reaction rate returns to the initial state. Thus, even if the components or crystal structure changes by reaction repetitions, the reaction rate is revived once the dehydration reaction occurs at high temperatures.

Hydration/dehydration reaction of $CaO/Ca(OH)_2$ has mainly been promoted by lithium doping [39–42], which lowers the energy barrier of dehydration and facilitates O–H

bond cleavage to increase the dehydration rate and thus allows the same heat storage efficiency to be achieved at a lower temperature [41]. In addition, Yan et al. also investigated the Mg doping effects [43]. However, the effects of Mg doping are too small. Shkatulov et al. investigated the doping effect of some salts [40]. The results show that KNO_3 was the highest effects of decreasing the dehydration temperatures.

Other researchers fabricated composites using expanded graphite or silicon carbide to increase the rate of intra-particle heat transfer or mass transfer, respectively [44,45]. The obtained particles could sustain > 100 cycles while maintaining an acceptable conversion and reaction rate [28]. The problems posed by agglomeration (observed in a bed after 35 cycles [46]), and low stability have been mitigated by nanoparticle doping [47,48], composite fabrication [24], and encapsulation [50] strategies. Above all, many studies have focused on material characteristics, and various methods were proposed for the improvement of the performance.

In addition, Table 1.4 summarizes the previous studies except for $CaO/Ca(OH)_2$. Many studies were carried out on $CaO/CaCO_3$ because the reaction is used as carbon capture and storage system. Similar methods for improving the performance of the TCS system were studied. These methods may be applied to $CaO/Ca(OH)_2$ system.

Table 1.3 Previous studies on material characteristics ($CaO/Ca(OH)_2$)

Contents of the studies	**Precursors / Doping / Composites / Methods**	**Ref.**
Kinetics	–	[28,34,36,51–58]
Improvement of reaction rate	Precursor: lime, scallop, coral powder	[37]
	Precursor: carbide slag	[59]
	High temperature	[38]
	Pure, LiCl, NaCl, KCl, $LiNO_3$, $NaNO_3$, KNO_3, LiOAc, NaOAc, KOAc	[40]
	Mg	[43]
	LiCl	[39]
	Li	[43,60,61]
	Ni	[62]
	Expanded graphite	[44]
	Silicon-carbide	[45]
Effect of CO_2, decomposing $CaCO_3$	–	[38,63]
Improvement of stability and/or inhibition of agglomeration	Nanoparticles (Aerosol)	[47,48]
	$Na_2Si_3O_7$	[64]
	Porous carbon	[65]
	Al	[66]
	Kaolinite ($Al_4Si_4O_{17}$)	[67]
	CMC (Vermiculite)	[49]
	Semipermeable	[50]

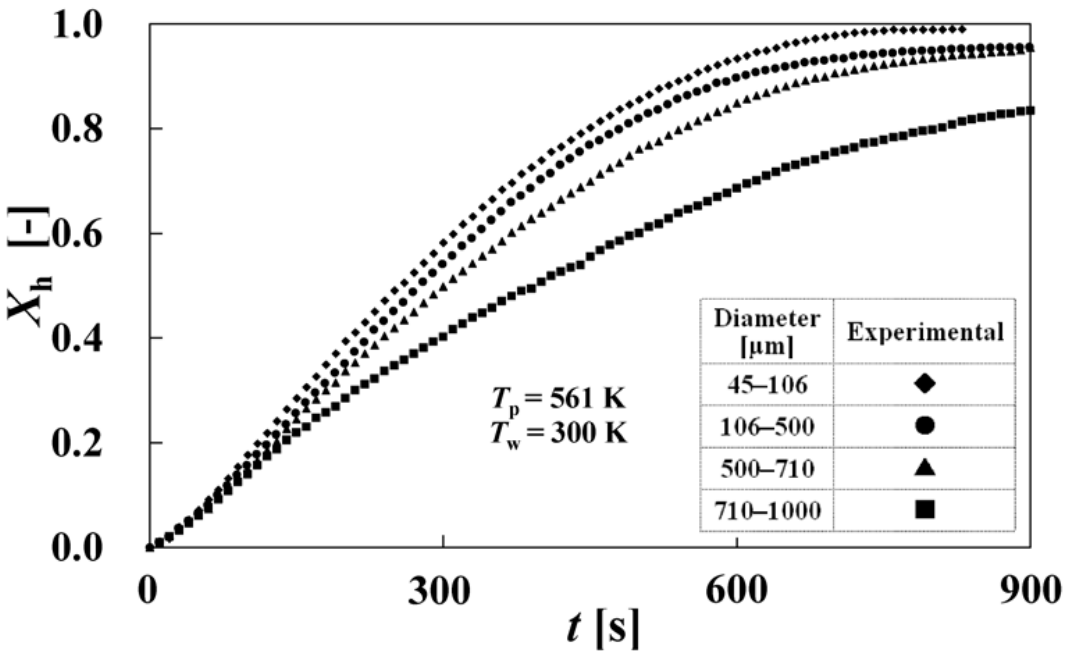

Figure 1.13 Hydration conversion changes of different diameter CaO particles analyzed by using thermogravimetric analysis unit

Reprinted with permission from ref. [36]. Copyright (2014) J. Chem. Eng. Japan

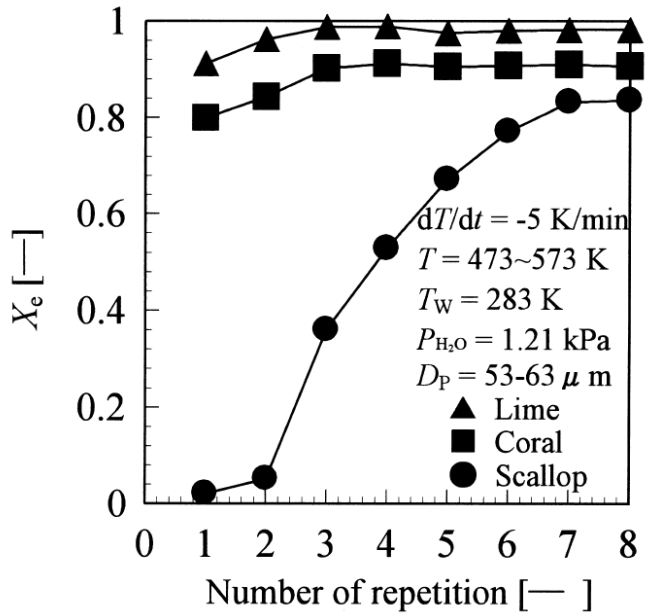

Figure 1.14 Final conversions of three CaO materials (precursors are lime, coral, and scallop powder) after some repetitions of reaction

Reprinted with permission from ref. [37]. Copyright (2004) J. Chem. Eng. Japan

Table 1.4 Previous studies on material characteristics (except for $CaO/Ca(OH)_2$)

TCS materials	Precursors / Doping / Composites / Methods	Ref.
$CaO/CaCO_3$	Limestone, biomass	[68]
	Limestone, carbide slag	[69]
	Limestone, marble, dolomite	[70]
	Pretreatment	[71]
	Limestone, dolomite, $Ca_3Al_2O_6$, ZrO_2	[72]
	Li_2SO_4	[73]
	Nano-silica	[74–77]
	$CaCO_3$ doped with metal oxides	[78]
	Mn+Fe	[79]
	CeO_2	[80]
	SiO_2	[81,82]
	AlOOH coated $CaCO_3$	[83]
	Nanoalumina	[84]
	$Ca_3Al_2O_6$	[85]
	Al	[86]
	Mesocellular siliceous foam (MCF)-supported CaO	[87]
	graphite nanosheet (H_3BO_3)	[88]
	Al, Si, Ti	[89]
	Mg nanoparticles	[90]
$CaCO_3/Ca(OH)_2$	Nanosilica	[77]
$MgO/MgCO_3$	KOAc, LiOAc, $Li_{0.42}K_{0.58}NO_3$, KNO_3, $NaNO_3$, K_2CO_3, Na_2CO_3, Li_2CO_3	[91]
$SrO/SrCO_3$	$CaSO_4$, $Sr_3(PO_4)_2$	[92]
$MgO/Mg(OH)_2$	Pretreatment	[93]
	LiOH	[94]
	$LiNO_3$	[95]
	LiBr, (Expanded graphite)	[96]
	Expanded graphite	[97]
	Carbon nanotube (separated curly tubes, Bundles of straight nanotubes)	[98]
	Exfoliated graphite (impregnation, deposition-precipitation)	[99]
	Pure, Li_2SO_4, Na_2SO_4, K_2SO_4, LiCl, NaCl, KCl, $CaCl_2$, LiOAc, NaOAc, KOAc, $LiNO_3$, $NaNO_3$, KNO_3, $RbNO_3$, $Mg(NO_3)_2$, $LixNa(1-y)NO_3$, $LiyK(1-y)NO_3$, $NazK(1-z)NO_3$	[40]
CoO/Co_3O_4	Composite (honey comb)	[100]
$CaCl_2$/hydrates	Silicagel	[101]

$SrBr_2$/hydrates	Natural graphite (pellet)	[102]
$CaCl_2$/hydrates	Impregnation (graphite, vermiculite), Encapsulation (ethyl cellulose)	[103]

1.3.2. Previous Studies on Reactors (gas-solid reactors)

Generally, gas-solid reactors can be divided into fixed beds, fluidized beds, and moving beds [26]. Table 1.5 summarizes previous studies on the gas-solid reactors for $CaO/Ca(OH)_2$ TCS system.

Fixed bed reactors are the simplest to operate but suffer from slow heat transfer due to the low thermal conductivity of the reactants [104] (approximately 0.1 W/(m·K) [105]) as well as agglomeration and/or channeling [47]. Various types of fixed bed reactors have been proposed [46,104,106,107] to improve their performance. Schaube et al. [108] studied a normal fixed bed reactor of continuous flow, and Dai et al. [109] and Yan et al. [61] studied a normal batch type fixed bed reactor. Some improved fixed bed reactors are summarized in Figure 1.15 and 1.16. These reactors were designed for improvement the heat transfer rate and facilitate the contact between reactant solids and gas. Fixed beds have also been extensively theoretically modeled [105,107,108,110–114].

Moving bed reactors are difficult to operate and have therefore been hardly used for heat storage [114]. Cosquillo et al. studied the moving bed using $CaO/Ca(OH)_2$ as shown in Figure 1.17 [115]. This structure was also aim for improvement of heat transfer rate. Criado et al. studied an entrained flow reactor (a circulating fluidized bed reactor), and the model was calculated at steady state [33].

Compared with fixed and moving bed reactors, fluidized bed reactors can be used to further facilitate heat transfer (up to 300 W/(m^2·K) [116]) and improve scalability. Because $Ca(OH)_2$ and CaO particles are small (usually several micro meters, i.e., Geldart C particles [29]) and difficult to fluidize, certain methods should be used to address this problem. Pardo et al. mixed the reactants (mean particle diameter is 3.8 μm) with Al_2O_3 or SiO_2 or SiC particles (Geldart A or B particles) as inert additives to promote fluidization ($Ca(OH)_2$: 20–35wt%) [29]. The results show that the case of $Ca(OH)_2$: Al_2O_3 = 30wt% : 70wt% is preferred in thirteen cases (mixing ratio was differed) considering homogeneous fluidization and mixing ratio. In

other study, $CaCO_3$ was used as a CaO precursor to preserve mechanical strength (active Ca: 9–51mol%) [117].

To evaluate the performance of the fluidized bed reactor, some models have been proposed. Among the models of a fluidized bed of $CaO/Ca(OH)_2$, Angerer et al. [35] assumed perfect mixing in each block of a fluidized bed (divided by baffles, see Figure 1.18) to develop a steady state model and used it to evaluate MW-scale fluidized bed reactors. Flegkas et al. [118] also provided a steady state model of a fluidized bed although the reactants were $MgO/Mg(OH)_2$. Criado et al. [117] produced a pseudo-steady state model, and the model image is shown in Figure 1.19. In this model, the fluidized bed was divided into the bubble and emulsion phases, and this model is called two-region models [119]. The study [117] included the mass transfer of H_2O between the bubble and emulsion phases. However, the calculations used experimentally determined bed temperatures instead of calculating the heat balance. Regarding $CaO/CaCO_3$ system, Wang et al. employed the Kunii-Levenspiel model (K-L model) to analyze CaO carbonation kinetics in a fluidized bed [120]. K-L model (Figure 1.20 [119]) is more detailed model than the two-region models and for a bubbling fluidized bed, and a fluidized bed is divided into following four phases; bubble, emulsion, cloud, and wake phases. A cloud phase is formed surrounding the bubble, and downflow occurs in a cloud phase. A wake phase is formed under a bubble, and solids of wake phase follow the bubble, and go up. It leads to the well circulation of the solids in a fluidized bed. In the calculation of the K-L model, cloud and wake phases are regarded as one phase (see Figure 1.20) and a fluidizing gas flow in only bubble phase and flow out from only bubble phase. The mass and heat transfer are considered between “bubble and (cloud + wake) phases” and “(cloud + wake) and emulsion phases”. Wang et al. [120] compared 1-D model (rate-equation-based grain model) and R-O model (reduced-order model) for facilitating the calculation, and the experiment data were represented by the R-O model.

Above all, many studies of lab-scale and pilot-scale of gas-solid reactors were carried

out. In addition, the calculation models on some reactors were proposed. A simple model is preferable for practical applications, thus, a proper reduced-order model is required. When VRE-derived heat is used for the TCS system, one should develop a dynamic model of a fluidized bed reactor to evaluate the effects of the VRE fluctuation.

The some previous studies on the gas-solid reactors (i.e., fixed bed, fluidized bed, and moving bed reactors) for TCS except for the $Ca(OH)_2$ to CaO conversion are summarized in Table 1.6. Some studies focused on the rotary kiln, entrained flow, vibrating reactors, etc. Various reactor structures were proposed for the performance improvement.

Table 1.5 Previous studies on the use of gas-solid reactors for TCS based on the $Ca(OH)_2$ to CaO conversion

Reactor type	**Experiments**	**Simulations**	
		Steady state	**Non-steady state**
Fixed bed	[46,61,104–106,108,109]	–	[105,107,108,110–114]
Fluidized bed	[29,35,117]	[35]	[117]
Moving bed	[115]	[33]	–

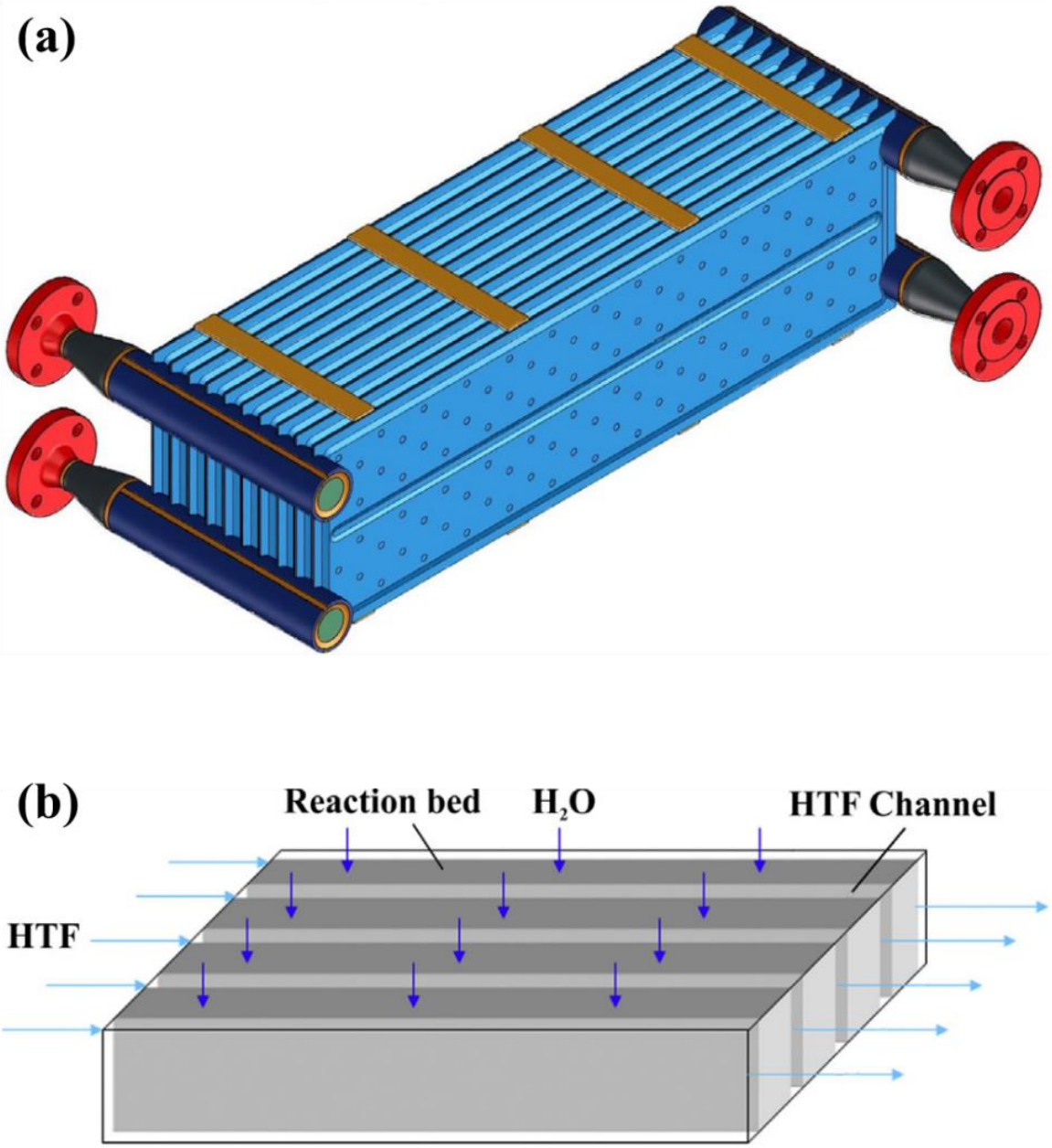

Figure 1.15 A fixed bed reactor of cross flow type (a) schematic of the reactor and (b) the cross flow design [104,105]

Reprinted with permission from ref. [104]. Copyright (2014) Elsevier B.V.

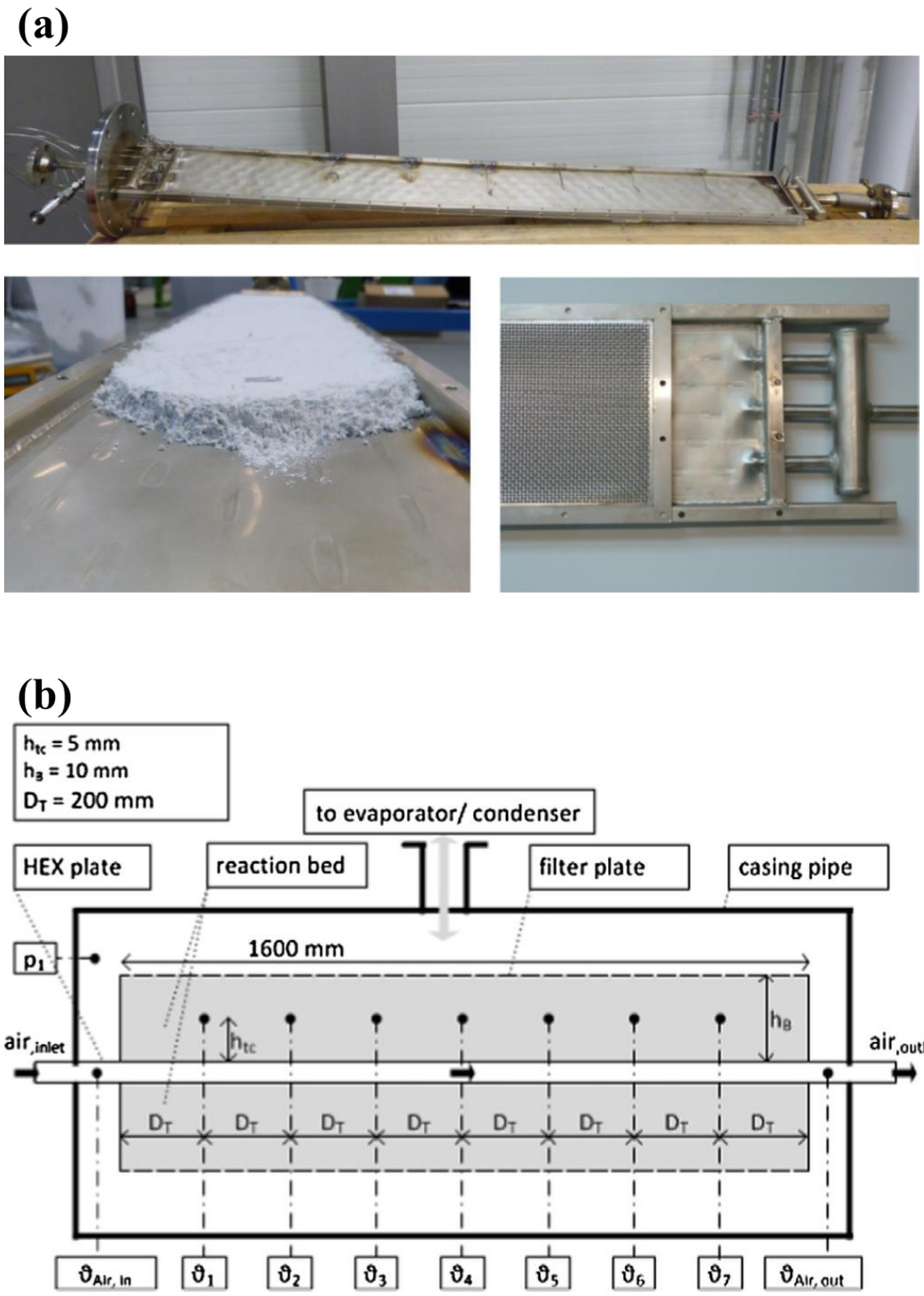

Figure 1.16 A fixed bed reactor of plate type (a) the photo of the reactor and (b) the reactor and flow design [46,106]

Reprinted with permission from ref. [106]. Copyright (2017) Elsevier B.V.

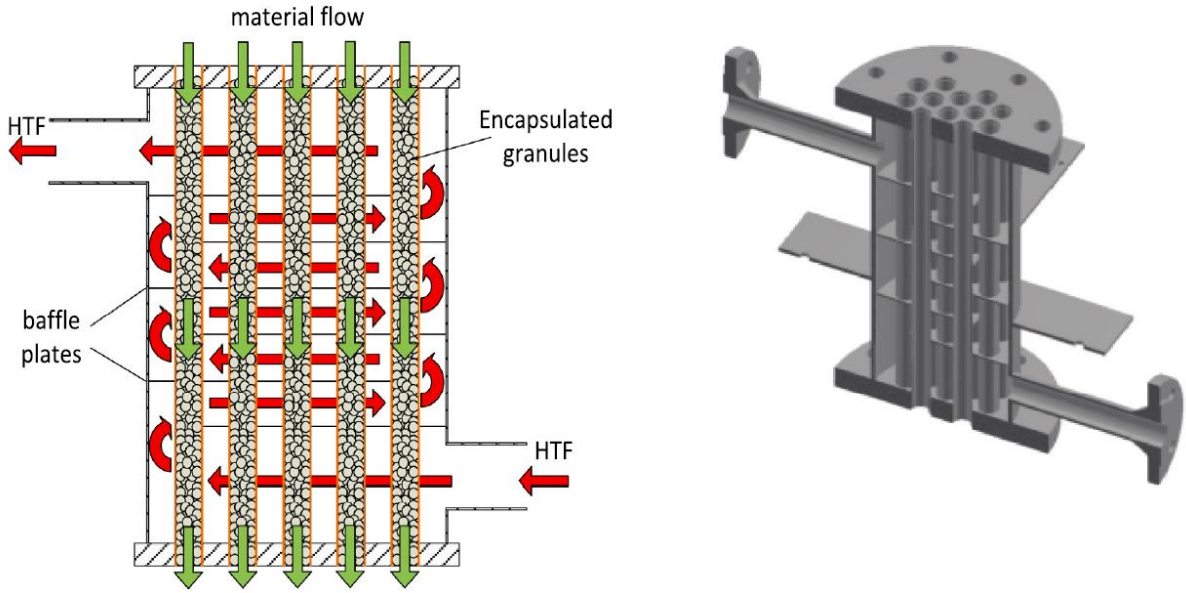

Figure 1.17 Schematic representation (left), and 3D image of the reactor (right)

Reprinted with permission from ref. [115]. Copyright (2020) Elsevier B.V.

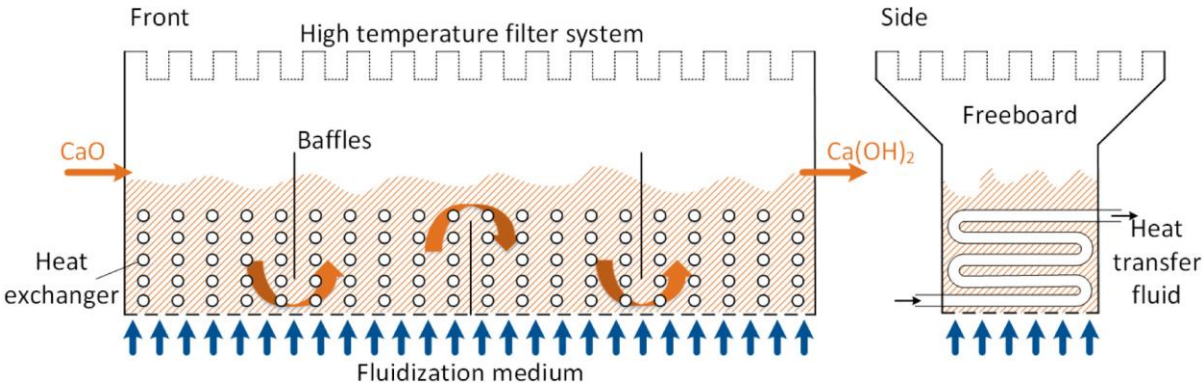

Figure 1.18 Continuous fluidized bed reactor for MW-scale

Reprinted with permission from ref. [35]. Copyright (2018) Elsevier B.V.

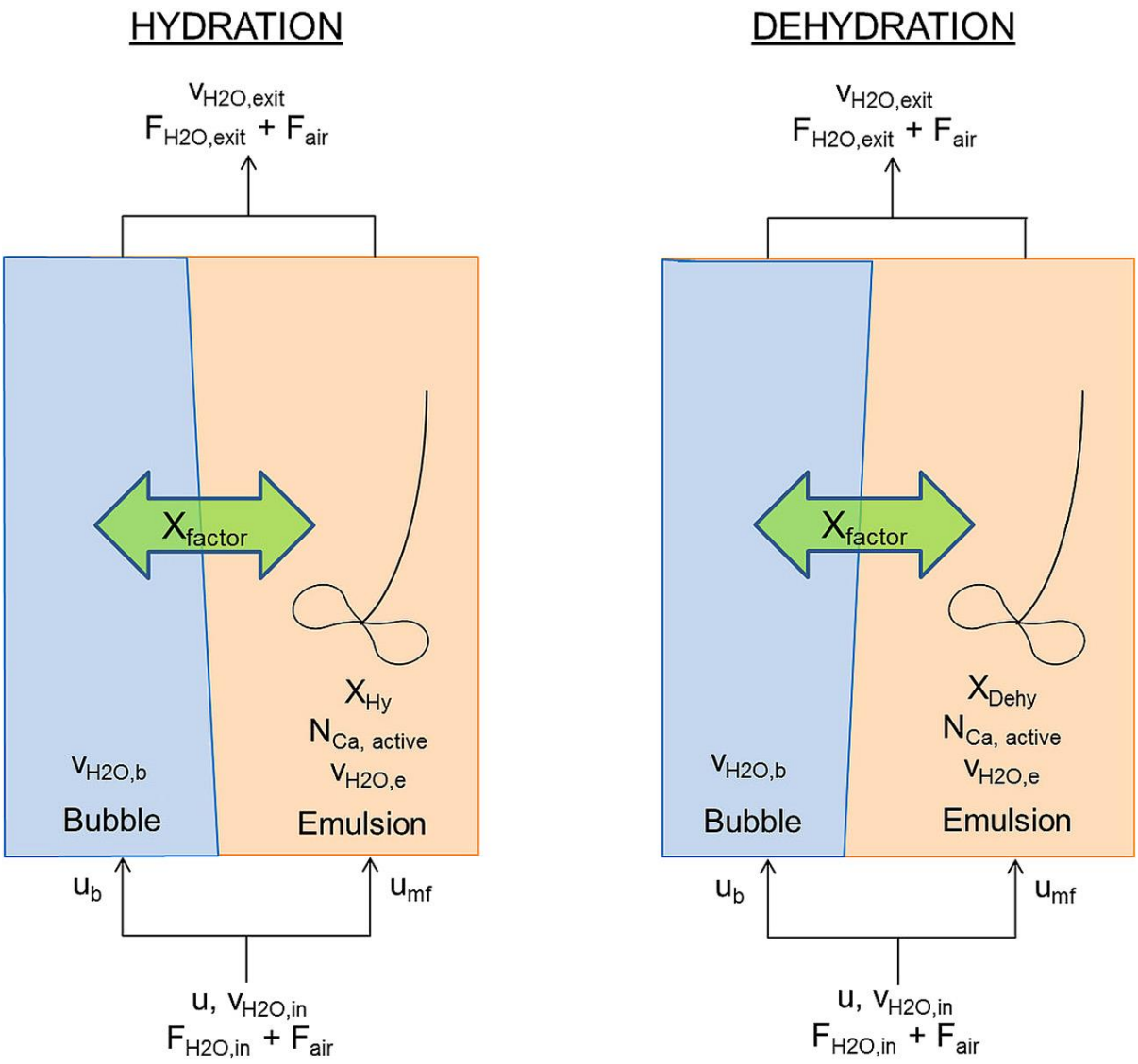

Figure 1.19 The two-region models of fluidized bed during hydration (left) and dehydration (right) with main variables in the referenced paper

Reprinted with permission from ref. [117]. Copyright (2017) Elsevier B.V.

(a)

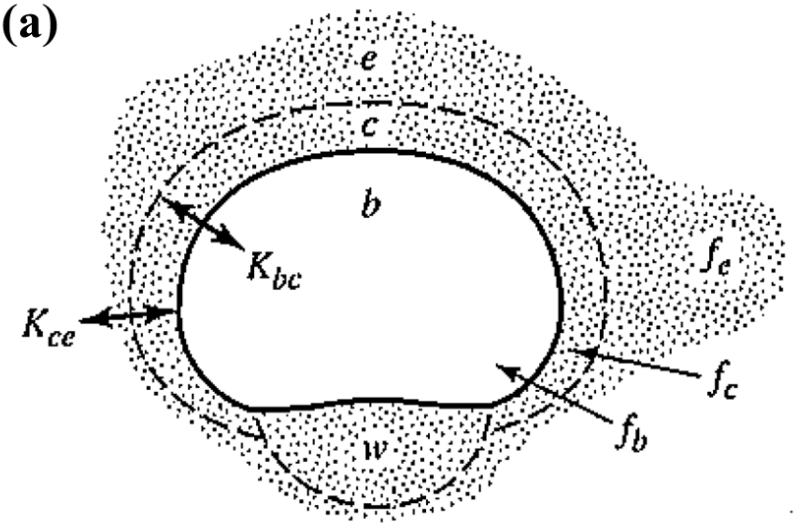

e: emulsion, c: cloud, b: bubble, w: wake

(b)

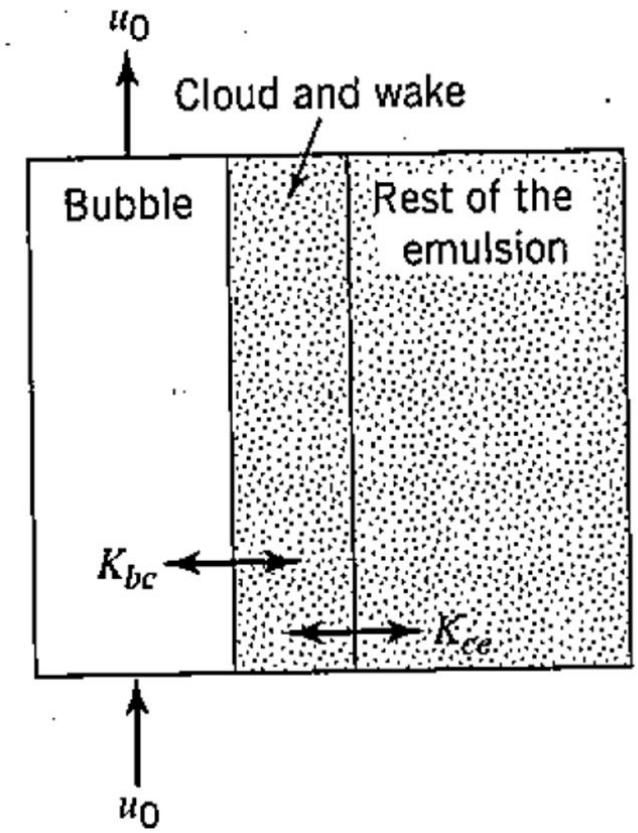

Figure 1.20 The K-L model (a) hypothesis of phases in a bubbling fluidized bed and (b) the image of mass and heat transfer among the phases [119]

Table 1.6 Previous studies on the use of gas-solid reactors for TCS except for the $Ca(OH)_2$ to CaO conversion

Reactor type	Experiments	Simulations	
		Steady state	**Non-steady state**
Fixed bed	CoO/Co_3O_4 [121] $SrBr_2$/hydrate [122]	Na_2S/hydrate [123]	$MgO/Mg(OH)_2$ [124] $MgH_2+Mg(OH)_2$ [125] CoO/Co_3O_4 [126,127]
Fluidized bed	$CaO/CaCO_3$ [120,128] $CaCO_3/Ca(OH)_2$ [77]	$MgO/Mg(OH)_2$ [118]	$CaO/CaCO_3$ [120]
Moving bed	$CaCl_2$/hydrate, vibrating [101] $SrBr_2$/hydrate (using rotary valve) [129] $SrBr_2$/hydrate, multilayered sieve reactor [130]	CoO/Co_3O_4, rotary kiln [100]	$CaO/CaCO_3$, entrained flow [131] $CaCl_2$/hydrate, vibrating [101] $SrCl_2$/hydrate, free fall (Air: cross flow) [30] $SrBr_2$/hydrate, multilayered sieve reactor [130]

1.3.3. Previous Studies on Process Evaluation and Economics

Process development and evaluation are also important. Table 1.7 summarizes the previous studies on process evaluation integrated with the TCS system using $CaO/Ca(OH)_2$. The TCS system using $CaO/Ca(OH)_2$ was integrated with CSP plants mainly. Schmidt and Linder [46] stated that the high storage efficiency of 87% can be achieved. Pelay et al. [132] studied the water management. In charging time, steam at high temperature comes out from the reactor, and the liquid water should preferably be stored. Thus, it is required to cool the steam. In discharging time, it is needed to heat the water to produce the reactant gas. These heating and cooling are key issues for improving energy efficiency. Considering the water management, they proposed a process based on the three integration concepts: thermal, mass, and turbine integration concepts [132,133]. These processes (contain the only CSP plant) are shown in Figure 1.21. In thermal integration concepts, the CSP, Rankine cycle, and TCS circuits are indirectly heated (i.e., heat is transferred among the circuits although the fluids are not contacted or mixed). In the mass integration concepts, the fluids of Rankine cycle and TCS circuits are mixed in the water reservoir (see Figure 1.21 (C)). In turbine integration concepts, a turbine is placed in the downflow of reactor. In discharging time, the steam produced by dehydration reaction is used as working fluid of the turbine, and the enthalpy of steam is changed to the electricity. As the results, they reported that the turbine integration concept was most effective [132,133].

Some previous studies also investigated the strategies by considering spot market [9,10] (in which selling electricity price is changed every 30 min [11]). Generally, selling price is high in the evening [9–11] because the decrease of solar power generation coincides with the increase of demand as people go home. This tendency is predicted to become larger by the spread of the solar power generation. Thus, it is expected that energy is stored at daytime and utilized in the evening. Pelay et al. [133] investigated the strategies of power generation (continuous and peak production modes) as shown in Figure 1.22. In the continuous production

mode, the same power generation was kept during phase 2 and 3 by using the TCS system. On the other hand, in the peak production mode, the power generation from the TCS system was carried out in the evening (just after the charging time) because the electricity price was high, and it achieved the maximum cost merit although the global efficiency decrease.

However, there are serious problems of integrating the Carnot battery with the CSP plant although all the previous studies shown in Table 1.7 focused on the integration with CSP plant. Using molten salt and heat transfer fluid has a restriction of the small temperature differences between the reaction temperature and today's maximum operating temperature of the salt [46]. Thus, this study focuses on the integration of the TCS system with a biomass power plant. The details on the integration process will be described in Chapter 3.

Biomass power is renewable energy and widely used as base load power because of power generation stability. One of the problems is the difficulty of scale-up because a biomass growing rate is much slower than that of combustion (the use as fuel) and transportation of biomass fuel to the power plant release CO_2. Table 1.8 summarizes the previous studies on a biomass power plant integrated with Carnot batteries. In these studies, organic Rankine cycle (ORC), steam Rankine cycle, and gas turbines were used to convert the stored heat to electricity, and these methods are chosen by considering the temperature of heat source and the scale of the process. ORC is generally used in the case of low heat source temperature (65–350 °C [134]) and low power generation (< 2 MW_e). In ORC working fluid, there are three types; wet, isentropic, and dry fluids. *T-s* diagrams of these types are shown in Figure 1.23. As saturated vapor expands, saturated vapor changes to liquid in wet fluid case, saturated vapor in isentropic case, and superheated vapor in dry fluid case. In the case of low operating temperature ORC, the isentropic or dry fluid is preferable because it is not necessary to superheat the vapor, and liquid droplets are not formed in a turbine [134]. Some candidates of working fluid of ORC are summarized in Table 1.9. R245fa is widely used as organic materials [135] because of

comparatively high molecular weight, which can make the system compact, and zero value of ODP [136].

The previous studies on the evaluation of the integration process are summarized in Table 1.10. Various processes and power generation strategies were evaluated. Regarding CSP and $CaO/Ca(OH)_2$ TCS system integration [9,10], at present, there is no profit, and subsidy is needed (net present value was negative value). To the best of our knowledge, there is no research on evaluation of a biomass power plant integrated with the TCS system with a fluidized bed.

Table 1.7 Previous studies on development of process integrated with the TCS system using $CaO/Ca(OH)_2$

Material	Integration	Capacity	Main results	Ref.
$CaO/Ca(OH)_2$	CSP plant	< 125 MW_e	Storage efficiency (< 87%)	[46]
	CSP plant	100 MW_e	Overall energy efficiency (< 39.2%) Exergy efficiency (52%)	[132]
	CSP plant	100 MW_e (Peak 1 GW_e)	Global efficiency (< 31.96%)	[133]
	CSP plant	< 55 MW_e	Cost (net present value: −89.92 M€)	[9]
	CSP plant	< 55 MW_e	Cost (required subsides: < 52 €/MWh)	[10]
	CSP plant	100 MW_e/294 MW_{th}	Thermal efficiency (98.51%) Cost (total capital cost: 4.78 $/$MJ_{th}$)	[137]

(A)

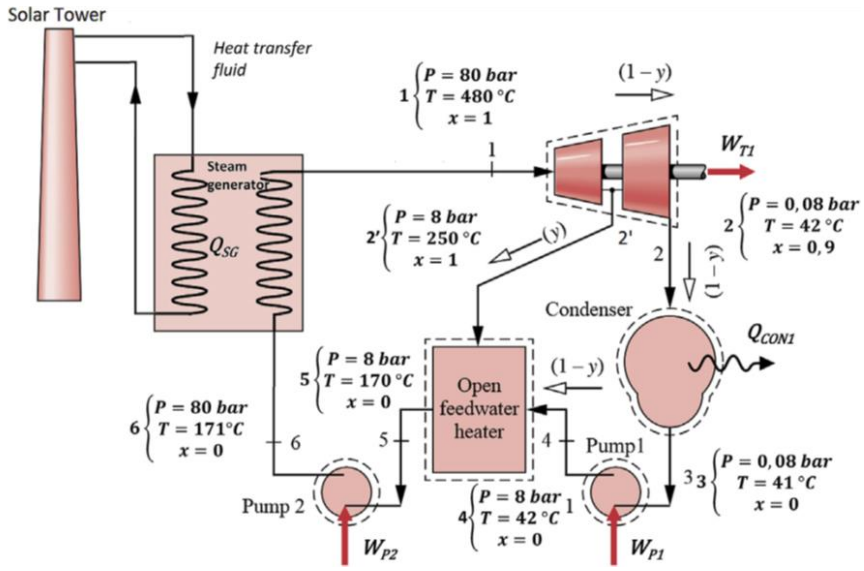
Solar Tower
Heat transfer fluid
Steam generator
Q_{SG}
$P = 80\ bar$ $T = 480\ °C$ $x = 1$
W_{T1}
$P = 8\ bar$ $T = 250\ °C$ $x = 1$
$P = 0,08\ bar$ $T = 42\ °C$ $x = 0,9$
Condenser
Q_{CON1}
$P = 8\ bar$ $T = 170\ °C$ $x = 0$
Open feedwater heater
$P = 80\ bar$ $T = 171°C$ $x = 0$
Pump1
$P = 0,08\ bar$ $T = 41\ °C$ $x = 0$
Pump 2
$P = 8\ bar$ $T = 42\ °C$ $x = 0$
W_{P2}
W_{P1}

(B)

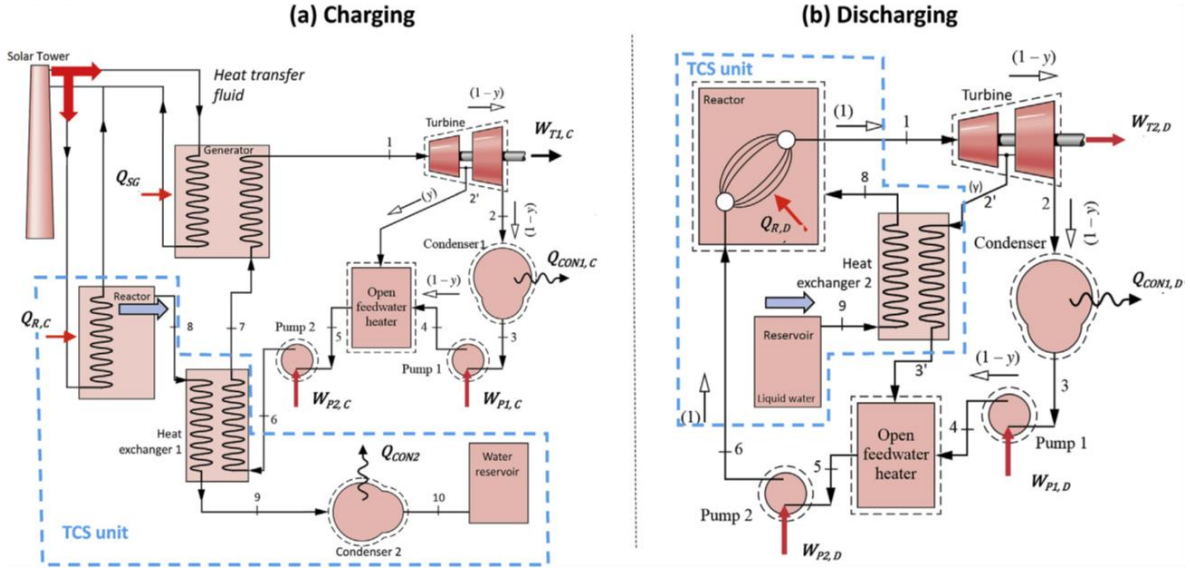
(a) Charging
(b) Discharging
Solar Tower
Heat transfer fluid
Generator
Q_{SG}
Turbine
$W_{T1,C}$
Condenser1
$Q_{CON1,C}$
Reactor
$Q_{R,C}$
Open feedwater heater
Pump 2
Pump 1
$W_{P2,C}$
$W_{P1,C}$
Heat exchanger 1
Q_{CON2}
Water reservoir
Condenser 2
TCS unit
Reactor
$Q_{R,D}$
Turbine
$W_{T2,D}$
Heat exchanger 2
Reservoir
Liquid water
Condenser
$Q_{CON1,D}$
Open feedwater heater
Pump 1
Pump 2
$W_{P1,D}$
$W_{P2,D}$

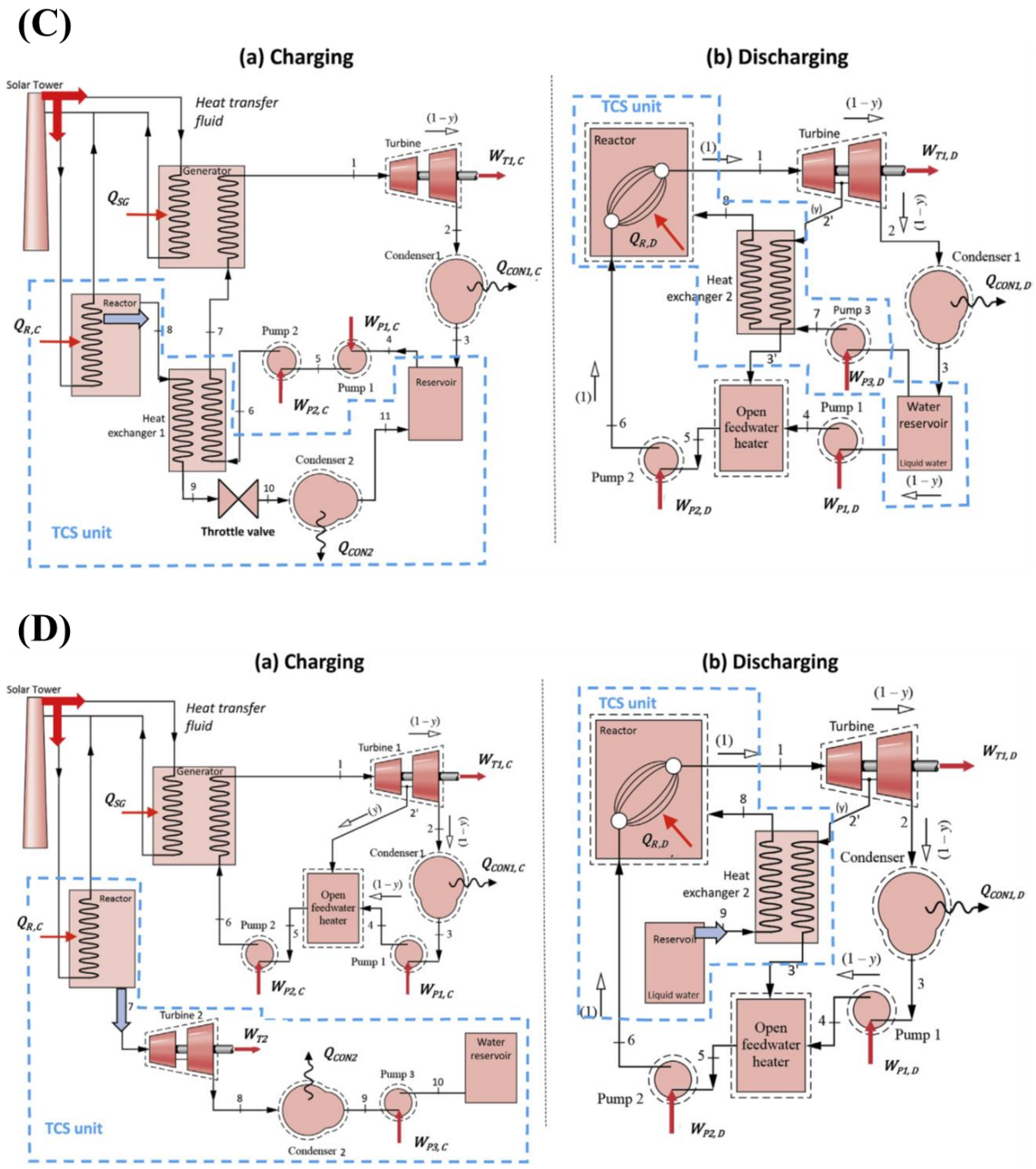

Figure 1.21 Schematic view of (A) a conventional regenerative Rankine cycle driven by CSP without the TCS system, (B) the thermal integration concept, (C) the mass integration concept, and (D) the turbine integration concept [132,133]

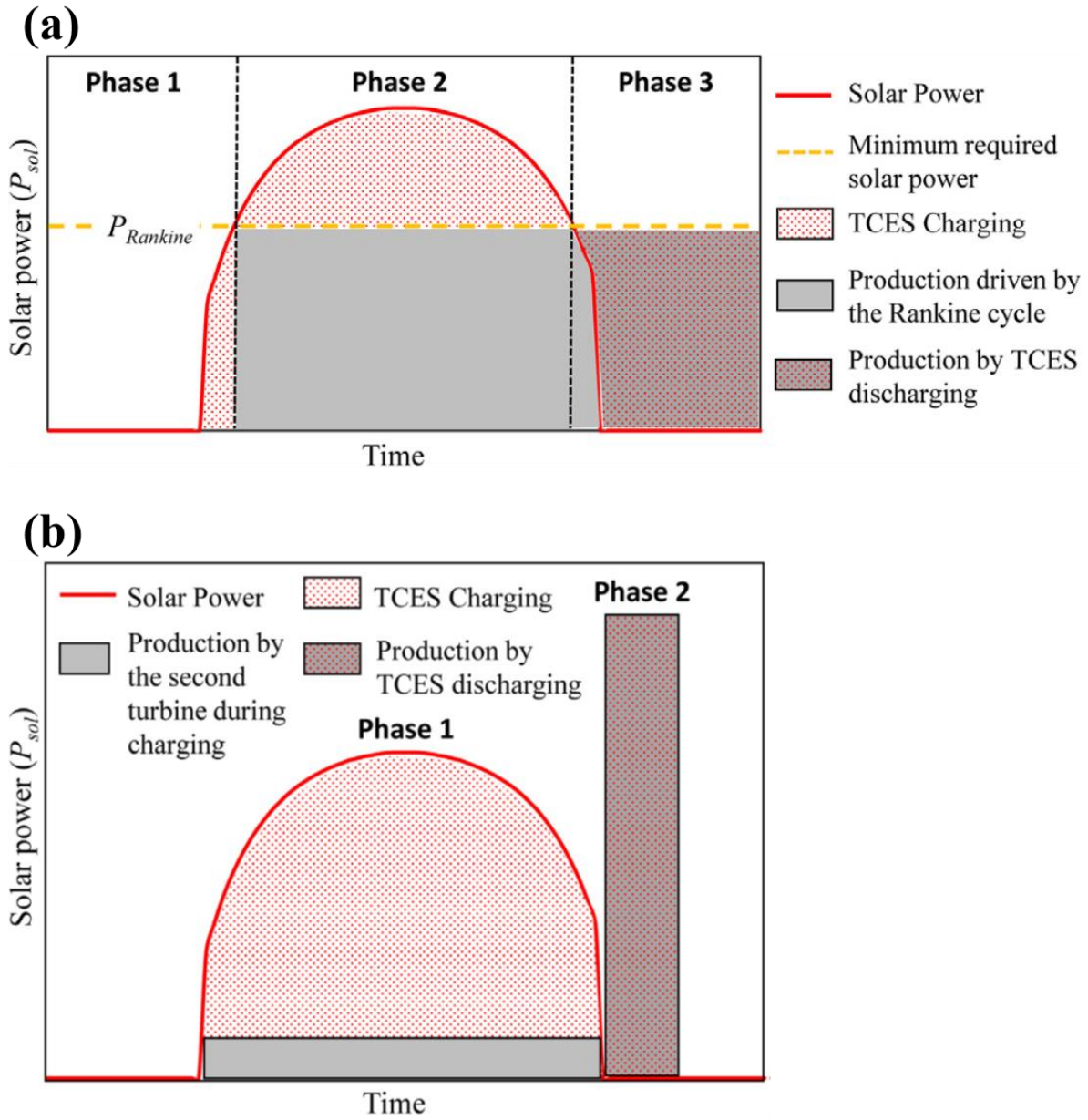

Figure 1.22 The operation mode of the TCS system integrated with CSP plant; (a) continuous production mode and (b) peak production mode

(TCES in this figure is the same for TCS)

Reprinted with permission from ref. [133]. Copyright (2019) Elsevier B.V.

Table 1.8 The previous studies on biomass power process integrated with energy storage

Storage methods	Integration	Scale	Main results	Ref.
Sensible heat storage	CSP plant, Biomass	2188 kW_e 2150 kW_{th}	global electric efficiency (20–25%)	[138]
Latent heat storage, Compressed air	CSP plant, Biomass	Maximum 80.45 MW_e	overall energy efficiency (28.58%), overall exergy efficiency (24.08%) (in the discharging period)	[139]
Latent heat storage	CSP plant, Biomass	3861 kW_e	Levelized cost of electricity (0.180 €/kWh_e)	[140]
Steam accumulator, Sensible heat storage, Latent heat storage	Biomass	Maximum 8.5 MW_e	storage efficiency (30–58%)	[141]
Compressed air	Biomass, Geothermal	6255.9 kWh_e	round trip efficiency (90.06%), exergy efficiency (31.52%)	[142]

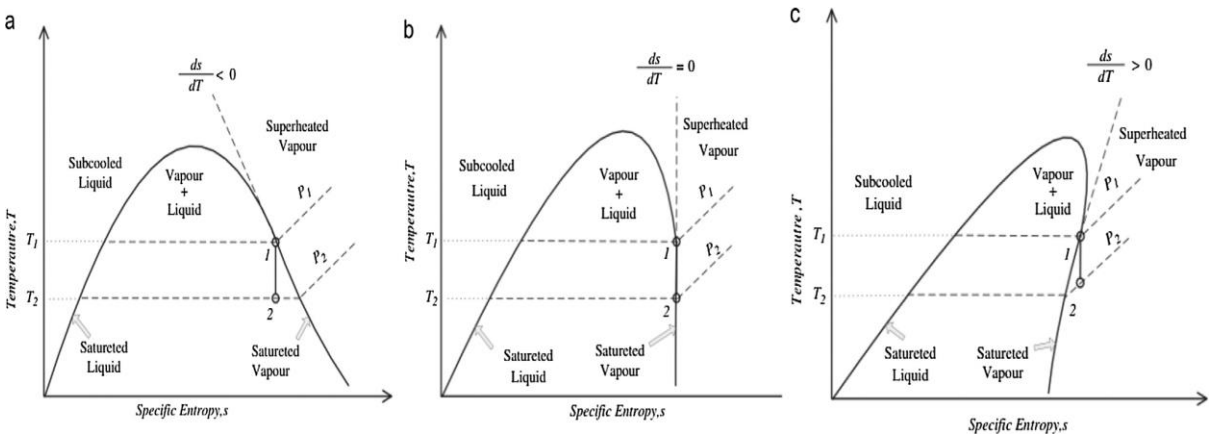

Figure 1.23 *T-s* diagram for (a) wet, (b) isentropic, and (c) dry fluid regrading ORC

Reprinted with permission from ref. [143]. Copyright (2018) Elsevier B.V.

Table 1.9 The properties of some ORC working fluids

Reprinted with permission from ref. [135]. Copyright (2020) Elsevier B.V.

Organic fluid	unit	R113	R123	R1233zd	R141b	R245fa	HFE7000	Butane	Isobutane	Pentane	Isopentane	Cyclopentane
T_{cr}	[K]	487	457	439	478	427	438	425	408	470	460	512
P_{cr}	[kPa]	3390	3660	3573	4212	3651	2476	3790	3640	3370	3378	4571
NBP	[K]	321	301	291	305	288	307	273	261	309	301	322
Heat of evaporation	[kJ/kg]	367	168	195	223	196	134	385	303	358	343	389
GWP	–	1.55	120	1	782	858	530	20	3	5	5	0.1
ODP	–	0.9	0.012	0	0.12	0	0	0	0	0	0	0
Molecular weight	[g/mol]	187	153	132	117	134	200	58	58	72	72	70
Gas density	[kg/m^3]	1.25	2.24	5.7	4.86	5.96	8.41	2.757	4.26	2.97	3.06	2.75
Dynamic viscosity	[kg/m·s]	920	565	529	386	473	436	202	199	202	215	325
c_p	[kJ/kg/K]	0.62	0.64	1.24	1.16	1.3	1.24	1.59	1.55	2.36	2.28	1.93
Heat conductivity	[kW/m/K]	0.077	0.084	0.08	0.09	0.09	0.07	0.115	0.098	0.11	0.11	0.12
Flammability	–	–	–	–	–	–	–	3	3	3	3	3
Toxicity	–	A	B	–	–	B	–	B	B	A	A	–
Fluid type		Dry	Dry	Dry	Dry	Dry	Dry	Dry	Dry	Dry	Dry	Dry
Thermal stability		Y	Y	Y	N	Y	Y	Y	Y	Y	Y	Y

Note (regarding Table 1.9):

T_{cr}: critical temperature

P_{cr}: critical pressure

c_p: heat capacity

NBP: Normal boiling point

GWP: Global Warming Potential for $CO_2 = 1.0$

ODP: Ozone Depletion Potential for R11 = 1.0

Dynamic viscosity $\times 10^6$

ASHRAE Standard 34 1: low flammability, 2: medium flammability, 3: high flammability

ASHRAE Standard 34 A: lower toxicity, B: higher toxicity

(ASHRAE: American Society of Heating, Refrigerating and Air-Conditioning Engineers)

Table 1.10 The summary of the previous studies on process performance and economics evaluations of the TCS integration process

	Storage materials	Integration process	Novelty	Evaluated parameters	Ref.
Process evaluation	$Ca(OH)_2$	CSP plant	Discharging: 4 modes (steam extraction conditions in the turbine were different)	Energy efficiency	[46]
		CSP plant	4 processes ① without TCS ② thermal integration concepts ③ mass integration concepts ④ turbine integration concepts	Exergy flow diagram	[132]
		CSP plant	4 processes (the same as [132]) ① summer or winter (continuous production mode) ② 2 operating modes (continuous production and peak production modes)	Global efficiency	[133]
	19 materials	CSP plant	Compared to materials	Energy distribution	[137]
	$CaCO_3$	PV[*1]	Peak shift	Mass and energy balance Daily duration curve	[144]
	$CaCO_3$	CSP plant	Investigation of main parameter effects (sensitivity analyses)	Global efficiency	[145]
		CSP plant	3 processes ① base case ② improvement process ③ improvement process by pinch analysis	Energy balance Global net efficiency	[146]

	CSP plant	4 processes (comparing sun, night, and sun mode w/o storage modes) ① base case ② solids heat exchangers ③ solids heat exchangers + intercooled compression ④ solids heat exchangers + intercooled compression + carbonator pressure is ambient pressure	Overall plant efficiency	[147]
	CSP plant	The effects of sensible heat (sensitivity analysis)	Sensible heat ratio	[148]
	CSP plant	Mg doping effect	Overall plant efficiency	[90]
	CSP plant	4 processes ① closed CO_2 Brayton cycle ② reheat Rankine cycle ③ super critical CO_2 recompression cycle ④ combined cycle (sensitivity analysis)	Global integration efficiency	[149]
	CSP plant	Optimizing heat exchanger network by pinch analysis (considering solid-solid heat transfer or not, and constraining the double carbonator inlet temperature)	Carbonator side efficiency Heat exchanger network	[150]
Co_3O_4	compressed air storage	Integrating compressed air energy storage system (sensitivity analysis)	Exergy flow diagram Round trip efficiency	[151]
Molten	biomass, CSP,	6 cases	Energy flow	[138]

	salt	ORC	① 3 places (different solar power generation) Priolo Gargallo (Italy) Marseilles (France) Rabat (Morocco) ② solar multiple = 2.1 or 4.2 (excess thermal power produced by the solar field)	Exergy balances Global energy efficiency	
Cost evaluation	$Ca(OH)_2$	CSP plant	3 cases ① no storage system ② classic strategy (discharging in the evening) ③ pre-scenario strategy (discharging in the morning and evening) (considering spot market, 4 seasons) (solar multiple = 2.5)	Net present value	[9]
		CSP plant	2 cases (California or Sevilla) (almost all the process is the same for [9])	Required subsidy = − (net present value) / (the electricity generated over the lifetime of the plant)	[10]
	19 materials	CSP plant	Compared to materials	Cost breakdown	[137]
	$CaCO_3$	PV[*1]	Peak shift	Total overnight cost	[144]
	Molten salt	biomass, CSP, ORC	6 cases ① 3 places (different solar power generation) Priolo Gargallo (Italy) Marseilles (France)	LCOE[*2] Net present value Internal rate of return	[138]

Rabat (Morocco)

② solar multiple (= 2.1 or 4.2)
(excess thermal power produced by the solar field)

---

*1PV: Photovoltaics

*2LCOE: Levelized cost of electricity

1.4. Objectives of This Dissertation

In this dissertation, it was investigated to improve and evaluate the $CaO/Ca(OH)_2$ TCS system with a fluidized bed. The aim is for promoting the utilization of renewable energies to alleviate the global warming. As described in the above sections, many studies on material characteristics were carried out. However, the studies regarding the dynamic model of a fluidized bed and the process design of the TCS system integrated with a biomass power plant are not carried out. Thus, this dissertation focuses on creating the dynamic model of a fluidized bed, evaluating the absorption of the VRE fluctuation, creating the TCS system integrated with a biomass power plant, evaluating the process performance regarding the energy efficiencies and flexibility of the power generation, improving the process performance, and evaluating the economics of the proposed process. The details of each chapter are as follows.

In Chapter 2, a dynamic model of a fluidized bed reactor for $CaO/Ca(OH)_2$–based TCS was created. As described in section 1.1.2, power generation by VRE is fluctuated, and it is required to absorb the fluctuation. As described in section 1.3.2, the reduced-order model is required for facilitating the calculation and practical application. Hence, the author herein developed the simplified dynamic model, validated this model by comparison with experimental data [29], investigated the influences of the VRE fluctuation on reactor temperature by fluctuating the input energy, and evaluated the performances of the fluidized bed using nitrogen or steam as the fluidizing gas.

In Chapter 3, the author created the biomass power generation process integrated with the TCS system using the fluidized bed with $CaO/Ca(OH)_2$ particles. In the power generation strategy, one day was separated in three times; normal operation (only ORC was worked), charging, and discharging times. The ORC working fluid was R245fa and the power output during the normal operation was set to 1 MW_e. The integrated process was evaluated from energy storage efficiency, the TCS system efficiency, and round-trip efficiency, and the effects of operational parameters regarding the TCS system were examined. As described in section

1.1.2, the flexible power generation is required to alleviate the dramatic increase of net load in the evening. Thus, the flexibility of power generation was also evaluated. In addition, the improvement process was proposed and evaluated.

In Chapter 4, the process described in Chapter 3 was improved. R245fa used in Chapter 3 has toxicity (Table 1.9). R1233zd is more eco-friendly material. Thus, it is preferable. This chapter focuses on the following three points. First, the energy efficiencies were evaluated by varying the two organic working fluid (R245fa and R1233zd), the turbine inlet temperature, superheated temperature of the working fluid, and the scale of the power generation. In addition, the performance of the TCS system and ORC was evaluated by varying the fluidized bed volume. Second, the process performance was evaluated during charging time when the heat source supplied to the TCS system was fluctuated. Third, the economics of the TCS system were calculated.

1.5. Structure of This Dissertation

The composition of this dissertation is illustrated in Figure 1.24. This dissertation focused on $CaO/Ca(OH)_2$ TCS system, a fluidized bed reactor, an integration of the TCS system with a biomass power plant.

In Chapter 1, the social energy problem to the solution dealt with this dissertation was described. The previous related studies were summarized by classifying the material characteristics, gas-solid reactors, and process evaluation. The objectives and novelty of this dissertation were described at the end.

In Chapter 2, a dynamic model of a fluidized bed reactor was created, and the model was validated by the experimental data reported in literature. The boundary of this chapter is shown in Figure 1.25. Note that the model validation of hydration reaction was also carried out. However, main evaluations are only dehydration reaction. The absorption of the VRE fluctuation was evaluated by using the dynamic model. In addition, the performances of the fluidized bed using nitrogen or steam as the fluidizing gas were evaluated because the energy efficiencies in discharging time was expected to increase as steam partial pressure decreases by using nitrogen as a fluidizing gas.

In Chapter 3, the process evaluation at non-steady state was carried out by using the fluidized bed dynamic model. The boundary of this chapter is shown in Figure 1.26. The TCS system integrated with a biomass power plant was created and evaluated by using three types of energy efficiencies. Then, the flexibility of the power generation from the proposed integration process was evaluated.

In Chapter 4, the proposed process was improved. The boundary of this chapter is shown in Figure 1.26 (the same as Chapter 3). The performances of the working fluid of ORC were compared, and the effect of process parameters regarding the biomass power plant were evaluated. In addition, the economics of the proposed TCS system was evaluated.

In Chapter 5, the conclusions of this dissertation were summarized, and the future plans were described.

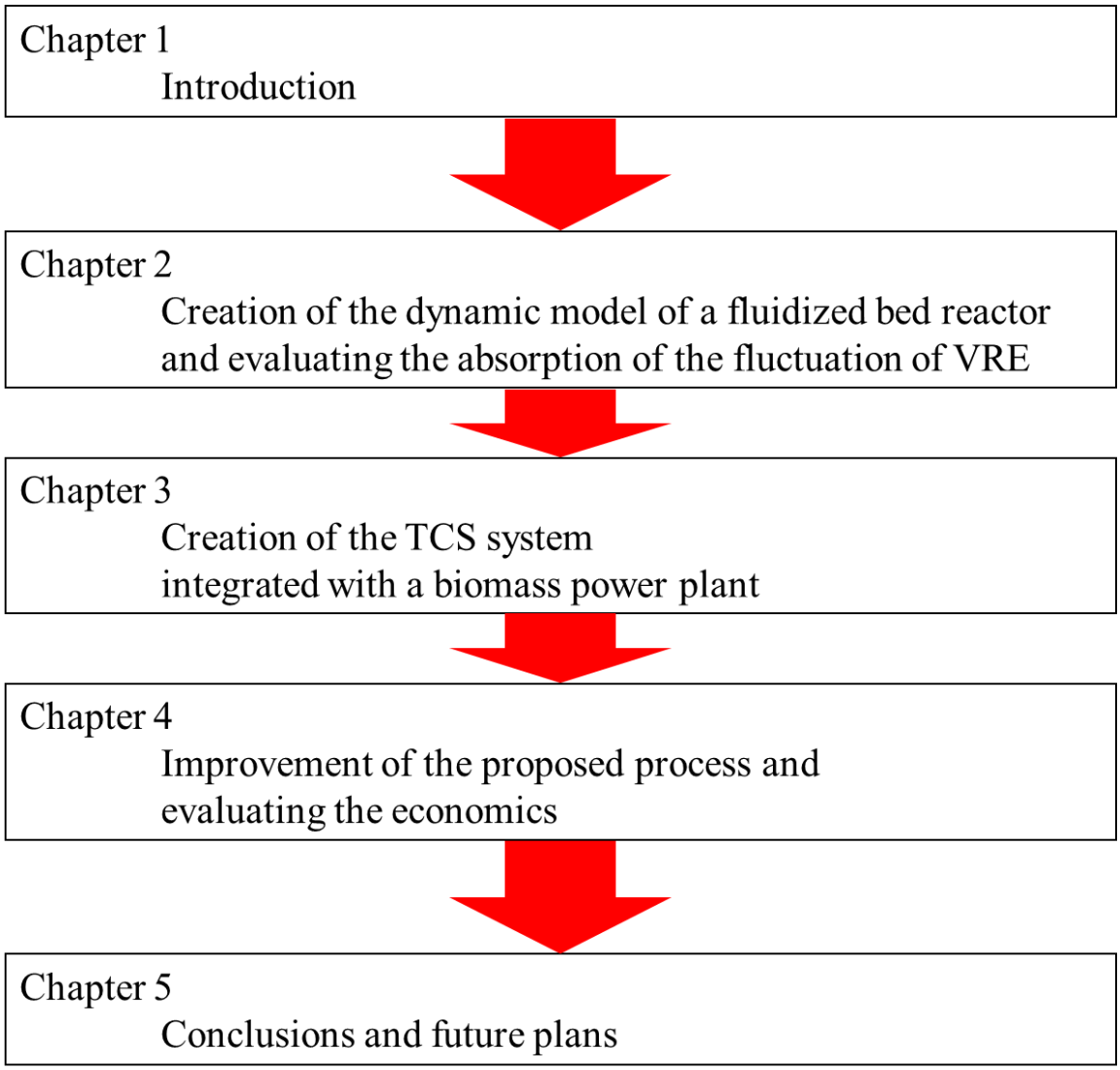

Figure 1.24 Structure of this dissertation

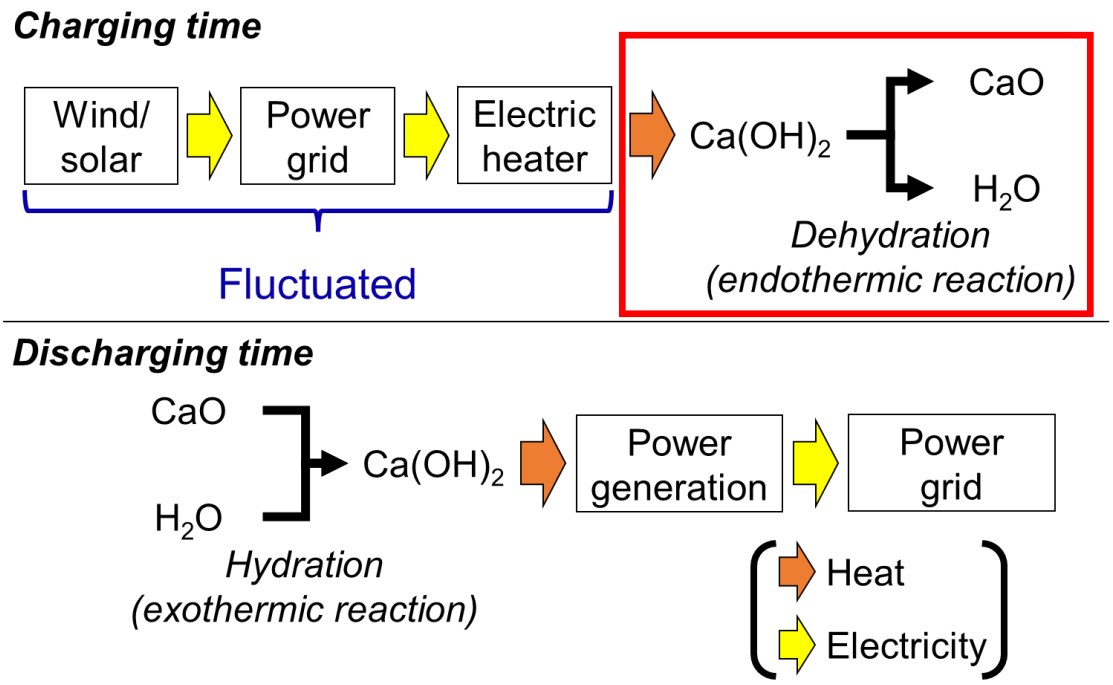

Figure 1.25 The boundary of Chapter 2

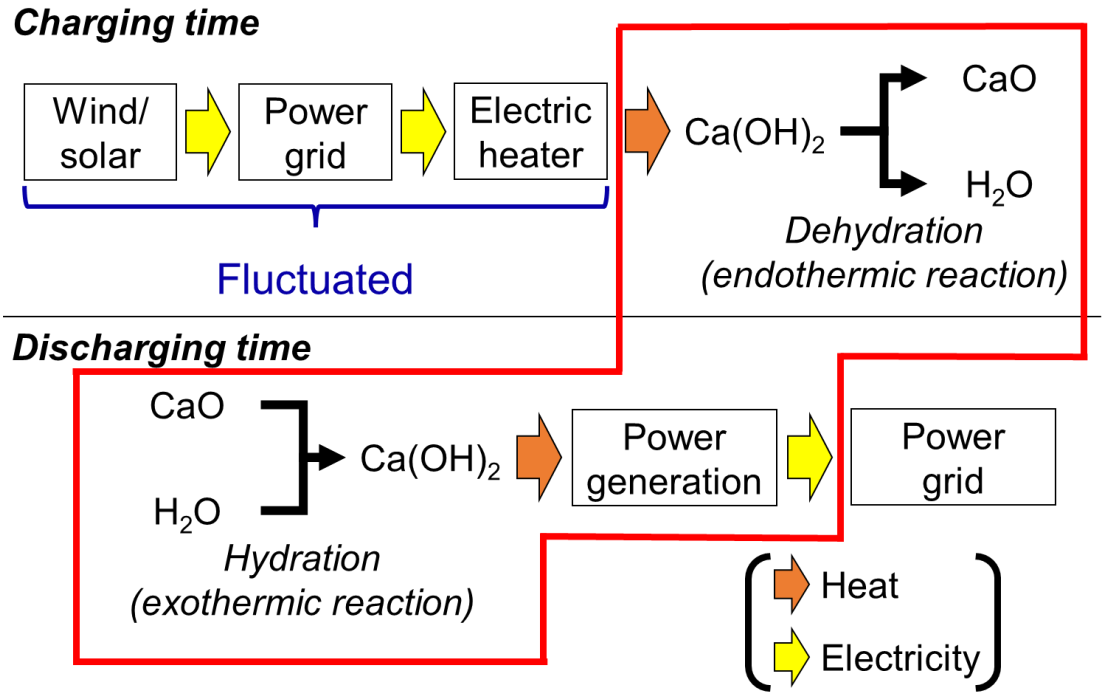

Figure 1.26 The boundary of Chapters 3 and 4

Chapter 2

Absorption of VRE Fluctuation by a Fluidized Bed Reactor for a TCS System using $CaO/Ca(OH)_2$/Alumina

2.1. Abstract

A simplified dynamic model of a $CaO/Ca(OH)_2$–containing fluidized bed reactor was developed by combining a continuously stirred tank reactor (CSTR) model in the solid phase with a series of CSTRs in the gas phase for mass transport. The heat supplied to the TCS system was allowed to fluctuate to evaluate the absorption of the VRE fluctuation. In addition, the performance of the fluidized bed was assessed using nitrogen or steam as the fluidizing gas. For nitrogen, the fluctuation of bed temperature increased with the increasing time step of heat change. The bed temperature was affected by the magnitude of the fluctuation of the supplied heat more strongly for nitrogen than for steam, mainly because the rate of dehydration under these conditions was more strongly dependent on temperature than in the case of steam. The TCS efficiency (calculated by considering reaction heat) and energy storage efficiency (calculated by considering reaction heat and sensible heat) equaled 14.1% and 34.1% for steam and 29.9% and 62.7% for nitrogen, respectively. The differences between the efficiencies for steam and nitrogen were ascribed to the latent heat of H_2O. Sensitivity analyses showed that both efficiencies increased with increasing heat supply because of the concomitant decrease in the time required to heat the system to the reaction temperature. During this time, thermochemical heat storage did not occur, which resulted in lower efficiency. Therefore, the fluctuation from VRE can be absorbed by using a fluidized bed reactor for the TCS system.

2.2. Dynamic Model of a Fluidized Bed Reactor

2.2.1. Fluidized Bed Model

Figure 2.1 shows a schematic model of the reactor. To simplify the model, the fluidized bed was divided into solid and gas phases. The solid phase was assumed to be perfectly mixed, and the gas phase was treated as a series of CSTR type cells for mass transport [116,152]. It was assumed that the gas and solids contact at the interface of the two phases sufficiently. Moreover, the solid and gas phase temperatures were assumed to be uniform. The total number of cells and the number of a given individual cell were denoted as N [-] and i [-], respectively. The fluidizing and reactant gases were preheated by receiving $q_{\mathrm{preheating}}$ [W] and then fed into the gas phase. The heat from an external heat source, q_{reactor} [W], was equally supplied to the N cells of the gas phase. In the i^{th} cell of the gas phase (see Figure 2.1 (b)), the gas received a heat input of q_{reactor}/N [W] and left this cell, which resulted in a temperature increase from $T_{\mathrm{r},i-1,t}$ [K] to $T_{\mathrm{r},i,t}$ [K].

Note that a fluidized bed has two phases called emulsion and bubble phases in the fluidized bed model such as two-region models and K-L model (described in section 1.3.2). However, in the dynamic model of this study, the solid and gas phases were assumed. In two-region model and K-L model, the mass transfer between the emulsion and bubble phases are considered, and the steam in the emulsion phase are reacted with the solid reactants in the emulsion phase. On the other hands, in this dynamic model, the mass transfer was not contained, and the steam partial pressure of gas phase are used for calculation of reaction kinetics.

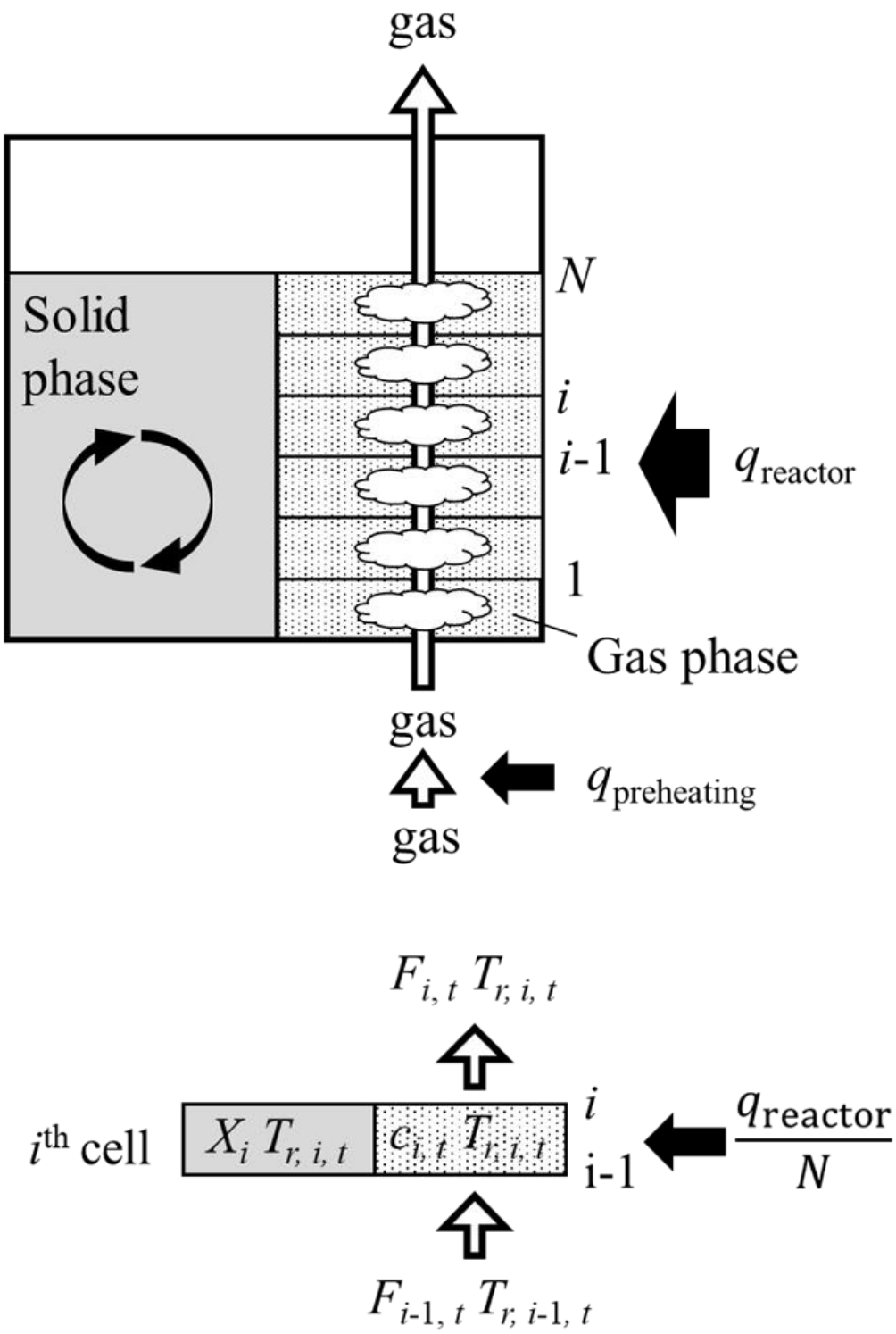

Figure 2.1 Schematics of the employed fluidized bed model (a) Overview for mass transport and (b) heat transport in i^{th} cell

2.2.2. Governing Equations

The mass balances of the solid and gas phases can be written as follows. The mass balance of the whole solid phase (containing alumina particles) is given by eqs. (2.1)–(2.3).

$$\frac{\partial n_{\mathrm{CaO}}}{\partial t} = \frac{n_{\mathrm{Ca}}}{N}\sum_{i=0}^{N}\left(\frac{\mathrm{d}X_i}{\mathrm{d}t}\right) \quad (2.1)$$

$$\frac{\partial n_{\mathrm{Ca(OH)_2}}}{\partial t} = -\frac{n_{\mathrm{Ca}}}{N}\sum_{i=0}^{N}\left(\frac{\mathrm{d}X_i}{\mathrm{d}t}\right) \quad (2.2)$$

$$\frac{\partial n_{\mathrm{alumina}}}{\partial t} = 0 \quad (2.3)$$

The mass balance of the gas phase in cell *i* is given by eqs. (2.4), (2.5).

$$A_{\mathrm{B}}\mathrm{d}z v_{\mathrm{g}}\frac{\partial c_{\mathrm{H_2O},i}}{\partial t} = F_{\mathrm{H_2O},i-1,t} - F_{\mathrm{H_2O},i,t} + \frac{n_{\mathrm{Ca}}}{N}\frac{\mathrm{d}X_i}{\mathrm{d}t} \quad (2.4)$$

$$A_{\mathrm{B}}\mathrm{d}z v_{\mathrm{g}}\frac{\partial c_{\mathrm{N_2},i}}{\partial t} = F_{\mathrm{N_2},i-1,t} - F_{\mathrm{N_2},i,t} \quad (2.5)$$

where n is the molar weight [mol], t is the time [s], $\mathrm{d}X_i/\mathrm{d}t$ is the reaction rate [s^{-1}] (see section 2.2.3), A_{B} is the cross-sectional area of the reactor [m^2], $\mathrm{d}z$ is the height of each cell [m], v_{g} is the voidage [-], c is the gas concentration [mol/m^3], and F is the gas molar flow rate [mol/s]. The heat balance in the i^{th} cell is given by eq. (2.6).

$$\left\{\sum_{\mathrm{solid}}\left(n\frac{1}{N}c_{\mathrm{p}}\right) + \sum_{\mathrm{gas}}\left(c_{t,i}A_{\mathrm{B}}\mathrm{d}z v_{\mathrm{g}}c_{\mathrm{p}}\right)\right\}\frac{\partial T_{\mathrm{r},i}}{\partial t} = F_{\mathrm{H_2O},i-1,t}c_{\mathrm{p,H_2O},i-1}T_{\mathrm{r},i-1,t} -$$

$$F_{\mathrm{H_2O},i,t}c_{\mathrm{p,H_2O},i}T_{\mathrm{r},i,t} + F_{\mathrm{N_2},i-1,t}c_{\mathrm{p,N_2},i-1}T_{\mathrm{r},i-1,t} - F_{\mathrm{N_2},i,t}c_{\mathrm{p,N_2},i}T_{\mathrm{r},i,t} + \frac{n_{\mathrm{Ca}}}{N}\frac{\mathrm{d}X_i}{\mathrm{d}t}\Delta H_{\mathrm{r}} + \frac{q_{\mathrm{reactor}}}{N}$$

(2.6)

where c_{p} is the specific heat capacity [J/(mol·K)], T is the temperature [K], and q_{reactor} is the external heat from the reactor wall [W]. These balance equations were solved by using the following relationships:

$$p_{\mathrm{r},i} = p_{\mathrm{in}} - \rho_{\mathrm{solid}}g\mathrm{d}zi \quad (2.7)$$

$$p_{\mathrm{r},i} = p_{\mathrm{H_2O},i,t+\mathrm{d}t} + p_{\mathrm{N_2},i,t+\mathrm{d}t} \quad (2.8)$$

$$p_{\mathrm{H_2O},i,t+\mathrm{d}t} = c_{\mathrm{H_2O},i,t+\mathrm{d}t}RT_{\mathrm{r},i,t+\mathrm{d}t} \quad (2.9)$$

$$p_{\mathrm{N_2},i,t+\mathrm{d}t} = c_{\mathrm{N_2},i,t+\mathrm{d}t}RT_{\mathrm{r},i,t+\mathrm{d}t} \quad (2.10)$$

$$c_{\mathrm{H_2O},i,t} = \frac{F_{\mathrm{H_2O},i,t}}{F_{\mathrm{N_2},i,t}} c_{\mathrm{N_2},i,t} \qquad (2.11)$$

where p is pressure [Pa], g is the gravitational acceleration [m/s^2], and R is the universal gas constant [J/(mol·K)]. Eq. (2.7) represents only the pressure drop in the fluidized bed, and the pressure changes attributed to the reaction did not occur. Eq. (2.8) was derived from Dalton's law. In this study, the gas was assumed to be ideal (eqs. (2.9) and (2.10)). Eq. (2.11) was obtained by assuming the same ratio of gas concentration and outlet gas flow rate for each cell. In addition, eq. (2.12) was used to maintain a uniform reactor temperature.

$$\left[\sum_{\mathrm{Solid}}\left(nc_{\mathrm{p}}\right) + \sum_{i=1}^{N}\left\{\sum_{\mathrm{gas}}\left(c_{t,i}A_{\mathrm{B}}\mathrm{d}zv_{\mathrm{g}}c_{\mathrm{p}}\right)\right\}\right]\left(T_{\mathrm{r},t+\mathrm{d}t} - T_{\mathrm{r},t}\right) = \sum_{i=1}^{N}\left[\left\{\sum_{\mathrm{solid}}\left(\frac{n}{N}c_{\mathrm{p}}\right) + \sum_{\mathrm{gas}}\left(c_{i,t}A_{\mathrm{B}}\mathrm{d}zv_{\mathrm{g}}c_{\mathrm{p}}\right)\right\}\left(T_{\mathrm{r},i,t+\mathrm{d}t} - T_{\mathrm{r},i,t}\right)\right] \qquad (2.12)$$

Two variables ($n_{\mathrm{CaO},\ t+\mathrm{d}t}$ and $n_{\mathrm{Ca(OH)2},\ t+\mathrm{d}t}$) were calculated using eqs. (2.1) and (2.2), and eight variables ($c_{\mathrm{H2O},\ i,\ t+\mathrm{d}t}$, $c_{\mathrm{N2},\ i,\ t+\mathrm{d}t}$, $F_{\mathrm{H2O},\ i,\ t+\mathrm{d}t}$, $F_{\mathrm{N2},\ i,\ t+\mathrm{d}t}$, $T_{\mathrm{r},\ i,\ t+\mathrm{d}t}$, $p_{\mathrm{r},\ i}$, $p_{\mathrm{H2O},\ i,\ \mathrm{t}+\mathrm{d}t}$, and $p_{\mathrm{N2},\ i,\ t+\mathrm{d}t}$) were calculated using eqs. (2.4)–(2.11). These equations were solved by using Visual Basic for Applications® (version 7.1). The details of the calculation were described in Appendix 2.1 and 2.2.

2.2.3. Reaction Kinetics

For nitrogen as a fluidizing gas, it was assumed that all particles had almost identical sizes, and the kinetic equations of dehydration and hydration proposed by Schaube et al. [28] were used. The pressure was maintained at < 0.13 MPa, although the above equations were applicable at $p \leq 0.1$ MPa.

For $X < 0.2$ (dehydration),

$$\frac{\mathrm{d}X}{\mathrm{d}t} = 1.9425 \times 10^{12} \exp\left(-\frac{187.88 \times 10^3}{RT}\right)\left(1 - \frac{p}{p_{\mathrm{eq}}}\right)^3 (1 - X) \qquad (2.13)$$

For $X > 0.2$ (dehydration),

$$\frac{\mathrm{d}X}{\mathrm{d}t} = 8.9588 \times 10^{9} \exp\left(-\frac{162.62 \times 10^3}{RT}\right)\left(1 - \frac{p}{p_{\mathrm{eq}}}\right)^3 2(1 - X)^{0.5} \qquad (2.14)$$

where X is the conversion ratio defined in eq. (2.15).

$$X = \frac{n_{\mathrm{CaO}}}{n_{\mathrm{Ca(OH)_2}} + n_{\mathrm{CaO}}} \times 100 \qquad (2.15)$$

and p_{eq} is steam pressure at equilibrium.

For $T_{\mathrm{eq}} - T \geq 50$ (hydration),

$$\frac{\mathrm{d}X}{\mathrm{d}t} = -13945 \exp\left(-\frac{89.486 \times 10^3}{RT}\right)\left(\frac{p}{p_{\mathrm{eq}}} - 1\right)^{0.83} 3(1 - X)[-\ln(1 - X)]^{0.666} \qquad (2.16)$$

For $T_{\mathrm{eq}} - T < 50$ (hydration),

$$\frac{\mathrm{d}X}{\mathrm{d}t} = -1.0004 \times 10^{-34} \exp\left(\frac{53.332 \times 10^3}{RT}\right)\left(\frac{p}{10^5}\right)^6 (1 - X), p > p_{\mathrm{eq}} \qquad (2.17)$$

where T_{eq} is the temperature at equilibrium. The relation between pressure and temperature at equilibrium is given by eq. (2.18).

$$\ln \frac{p_{\mathrm{eq}}}{10^5} = \frac{12845}{T_{\mathrm{eq}}} + 16.508 \qquad (2.18)$$

Because the above equations describing hydration rate have a sharp transition, the averaging function proposed by Stöhle et al. [112] was used to afford a smooth transition.

For steam as a fluidizing gas, the kinetic equations of dehydration and hydration proposed by Angerer et al. [35] were used because the applied range of steam partial pressure

were close although inert particles were different.

For dehydration,

$$p_{\mathrm{onset,dehy}} = \exp\left(-\frac{13090}{T} + 16.443\right) \quad (2.19)$$

$$\frac{\mathrm{d}X}{\mathrm{d}t} = -449974\exp\left(-\frac{91282}{RT}\right)\left(1 - \min\left\{\frac{\frac{1}{p}}{p_{\mathrm{onset,dehy}}}\right\}\right)^{3.47} X \quad (2.20)$$

For hydration,

$$p_{\mathrm{onset,hy}} = \exp\left(-\frac{9713.3}{T} + 12.725\right) \quad (2.21)$$

$$\frac{\mathrm{d}X}{\mathrm{d}t} = 390827\exp\left(-\frac{87460}{RT}\right)\left(1 - \max\left\{\frac{\frac{1}{p}}{p_{\mathrm{onset,hy}}}\right\}\right)^{3.43} (1 - X) \quad (2.22)$$

2.2.4. Calculation Methods and Parameters

The flowchart of the dynamic model calculation is shown in Figure 2.2. To validate the model, the author compared the predicted results with lab-scale experimental data [29], with the calculation parameters summarized in Tables 2.1–2.3. The value of q_{reactor} during dehydration was calculated using eq. (2.23).

$$q_{\text{reactor}} = U\pi D_{\text{B}} H_{\text{B}} \Delta T = 300 \times \pi D_{\text{B}} H_{\text{B}} \times 20 = 802\ \text{W} \qquad (2.23)$$

where D_{B} is the internal diameter of the reactor [m], H_{B} is the height of the fluidized bed [m], and U is the coefficient of overall heat transfer between the wall and the bed, which was assumed to equal 300 W/(m^2·K) [116]. The temperature difference between the wall and the bed (ΔT) was assumed to equal 20 °C (see Figure 2.4). All specific heat capacities and production enthalpies were calculated using data from the National Institute of Standards and Technology (NIST) Chemistry Webbook [153].

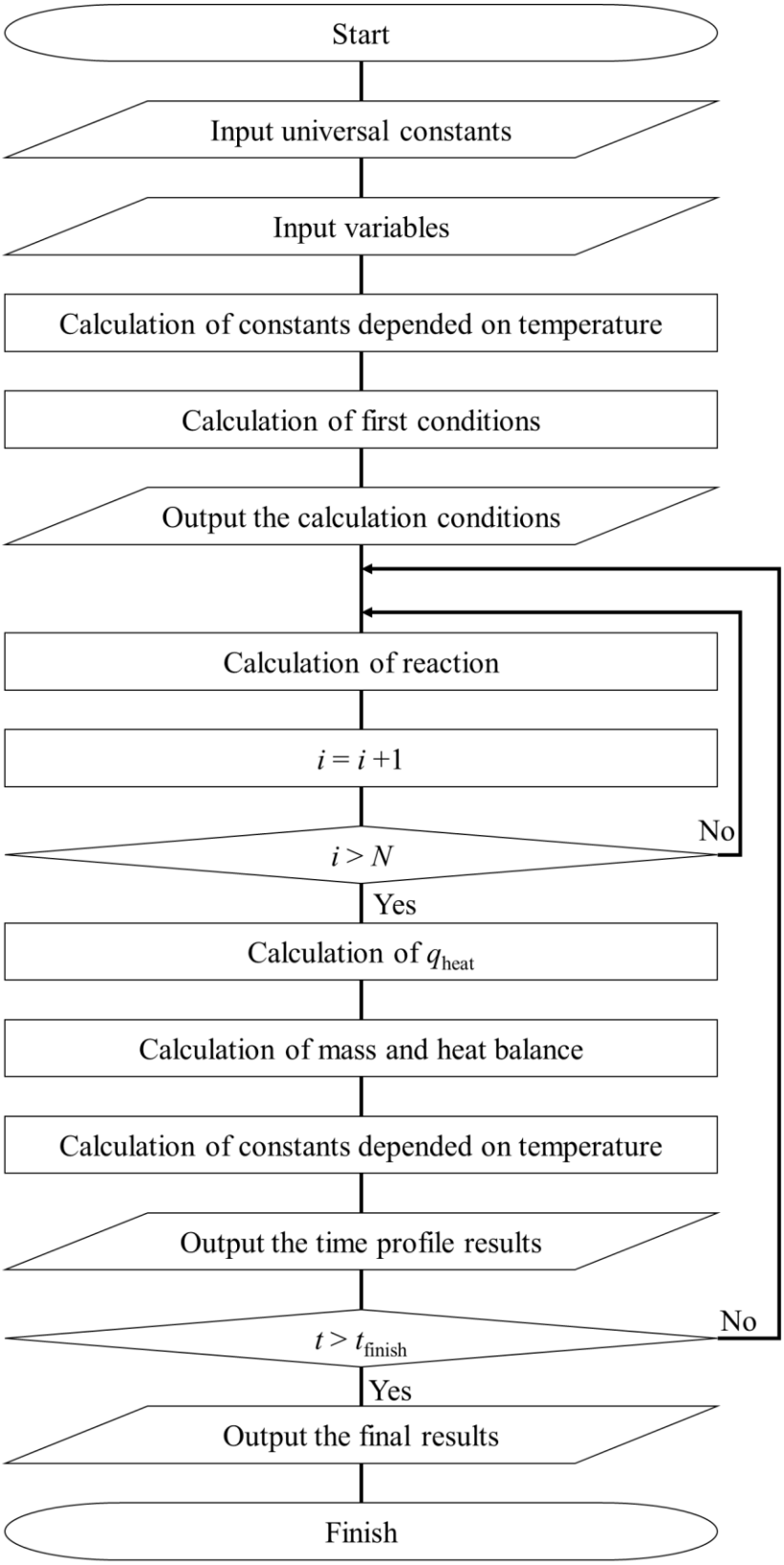

Figure 2.2 The flowchart of the calculation of the dynamic model

Table 2.1 Calculation parameters (physical data)

	Unit	$Ca(OH)_2$	CaO	Alumina	H_2O	N_2
True density of particles [29]	kg/m^3	2240	3300	3970	–	–
Bulk density of particles in the fixed bed [29]	kg/m^3	490	650	736	–	–
Molecular weight [154]	g/mol	74	56	102	18	28
Standard enthalpy of formation [154]	kJ/mol	−986.09	−635.09	–	–241.83	–
Particle size [29]	μm	3.8	3.8	171.7	–	–

Table 2.2 Calculation parameters (experimental conditions [29]**)**

	Unit	Dehydration	Hydration
$Ca(OH)_2$	mol	7.8	0
CaO	mol	0	7.8
Alumina content	wt%	70	70
Initial bed temperature	°C	325	345
Nitrogen flow rate	Nm^3/h	2	2
Steam flow rate	kg/h	0	0.49
Gas temperature at inlet	°C	300	300
Gas pressure at inlet	kPa	133	134
Diameter of the reactor	m	0.114	0.114
$q_{reactor}$ during reaction	W	802[*1]	−400, −500, −650[*2]

[*1]See eq. (2.23)

[*2]Negative values indicate an exothermic reaction.

Table 2.3 Calculation parameters (other)

	Unit	Value
Bed expansion [35]	%	125
Time step, dt	s	0.01
N[*1]	–	10
Pressure loss of gas distributor [35]	Pa	2.0×10^4

[*1]See section 2.3.1

2.2.5. Evaluation Methods

VRE fluctuations were modeled as eq. (2.24).

$$q_{\mathrm{heat}} = \mathrm{Int}\{(q_{\mathrm{fluctuation}} + 1) \times random + q_{\mathrm{min}}\} \quad (2.24)$$

where $q_{\mathrm{fluctuation}}$ is the magnitude of the VRE fluctuation [W], *random* is a random number greater or equal to zero and less than one [-], and q_{min} is the lowest value of q_{heat} [W]. The value of *random* was changed every second (t_{change} [s]). "Int" refers to the operation of rounding down, and q_{heat} is used to increase the temperature of the reactor (q_{reactor}) and preheat the fluidizing gas ($q_{\mathrm{preheating}}$) [W].

$$q_{\mathrm{heat}} = q_{\mathrm{reactor}} + q_{\mathrm{preheating}} \quad (2.25)$$

The input fluctuation affects only q_{reactor}, and the heat externally supplied to keep the inlet gas temperature constant (Table 2.4). Table 2.4 show the t_{change}, $q_{\mathrm{fluctuation}}$, and q_{min} for each case. In the case of Base-1, q_{heat} (or q_{min}) was set to 1000 W, a value close to that of (q_{reactor} of the dehydration model validation + $q_{\mathrm{preheating}}$). Note that q_{heat} was identical to $q_{\mathrm{preheating}}$ after the reaction was complete. The other parameters were identical to those used for model validation.

The dynamic performance of the reactor was qualitatively evaluated using $\Delta T_{\mathrm{total}}$ [K], defined as

$$\Delta T_{\mathrm{total}} = \sum \left| T_{\mathrm{r},t+\mathrm{d}t} - T_{\mathrm{r},t} \right| \quad (2.26)$$

where t_{finish} is the time of reaction completion [s], and $\Delta T_{\mathrm{total}}$ represents the summations of the absolute bed temperature changes. $\Delta T_{\mathrm{total}}$ is positively correlated with fluctuation magnitude, even though this magnitude (fluctuation temperature range) is not considered in the above expression.

Reactor performance was evaluated by using TCS efficiency, η_{chemical} [%] and energy storage efficiency, η_{storage} [%], which are defined in eqs. (2.27) and (2.28), respectively. The former parameter is determined only by the endothermic reaction heat, whereas the latter

parameter is determined by both the endothermic reaction heat and sensible heat in solids. This is also viewed as stored energy if the reactor is well insulated or the storage time is very short.

$$\eta_{\mathrm{chemical}} = \frac{Q_{\mathrm{chemical}}}{Q_{\mathrm{heat}}+\mathrm{Q_{s,preheat}}} \times 100\% \qquad (2.27)$$

$$\eta_{\mathrm{storage}} = \frac{Q_{\mathrm{chemical}}+\mathrm{Q_{s,finish}}}{Q_{\mathrm{heat}}+\mathrm{Q_{s,preheat}}} \times 100\% \qquad (2.28)$$

where Q_{chemical} is the heat stored as thermochemical heat (i.e., the heat of the endothermic reaction) [MJ], Q_{heat} is the integral value of q_{heat} from 0 to t_{finish} [MJ], $Q_{\mathrm{s,preheat}}$ is the sensible heat of preheating solids from the ambient temperature to the initial temperature [MJ], and $Q_{\mathrm{s,finish}}$ is the sensible heat of the solid heated from ambient temperature to the final temperature at t_{finish} [MJ]. The efficiencies were calculated at t_{finish}.

Table 2.4 Calculation parameters used for the case of nitrogen as a fluidizing gas

Case	t_{change} [s]	$q_{\mathrm{fluctuation}}$ [W]	q_{min} [W]
Base-1	0	0	1000
1	1	400	800
2	60	400	800
3	120	400	800
4	60	600	700
5	60	800	600
6	60	1000	500

2.3. Results and Discussion

2.3.1. Effects of N for Calculation of Bed Temperature

Firstly, the effects of N were investigated. The results are shown in Figure 2.3. The results show that the time profile in the case of $N = 1$ was different from other results. As N was larger than 5, the time profile was almost the same. Thus, the calculations of this dissertation were carried out as N is 10.

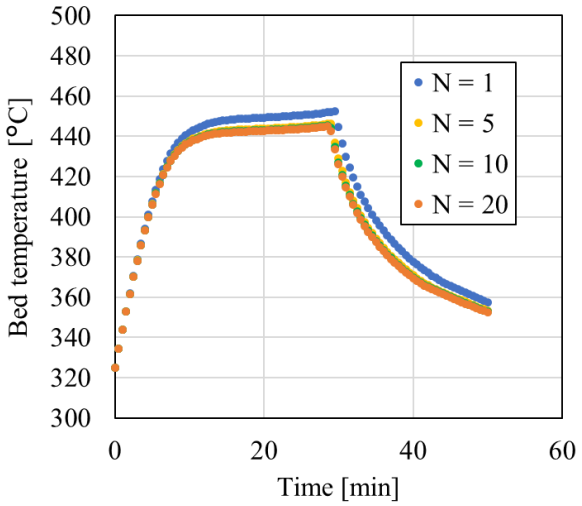

Figure 2.3 The effects of *N* for calculation of bed temperature (*N* = 1, 5, 10, 20)

2.3.2. Model Validation

Figures 2.4 and 2.5 show the experimental [29] and calculated results for dehydration and hydration, respectively. In the dehydration experiment (Figures 2.4 (a) and (b)) [29], solids were slowly preheated by the electric heater (250 °C/h) to 330 °C. The flow rate of nitrogen was set to 2.26 kg/h, and its temperature equaled 300 °C, whereas the inlet steam flow equaled 0 kg/h. At 119 min, the reactor wall temperature (T_w) was raised to 480 °C at 30 °C/min and then held constant (± 2 °C). The bed temperature was lower than the wall temperature because dehydration is an endothermic reaction. The outlet flow rate of steam increased to 0.33 kg/h because of the dehydration of $Ca(OH)_2$ and then decreased. However, some particles were entrained and captured by the filters. The filters were cleaned at 151 and 158 min, and the particles were returned to the reactor. Thus, the outlet flow rate of steam increased dramatically at 151 and 158 min. The reaction time was 51 min (between 119 and 170 min). Hydration experiments were carried out after dehydration (Figures 2.5 (a) and (b)). The wall temperature was set to 350 °C, and the bed temperature was 345 °C. At 203 min, inlet nitrogen and steam flow rates were set to 2.26 and 0.49 kg/h, respectively. The bed temperature increased to 385 °C and exceeded the wall temperature because the hydration reaction is exothermic. Upon the onset of hydration, the outlet steam flow rate markedly decreased and then gradually increased. The reaction time equaled 28 min (between 204 and 232 min). The simulation of dehydration (Figures 2.4 (c) and (d)) afforded a reaction time and maximum temperature that were lower than experimental values by 10 min and 20 °C, respectively. The lower calculated reaction time was ascribed to the fact that our model did not consider particle entrainment. Figures 2.5 (c) and (d) present the simulated hydration results for heat losses of 400, 500, and 650 W, revealing a large initial drop in bed temperature due to the fact that the heat loss was constant. This heat loss was assumed to equal 400–500 W, as evaluated by Criado et al. [119], who used a device similar to that of Pardo et al. [29]. In the case of 400 W, the simulated reaction temperature was

identical to the experimental one, although the simulated reaction time was longer than the experimental value. At a heat loss of 650 W, the reaction time matched the experimental value, although the reaction temperature was underestimated by 20 °C. The calculated mass flow rate of steam was constant during the reaction. Schaube et al. reported that the bed temperature of some systems strongly decreased in a fixed-bed reactor model [108], which was ascribed to a restriction of the reaction rate in a 60 g powder bed. These authors used the same reaction rate equation (Schaube et al. [28]) derived by thermogravimetry for a 10 mg sample. Our reference experiments used a solid mass of 1.93 kg (1.35 kg-alumina) [29]. Thus, a similar restriction caused a dramatic decrease.

The discrepancies between experimental and calculated results were rationalized as follows. First, in our model, the fluidized bed was divided into solid and gas phases, and the rates of mass and heat transfer between the phases were assumed to be sufficiently fast. Conversely, in the K-L model, which is widely used to describe fluidized beds [119], the fluidized bed is divided into emulsion, cloud + wake, and bubble phases, and the rates of mass and heat transfer between the phases are considered. For slow gas-solid reactions, the reaction proceeds mainly in the emulsion phase. Second, this system contained alumina particles whose thermal conductivity exceeds that of $Ca(OH)_2$ or CaO. Thus, this thermal conductivity strongly influences the reaction. Third, one should consider the effects of $Ca(OH)_2$ and/or CaO agglomeration. Fourth, although a fluidized bed reactor was used, the author employed the kinetic equations derived by thermogravimetry. These phenomena are complexly intertwined, and no clear explanation is available. However, the adopted model was sufficient to represent the behavior of a fluidized bed in a non-steady state and evaluate its performance. In addition, it takes only 10 s in real time to calculate the performance of the fluidized bed for 50 min.

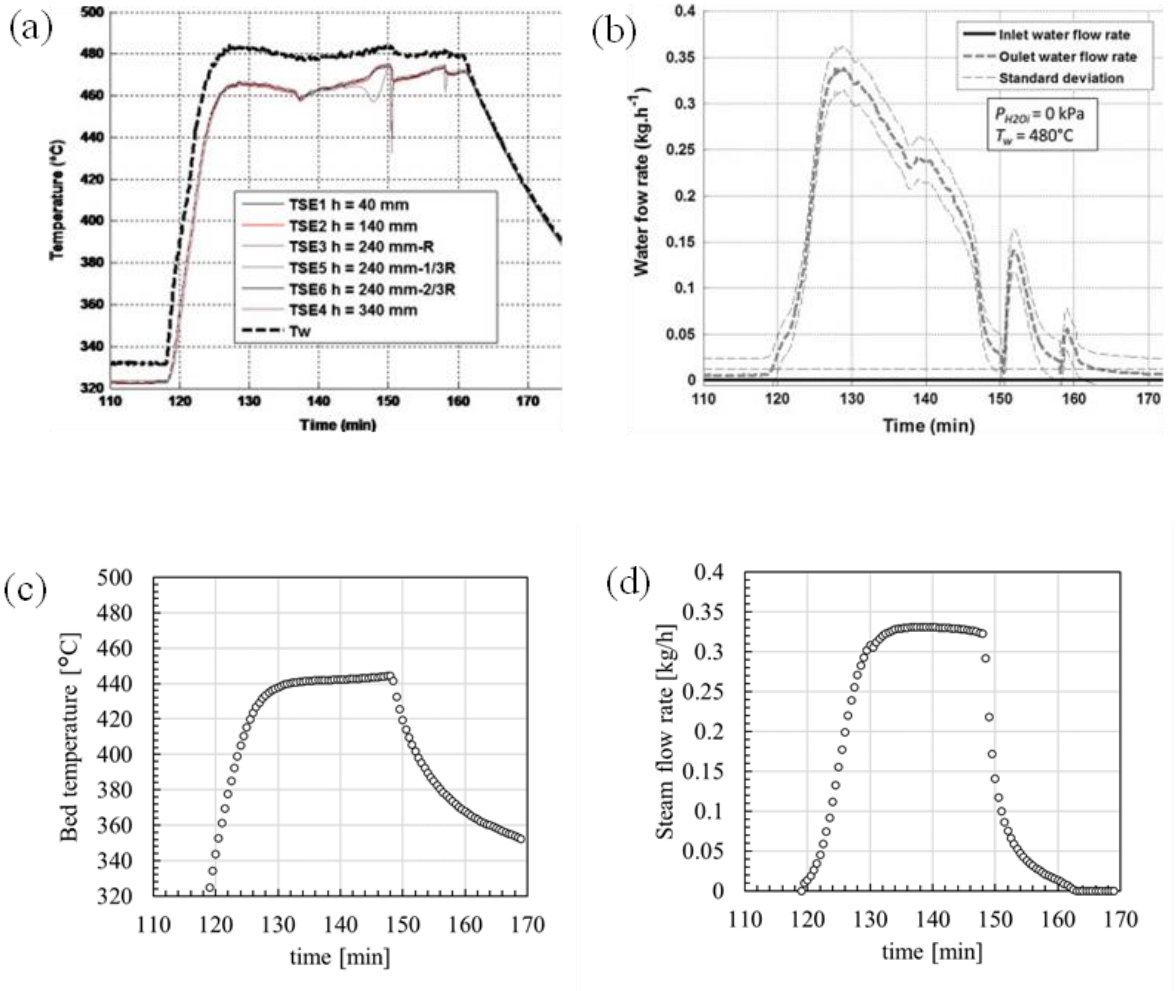

Figure 2.4 (a, c) Bed temperatures and (b, d) mass flow rates of steam determined for dehydration (a, b) experimentally [29] and (c, d) using a numerical model

Reprinted with permission from ref. [29]. Copyright (2014) Elsevier B.V.

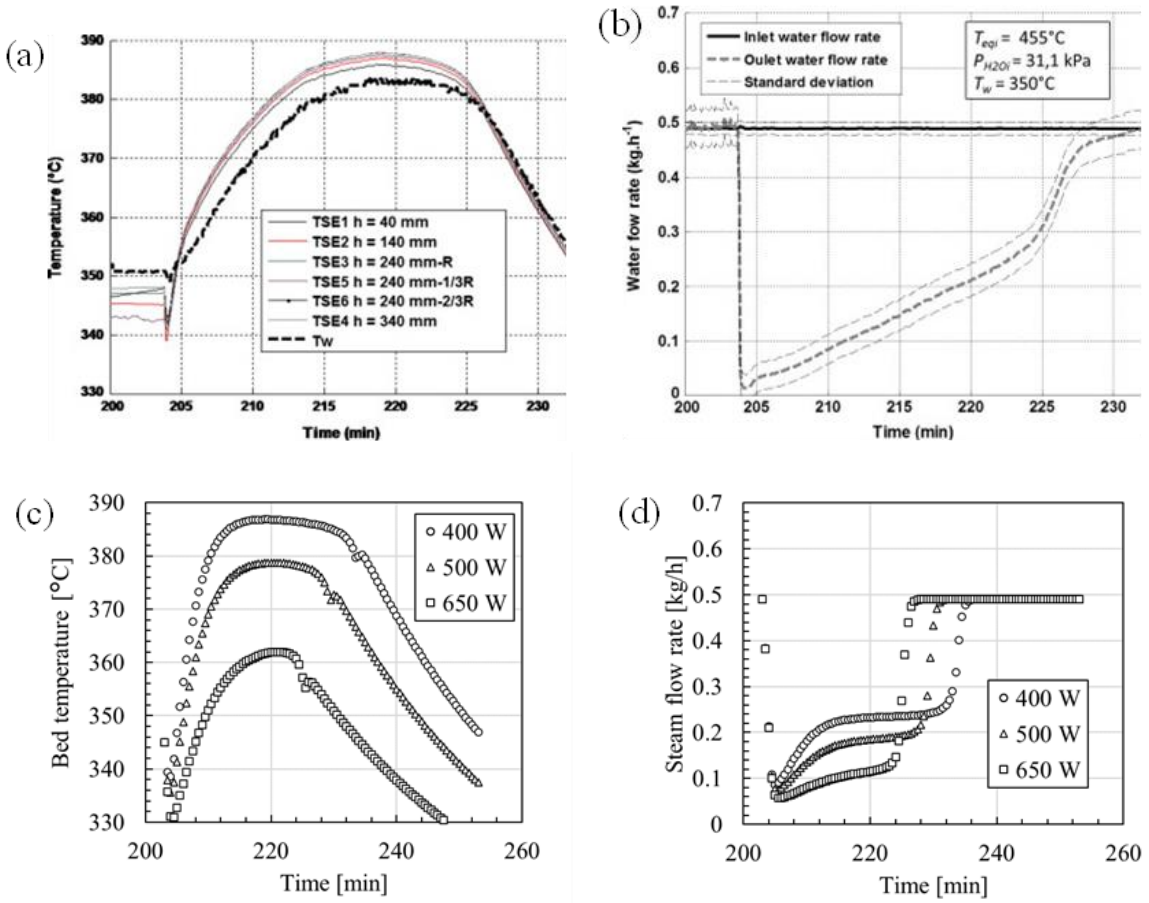

Figure 2.5 (a, c) Bed temperatures and (b, d) mass flow rates of steam determined for hydration at various heat losses from the reactor (a, b) experimentally [29] and (c, d) using a numerical model

2.3.3. Fluctuation Absorption (nitrogen as fluidizing gas)

The calculated results of the bed temperature fluctuation are shown in Figure 2.6. In addition, t_{finish}, q_{ave} (average of q_{heat}), ΔT_{total}, and the two energy efficiencies are listed in Table 2.5. In scenario Base-1, the bed was heated from 0 min, and the temperature increased to 440 °C. The bed temperature slightly increased during the dehydration reaction. The reactor heating stopped at t_{finish}, and the bed temperature decreased. The results of cases 1–3 show that the bed temperature widely fluctuated with increasing t_{change}. For t_{change} = 1 s (case 1), the fluctuation of heat supply had little effect on the bed temperature. The effects of increasing and decreasing bed temperature were canceled out because q_{heat} was changed every 1 s. For t_{change} = 60 and 120 s (cases 2 and 3, respectively), bed temperature fluctuated around 440 °C, with the fluctuation of case 3 exceeding that of case 2. In this case, the effects of increasing and decreasing bed temperature were not canceled out because the cycle of heat value change (t_{change}) was long. However, ΔT_{total} decreased with increasing t_{change} because the bed temperature significantly changed immediately after the change in q_{heat}. A slight decrease in t_{finish} and a slight increase in $\eta_{chemical}$ and $\eta_{storage}$ were observed with increasing q_{ave} (see Table 2.5). In fact, q_{ave} also had to change because of the VRE fluctuation. Therefore, even for t_{change} = 1 s, the bed temperature had to change under real conditions because of the change in q_{ave}. The above values were influenced by q_{heat} (or q_{ave}), as described in Section 2.3.5.

For the cases of Base-1, 2, and 4–6, ΔT_{total} increased with increasing magnitude of heating fluctuation, with the underlying reason described in section 2.3.4. Notably, t_{finish}, $\eta_{chemical}$, and $\eta_{storage}$ did not change significantly and were influenced by q_{ave}. When the bed temperature fluctuated, the outlet gas temperature also fluctuated because the temperature of the gas and solid phase was assumed to be uniform. For Base-1, $\eta_{storage}$ equaled 62.7%, indicating that the outlet gas carried the remaining 37.3% of energy. When energy is used for heating in other processes, temperature fluctuation can be a serious problem.

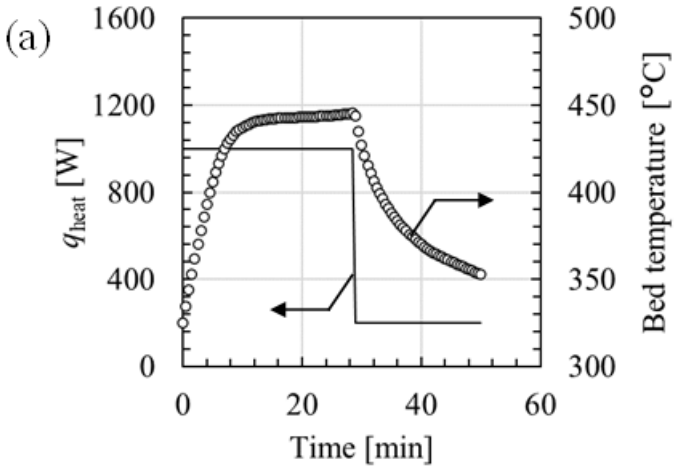
(a)
1600
1200
800
400
0
q_{heat} [W]
500
450
400
350
300
Bed temperature [°C]
0
20
40
60
Time [min]

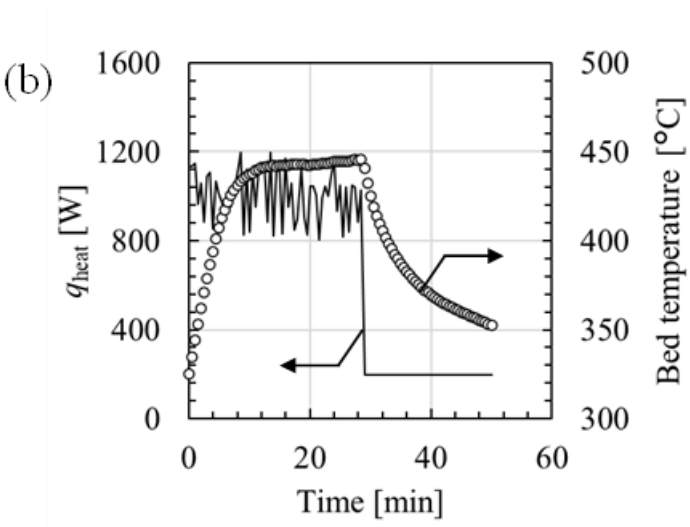
(b)
1600
1200
800
400
0
q_{heat} [W]
500
450
400
350
300
Bed temperature [°C]
0
20
40
60
Time [min]

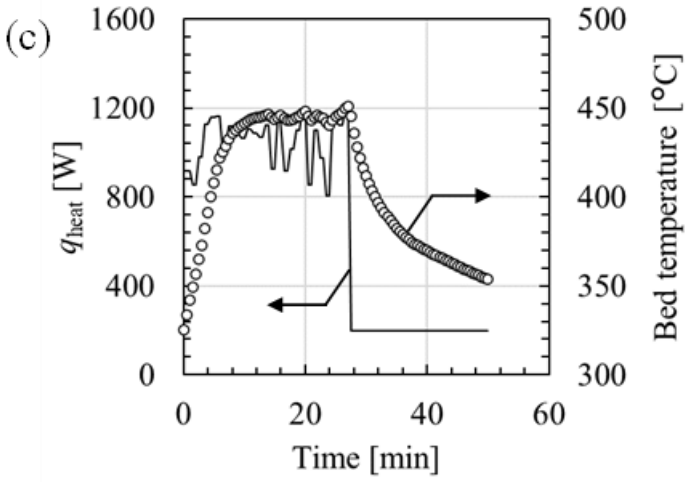
(c)
1600
1200
800
400
0
q_{heat} [W]
500
450
400
350
300
Bed temperature [°C]
0
20
40
60
Time [min]

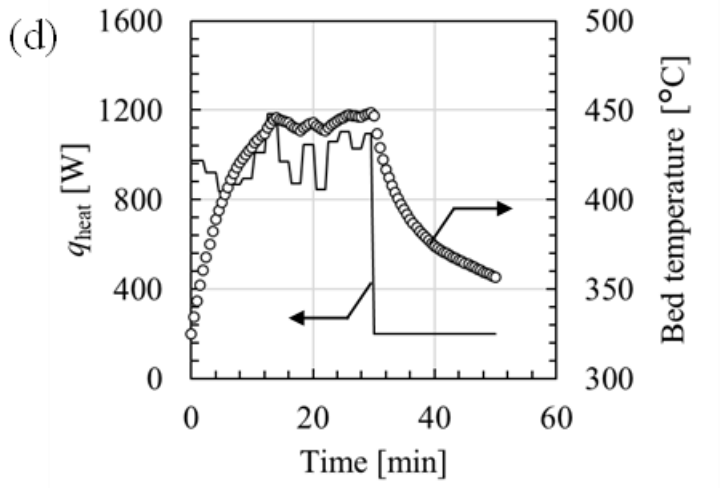
(d)
1600
1200
800
400
0
q_{heat} [W]
500
450
400
350
300
Bed temperature [°C]
0
20
40
60
Time [min]

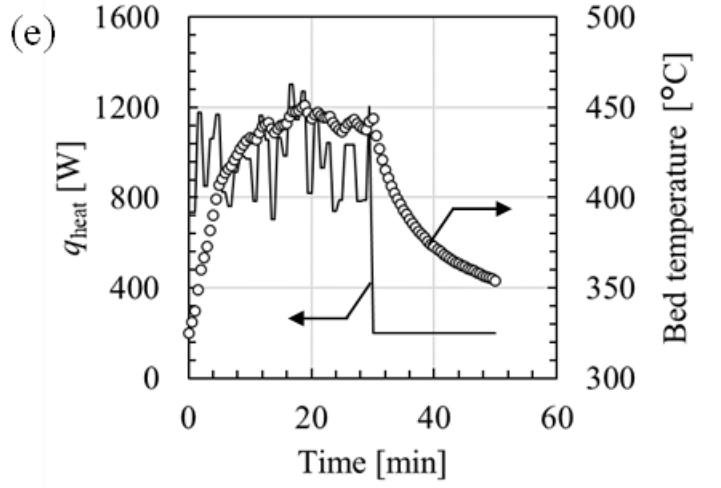
(e)
1600
1200
800
400
0
q_{heat} [W]
500
450
400
350
300
Bed temperature [°C]
0
20
40
60
Time [min]

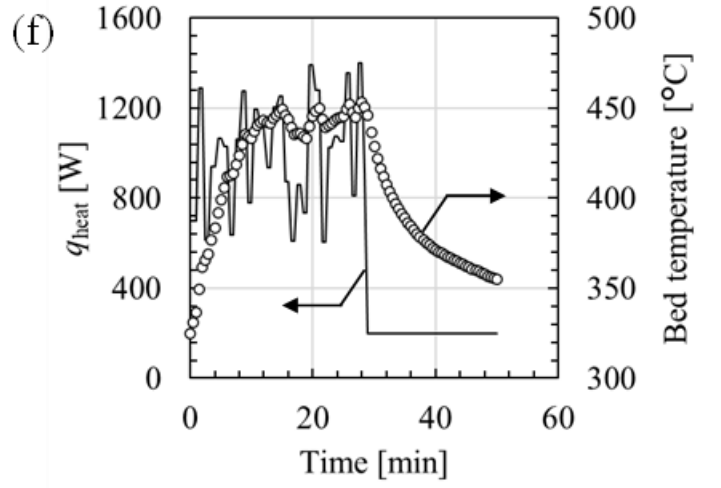
(f)
1600
1200
800
400
0
q_{heat} [W]
500
450
400
350
300
Bed temperature [°C]
0
20
40
60
Time [min]

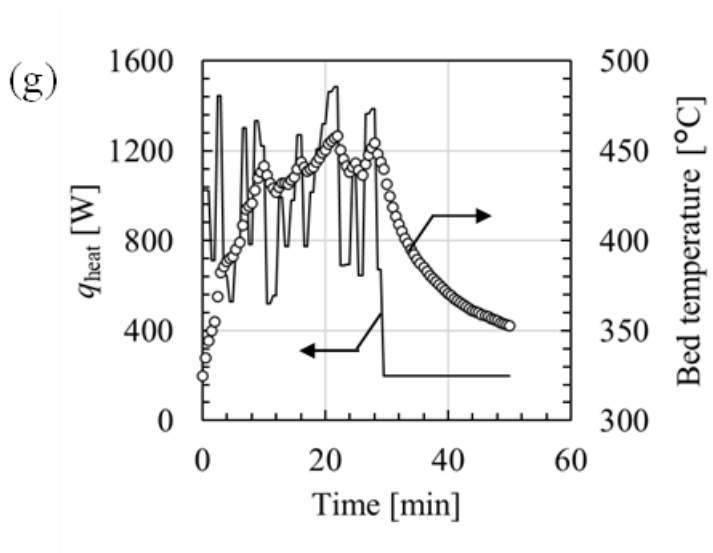

Figure 2.6 Evolution of calculated q_{heat} and fluidized bed temperature with time in the case of nitrogen (a) Base-1, (b) case 1, (c) case 2, (d) case 3, (e) case 4, (f) case 5, and (g) case 6

Table 2.5 Reaction performance metrics obtained for various cases

Case	Fluidizing gas	t_{finish} [min]	q_{ave} [kW_{th}]	ΔT_{total} [K]	$\eta_{chemical}$ [%]	$\eta_{storage}$ [%]
Base-1	Nitrogen	28.9	1.00	121	29.9	62.7
1	Nitrogen	28.8	1.00	164	29.9	62.7
2	Nitrogen	27.3	1.05	159	30.1	63.5
3	Nitrogen	29.9	0.98	150	29.6	62.4
4	Nitrogen	29.9	0.97	182	29.7	62.2
5	Nitrogen	28.9	1.00	209	29.8	62.8
6	Nitrogen	29.3	0.99	235	29.7	62.6
Base-2	Steam	29.8	2.40	219	14.1	34.1
7	Steam	29.0	2.42	228	14.3	34.5
8	Steam	28.6	2.43	237	14.4	34.9
9	Steam	28.2	2.44	262	14.5	35.1

2.3.4. Fluctuation Absorption (steam as fluidizing gas)

For the TCS system based on the $Ca(OH)_2$ to CaO conversion, steam may be used as a fluidizing gas instead of nitrogen. Therefore, the author also evaluated the performance of our fluidized bed reactor model for steam as a fluidizing gas, with the employed parameters listed in Table 2.6. In this case, q_{heat} was chosen to make the reaction time roughly equal to that of Base-1, while the other conditions were identical to those in the case of nitrogen (cf. Tables 2.1–2.3). The obtained results are presented in Figure 2.7 and Table 2.5. For Base-2, the bed temperature linearly increased to 535 °C. Because the partial pressure of steam was higher than that of Base-1, the maximum bed temperature exceeded that observed for the case of nitrogen (cf. Figure 2.6). When q_{heat} suddenly decreased from 2400 to 1355 W at t_{finish}, the bed temperature monotonically decreased to 490 °C in 38 min and then stabilized because of the ongoing hydration. Increased magnitudes of q_{heat} fluctuation (cases 7–9) resulted in higher ΔT_{total}. A slight decrease in t_{finish} and slight increases in $\eta_{chemical}$ and $\eta_{storage}$ were observed with increasing q_{ave} (Table 2.5).

When $q_{fluctuation}$ increased from 0 to 1000 W, ΔT_{total} increased by 114 K in the case of nitrogen and by 18 K in the case of steam. Thus, the fluctuation of bed temperature was much smaller for steam than for nitrogen. This was ascribed to the effects of hydration kinetics. When nitrogen was used, dX/dt equaled 0.0015, 0.0028, and 0.0045 s^{-1} at 435, 440, and 445 °C, respectively (steam partial pressure = 0.01 MPa, X = 0.5, cf. eqs. (2.13) and (2.14)). When steam was used, dX/dt equaled 0.00015, 0.0011, and 0.0037 s^{-1} at 535, 540, and 545 °C, respectively (steam partial pressure = 0.113 MPa, X = 0.5, cf. eqs. (2.13) and (2.14)) [35]. The reaction rate increased 2.9-fold upon going from 435 to 445 °C (nitrogen) and 25-fold upon going from 535 to 545 °C (steam). Thus, when steam was used as the fluidizing gas, dehydration rate had a stronger temperature dependence than when nitrogen was employed. Both the temperature and the reaction rate increased with increasing q_{heat}, so did the heat used

for the endothermic dehydration. If q_{heat} and the heat used for the endothermic dehydration are balanced, the bed temperature stays constant. In the case of steam, if the temperature slightly increases, q_{heat} and the heat for the endothermic dehydration will be balanced. In the case of nitrogen, a higher temperature is needed to balance these quantities. When q_{heat} decreases, the opposite phenomenon occurs. Therefore, the bed temperature did not significantly fluctuate in the case of steam.

Considering base scenarios (Table 2.5), $\eta_{chemical}$ and $\eta_{storage}$ equaled 14.1% and 34.1% in the case of steam (Base-2) and 29.9% and 62.7% in the case of nitrogen (Base-1), respectively. The difference between these values was due to the latent heat of H_2O. For steam and nitrogen, $q_{preheating}$ equaled 1.35 and 0.198 kW_{th}, respectively. Although these values refer to the inlet gas, similar differences were observed for outlet gas. As outlet steam had a higher energy than nitrogen, lower efficiencies were observed in the former case. To increase the efficiency, the latent heat of H_2O should be recovered. In contrast, nitrogen possesses only sensible heat, and the related energy is easy to be used because of the high gas temperature, although the amount of this energy is small.

Table 2.6 Parameters used when steam was employed as a fluidizing gas

Case	t_{change} [s]	$q_{fluctuation}$ [W]	q_{min} [W]
Base-2	0	0	2400
7	60	600	2100
8	60	1000	1900
9	60	1800	1500

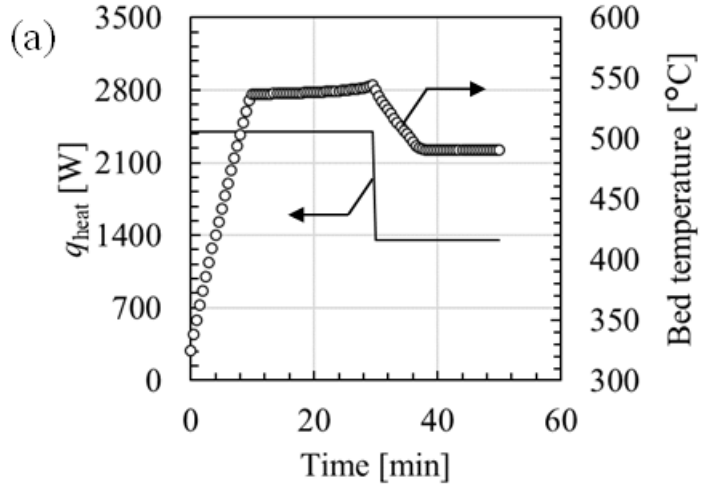
(a)
3500
2800
2100
1400
700
0
q_{heat} [W]
600
550
500
450
400
350
300
Bed temperature [°C]
0
20
40
60
Time [min]

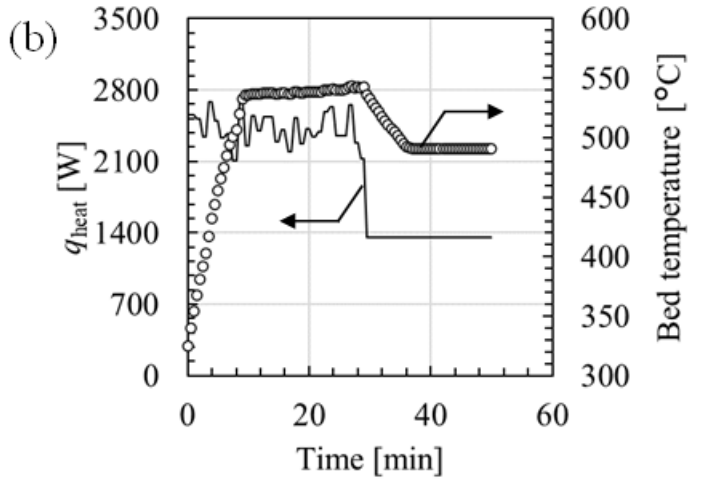
(b)
3500
2800
2100
1400
700
0
q_{heat} [W]
600
550
500
450
400
350
300
Bed temperature [°C]
0
20
40
60
Time [min]

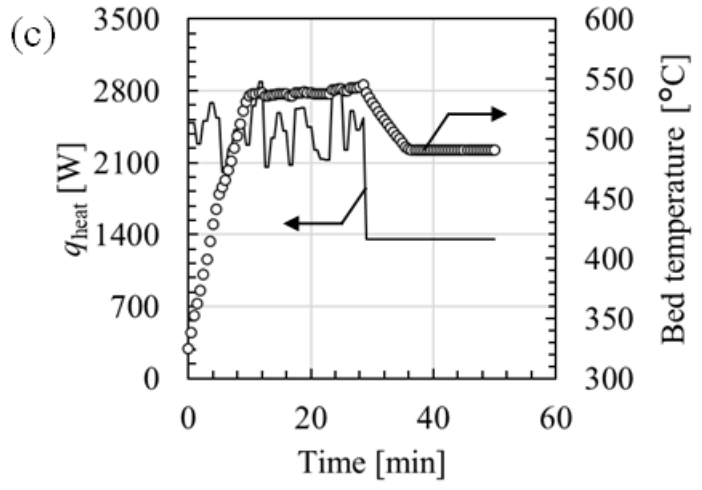
(c)
3500
2800
2100
1400
700
0
q_{heat} [W]
600
550
500
450
400
350
300
Bed temperature [°C]
0
20
40
60
Time [min]

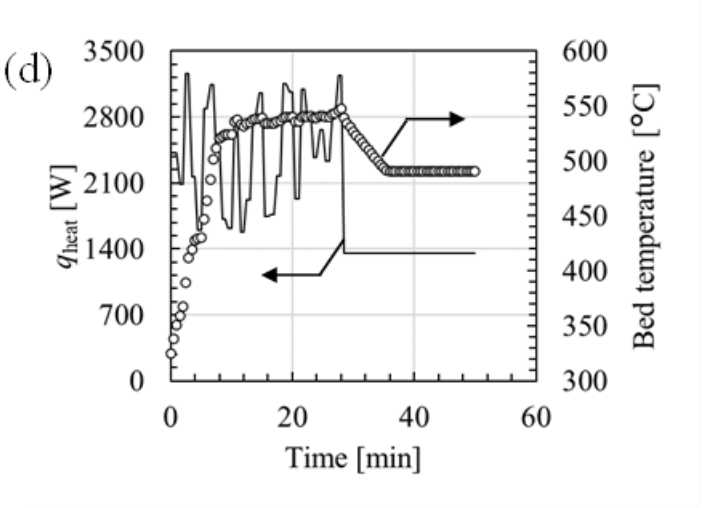

Figure 2.7 Evolution of calculated q_{heat} and fluidized bed temperature with time in the case of steam (a) Base-2, (b) case 7, (c) case 8, and (d) case 9

2.3.5. Sensitivity Analyses

In their steady-state model, Angerer et al. [35] conducted sensitivity analyses for stored heat at various reactor volumes, inlet gas conditions (temperature, pressure, and velocity), *kA* values (heat transfer coefficient and heat transfer area), and heater temperatures. They reported that the heater temperature and the *kA*-value had the largest and second largest effects on stored heat, respectively. Thus, in this study, the author considered q_{heat} to be the most important factor and varied it to perform sensitivity analyses. In these analyses, t_{finish} and the two efficiencies were evaluated, with the results for nitrogen and steam shown in Figures 2.8 and 2.9, respectively. With increasing q_{heat}, the reaction time decreased in both cases, as the heat supply for the endothermic reaction concomitantly increased, whereas $\eta_{storage}$ and $\eta_{chemical}$ increased in both cases. This behavior was ascribed to the decrease in the time required for heating from the initial temperature (325 °C) to the reaction temperature with increasing q_{heat}. During the heating time, hardly any thermochemical heat storage occurred, resulting in lower efficiencies. When q_{heat} increased, so did the differences between $\eta_{storage}$ and $\eta_{chemical}$ because of the concomitant increase in sensible heat due to the increase in bed temperature at t_{finish}. Moreover, the efficiencies observed for steam were close to those observed for nitrogen when q_{heat} was sufficiently large.

The advantages and disadvantages of each fluidizing gas are listed in Table 2.7. During dehydration, nitrogen was a suitable choice considering energy storage efficiencies, and steam was suitable considering the usage of VRE as a heat source. Generally, high steam pressure is preferable during hydration, and low steam pressure is preferable during dehydration. However, if nitrogen is used only during dehydration, it should be stored during hydration or be separated from contaminated air before dehydration. If air is used as a fluidizing gas instead of nitrogen during dehydration to solve these problems, CaO reacts with atmospheric CO_2 to form $CaCO_3$, which makes it difficult to maintain TCS cycles and decreases TCS performance. The

decomposition of $CaCO_3$ requires high temperatures of < 900 °C. This results in lower efficiency and increases equipment cost because of the use of materials capable of withstanding high temperatures. The most important aspect is the entire process. Generally, the TCS system is used in integration with thermal, concentrated solar, and/or other power plants. If the energy of the outlet steam of the TCS reactor can be recovered in these plants to improve energy efficiency, steam is a feasible fluidizing gas. If nitrogen from another process can be supplied to the TCS system, it may be used during dehydration, while steam may be used during hydration. Therefore, the exact setup of the TCS system is determined by considering the integrated processes, each of which should be evaluated.

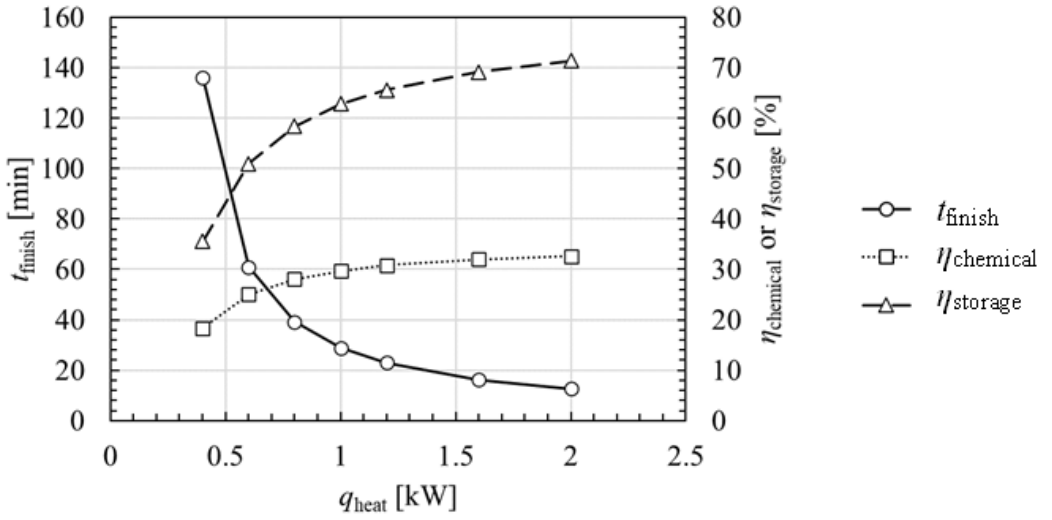

Figure 2.8 Sensitivity analyses for t_{finish} and efficiencies obtained for nitrogen

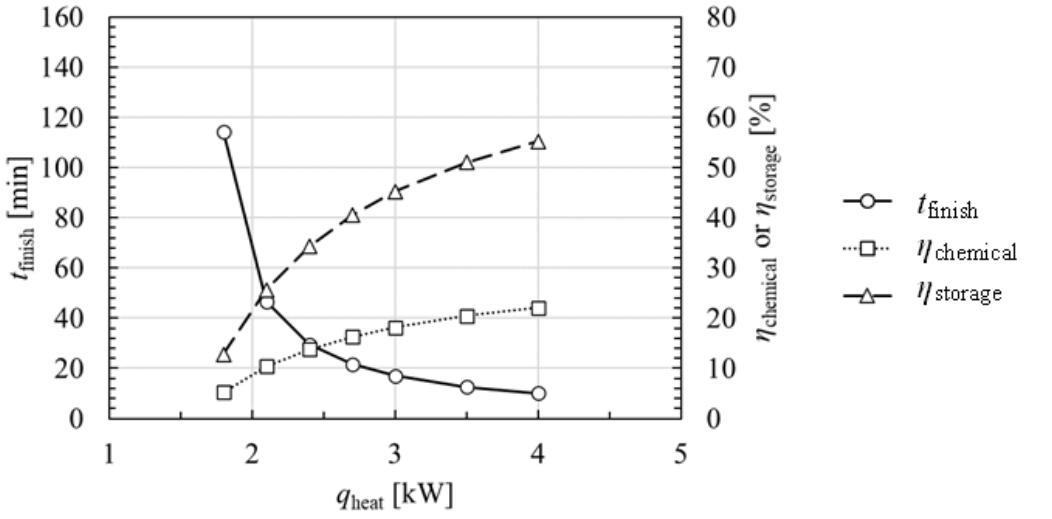

Figure 2.9 Sensitivity analyses for t_{finish} and efficiencies obtained for steam

Table 2.7 Advantages and disadvantages of fluidizing gas pairs

Fluidizing gas dehydration/hydration	Advantages and disadvantages	
	Dehydration	**Hydration**
Nitrogen/nitrogen+steam	✓Fast dehydration ✓High storage efficiency ×Large effects of the VRE fluctuation	×Need a compressor to increase operation pressure
Nitrogen/steam	✓Fast dehydration ✓High storage efficiency ×Large effects of the VRE fluctuation	✓Fast hydration ✓Ease of increasing operation pressure ×Need to store nitrogen or purify air for dehydration
Steam/steam	✓Small effects of the VRE fluctuation ×Low storage efficiency ×High dehydration temperature	✓Fast hydration ✓Ease of increasing operation pressure

✓: Advantages, ×: Disadvantages

2.4. Conclusions of Chapter 2

This chapter proposed a non-steady state fluidized bed model for TCS based on the $Ca(OH)_2$ to CaO conversion and validated this model by comparison with previously reported experimental data. Because VRE was assumed to be used as the TCS heat source, the heat supplied to the TCS system was fluctuating by using a random function, and the absorption of this fluctuation was evaluated for cases of nitrogen or steam as the fluidizing gas. The main results can be summarized as follows.

(1) The simulated data well agreed with the experimental data. However, this agreement was not perfect, as the model was assumed to be ideal, and the rates of mass and heat transfer between phases were fast enough. It was sufficient to evaluate the fluidized bed behavior in a non-steady state.

(2) For nitrogen as the fluidizing gas, the bed temperature fluctuation increased with increasing t_{change} and the magnitude of the fluctuation of supplied heat, with the effects of the latter factor exceeding those of the former. $\eta_{chemical}$ and $\eta_{storage}$ were determined as 29.9% and 62.7%, respectively.

(3) For steam as the fluidizing gas, the bed temperature fluctuation was not significantly influenced by the magnitude of the fluctuation of supplied heat, mainly because the dehydration rate under these conditions had a stronger temperature dependence than in the case of nitrogen. As a result, the bed temperature did not fluctuate. $\eta_{chemical}$ and $\eta_{storage}$ were determined as 14.1% and 34.1%, respectively, i.e., lower than the corresponding values obtained for nitrogen. This was ascribed to the contribution of the latent heat of H_2O in the case of steam. When steam was used as the fluidizing gas, the inlet and outlet gases had a larger energy, resulting in lower energy efficiencies.

(4) Sensitivity analyses were carried out by varying q_{heat}, revealing that with increasing q_{heat}, t_{finish} decreased, while $\eta_{chemical}$ and $\eta_{storage}$ increased, mainly because of the concomitant

decrease in the time required for heating from the initial temperature to the reaction temperature. During this time, hardly any thermochemical heat storage occurred, resulting in lower efficiencies.

Therefore, during dehydration, nitrogen was a suitable choice considering energy storage efficiencies, and steam was a suitable choice considering the usage of VRE as a heat resource. However, the most important aspect is the entire process. The TCS system should be evaluated for all processes, as they influence energy recovery methods. The process evaluations were carried out in following chapters.

Appendix 2.1 (calculation methods for steam as fluidizing gas)

The calculation methods of mass and heat balance in the case of steam as fluidizing gas are explained in Appendix 2.1.

$$\frac{\partial n_{\mathrm{CaO}}}{\partial t} = \frac{n_{\mathrm{Ca}}}{N}\sum_{i=0}^{N}\left(\frac{\mathrm{d}X_i}{\mathrm{d}t}\right) \quad \text{(A.2.1)}$$

$$\frac{\partial n_{\mathrm{Ca(OH)_2}}}{\partial t} = -\frac{n_{\mathrm{Ca}}}{N}\sum_{i=0}^{N}\left(\frac{\mathrm{d}X_i}{\mathrm{d}t}\right) \quad \text{(A.2.2)}$$

$$\frac{\partial n_{\mathrm{Alumina}}}{\partial t} = 0 \quad \text{(A.2.3)}$$

$$A_{\mathrm{B}}\mathrm{d}zv_{\mathrm{g}}\frac{\partial c_{\mathrm{H_2O},i}}{\partial t} = F_{\mathrm{H_2O},i-1,t} - F_{\mathrm{H_2O},i,t} + \frac{n_{\mathrm{Ca}}}{N}\frac{\mathrm{d}X_i}{\mathrm{d}t} \quad \text{(A.2.4)}$$

$$\left\{\sum_{\mathrm{solid}}\left(i\frac{1}{N}c_{\mathrm{p}}\right) + \sum_{\mathrm{gas}}\left(c_{t,i}A_{\mathrm{B}}\mathrm{d}zv_{\mathrm{g}}c_{\mathrm{p}}\right)\right\}\frac{\partial T_{\mathrm{r},i}}{\partial t} = F_{\mathrm{H_2O},i-1,t}c_{\mathrm{p,H_2O},i-1}T_{\mathrm{r},i-1,t} -$$

$$F_{\mathrm{H_2O},i,t}c_{\mathrm{p,H_2O},i}T_{\mathrm{r},i,t} + \frac{n_{\mathrm{Ca}}}{N}\frac{\mathrm{d}X_i}{\mathrm{d}t}\Delta H_{\mathrm{r}} + \frac{q_{\mathrm{reactor}}}{N} \quad \text{(A.2.5)}$$

$$p_{\mathrm{H_2O},i,t+\mathrm{d}t} = p_{\mathrm{r},i} = p_{\mathrm{in}} - \rho_{\mathrm{solid}}g\mathrm{d}zi \quad \text{(A.2.6)}$$

$$p_{\mathrm{H_2O},i,t+\mathrm{d}t} = c_{\mathrm{H_2O},i,t+\mathrm{d}t}RT_{\mathrm{r},i,t+\mathrm{d}t} \quad \text{(A2.7)}$$

$$\left[\sum_{\mathrm{solid}}\left(n_{\mathrm{solid}}c_{\mathrm{p}}\right) + \sum_{i=1}^{N}\left\{\sum_{\mathrm{gas}}\left(c_{t,i}A_{\mathrm{B}}\mathrm{d}zv_{\mathrm{g}}c_{\mathrm{p}}\right)\right\}\right]\left(T_{\mathrm{r},t+\mathrm{d}t} - T_{\mathrm{r},t}\right) = \sum_{i=1}^{N}\left[\left\{\sum_{\mathrm{solid}}\left(\frac{n_{\mathrm{solid}}}{N}c_{\mathrm{p}}\right) +\right.\right.$$

$$\left.\left.\sum_{\mathrm{gas}}\left(c_{i,t}A_{\mathrm{B}}\mathrm{d}zv_{\mathrm{g}}c_{\mathrm{p}}\right)\right\}\left(T_{\mathrm{r},i,t+\mathrm{d}t} - T_{\mathrm{r},i,t}\right)\right] \quad \text{(A.2.8)}$$

These equations were solved. There are eight variables; $n_{\mathrm{CaO},t+\mathrm{d}t}$, $n_{\mathrm{Ca(OH)2},t+\mathrm{d}t}$, $n_{\mathrm{Alumina},t+\mathrm{d}t}$, $c_{\mathrm{H2O},i,t+\mathrm{d}t}$, $T_{\mathrm{r},i,t+\mathrm{d}t}$, $F_{\mathrm{H2O},i,t}$, $p_{\mathrm{H2O},i,t+\mathrm{d}t}$, $T_{\mathrm{r},t+\mathrm{d}t}$. $p_{\mathrm{H2O},i,t+\mathrm{d}t}$ are constants (eq. (A.2.6)). Eqs. (A.2.1)–(A.2.3) are general differential equations, respectively. Eqs. (A.2.4)–(A.2.8) are simultaneous equations.

To simplify the equations, following variables were used.

$$\alpha = \frac{A_{\mathrm{B}}\mathrm{d}zv_{\mathrm{g}}}{\mathrm{d}t}$$

$$\beta = \frac{\sum_{\mathrm{solid}}\left(nc_{\mathrm{p}}\frac{1}{N}\right) + \sum_{\mathrm{gas}}\left(c_{t,i}A_{\mathrm{B}}\mathrm{d}zv_{\mathrm{g}}c_{\mathrm{p}}\right)}{\mathrm{d}t}$$

$$\gamma = F_{\mathrm{H2O},i-1,t}c_{\mathrm{p,H2O},i-1}T_{r,i-1,t} + \frac{n_{\mathrm{Ca}}}{N}\frac{\mathrm{d}X_i}{\mathrm{d}t}\Delta H_{\mathrm{r}} + \frac{q_{\mathrm{reactor}}}{N}$$

By eqs. (A.2.6) and (A.2.7),

$$T_{\mathrm{r},t+\mathrm{d}t} = \frac{p_{\mathrm{H2O},i,t+\mathrm{d}t}}{c_{\mathrm{H2O},i,t+\mathrm{d}t}R} \qquad \text{(A.2.9)}$$

By eqs. (A.2.9) and (A.2.5),

$$\beta\left(T_{\mathrm{r},i,t+\mathrm{d}t} - T_{\mathrm{r},i,t}\right) = \gamma - F_{\mathrm{H2O},i,t}c_{\mathrm{p,H2O},i}T_{\mathrm{r},i,t}$$

$$\beta\frac{p_{\mathrm{H2O},i,t+\mathrm{d}t}}{c_{\mathrm{H2O},i,t+\mathrm{d}t}R} - \beta T_{\mathrm{r},t} = \gamma - F_{\mathrm{H2O},i,t}c_{\mathrm{p,H2O},i}T_{\mathrm{r},i,t}$$

$$c_{\mathrm{H2O},i,t+\mathrm{d}t} = \frac{\beta p_{\mathrm{H2O},i,t+\mathrm{d}t}}{R\left(\gamma - F_{\mathrm{H2O},i,t}c_{\mathrm{p,H2O},i}T_{\mathrm{r},i,t} + \beta T_{\mathrm{r},i,t}\right)} \qquad \text{(A.2.10)}$$

By eqs. (A.2.4) and (A.2.10),

$$\alpha c_{\mathrm{H2O},i,t+\mathrm{d}t} - \alpha c_{\mathrm{H2O},i,t} = F_{\mathrm{H2O},i-1,t} - F_{\mathrm{H2O},i,t} + n_{\mathrm{r}}\frac{\mathrm{d}X_i}{\mathrm{d}t}\frac{1}{N}$$

$$\frac{\alpha\beta p_{\mathrm{H2O},i,t+\mathrm{d}t}}{R\left(\gamma - F_{\mathrm{H2O},i,t}c_{\mathrm{p,H2O},i}T_{\mathrm{r},i,t} + \beta T_{\mathrm{r},t}\right)} = F_{\mathrm{H2O},i-1,t} - F_{\mathrm{H2O},i,t} + n_{\mathrm{r}}\frac{\mathrm{d}X_i}{\mathrm{d}t}\frac{1}{N} + \alpha c_{\mathrm{H2O},i,t}$$

$$\begin{aligned}\frac{\alpha\beta p_{\mathrm{H2O},i,t+\mathrm{d}t}}{R} &= \left(F_{\mathrm{H2O},i-1,t} + n_{\mathrm{r}}\frac{\mathrm{d}X_i}{\mathrm{d}t}\frac{1}{N} + \alpha c_{\mathrm{H2O},i,t}\right)\left(\gamma + \beta T_{\mathrm{r},i,t} - c_{\mathrm{p,H2O},i}T_{\mathrm{r},i,t}F_{\mathrm{H2O},i,t}\right)\\ &\quad - F_{\mathrm{H2O},i,t}\left(\gamma + \beta T_{\mathrm{r},i,t} - c_{\mathrm{p,H2O},i}T_{\mathrm{r},i,t}F_{\mathrm{H2O},i,t}\right)\end{aligned}$$

$$\begin{aligned}\frac{\alpha\beta p_{\mathrm{H2O},i,t+\mathrm{d}t}}{R} &= \left(F_{\mathrm{H2O},i-1,t} + n_{\mathrm{r}}\frac{\mathrm{d}X_i}{\mathrm{d}t}\frac{1}{N} + \alpha c_{\mathrm{H2O},i,t}\right)\left(\gamma + \beta T_{\mathrm{r},i,t}\right)\\ &\quad + \left(F_{\mathrm{H2O},i-1,t} + n_{\mathrm{r}}\frac{\mathrm{d}X_i}{\mathrm{d}t}\frac{1}{N} + \alpha c_{\mathrm{H2O},i,t}\right)\left(-c_{\mathrm{p,H2O},i}T_{\mathrm{r},i,t}\right)F_{\mathrm{H2O},i,t}\\ &\quad - \left(\gamma + \beta T_{\mathrm{r},i,t}\right)F_{\mathrm{H2O},i,t} + \left(c_{\mathrm{p,H2O},i}T_{\mathrm{r},i,t}\right){F_{\mathrm{H2O},i,t}}^2\end{aligned}$$

$$\begin{aligned}&\left(c_{\mathrm{p,H2O},i}T_{\mathrm{r},i,t}\right){F_{\mathrm{H2O},i,t}}^2\\ &\quad + \left\{\left(F_{\mathrm{H2O},i-1,t} + n_{\mathrm{r}}\frac{\mathrm{d}X_i}{\mathrm{d}t}\frac{1}{N} + \alpha c_{\mathrm{H2O},i,t}\right)\left(-c_{\mathrm{p,H2O},i}T_{\mathrm{r},i,t}\right)\right.\\ &\quad \left. - \left(\gamma + \beta T_{\mathrm{r},i,t}\right)\right\}F_{\mathrm{H2O},i,t} + \left(F_{\mathrm{H2O},i-1,t} + n_{\mathrm{r}}\frac{\mathrm{d}X_i}{\mathrm{d}t}\frac{1}{N} + \alpha c_{\mathrm{H2O},i,t}\right)\left(\gamma + \beta T_{\mathrm{r},i,t}\right)\\ &\quad - \frac{\alpha\beta p_{\mathrm{H2O},i,t+\mathrm{d}t}}{R} = 0\end{aligned}$$

$$A{F_{\mathrm{H2O},i,t}}^2 + BF_{\mathrm{H2O},i,t} + C = 0$$

$$F_{\mathrm{H2O},i,t} = \frac{-B - \sqrt{B^2 - 4AC}}{2A}$$

The variables were calculated by using eqs. (A.2.10), (A.2.9), (A.2.8) in turn.

Appendix 2.2 (calculation methods for nitrogen as fluidizing gas)

The calculation methods of mass and heat balance in the case of nitrogen as fluidizing gas are explained in Appendix 2.2.

$$\frac{\partial n_{\mathrm{CaO}}}{\partial t} = \frac{n_{\mathrm{Ca}}}{N}\sum_{i=0}^{N}\left(\frac{\mathrm{d}X_i}{\mathrm{d}t}\right) \quad \text{(A.2.11)}$$

$$\frac{\partial n_{\mathrm{Ca(OH)_2}}}{\partial t} = -\frac{n_{\mathrm{Ca}}}{N}\sum_{i=0}^{N}\left(\frac{\mathrm{d}X_i}{\mathrm{d}t}\right) \quad \text{(A.2.12)}$$

$$\frac{\partial n_{\mathrm{Alumina}}}{\partial t} = 0 \quad \text{(A.2.13)}$$

$$A_{\mathrm{B}}\mathrm{d}z v_{\mathrm{g}}\frac{\partial c_{\mathrm{H_2O},i}}{\partial t} = F_{\mathrm{H_2O},i-1,t} - F_{\mathrm{H_2O},i,t} + \frac{n_{\mathrm{Ca}}}{N}\frac{\mathrm{d}X_i}{\mathrm{d}t} \quad \text{(A.2.14)}$$

$$A_{\mathrm{B}}\mathrm{d}z v_{\mathrm{g}}\frac{\partial c_{\mathrm{N_2},i}}{\partial t} = F_{\mathrm{N_2},i-1,t} - F_{\mathrm{N_2},i,t} \quad \text{(A.2.15)}$$

$$\left\{\sum_{\mathrm{solid}}\left(i\frac{1}{N}c_{\mathrm{p}}\right) + \sum_{\mathrm{gas}}\left(c_{i,t}A_{\mathrm{B}}\mathrm{d}z v_{\mathrm{g}}c_{\mathrm{p}}\right)\right\}\frac{\partial T_{\mathrm{r},i}}{\partial t} = F_{\mathrm{H_2O},i-1,t}c_{\mathrm{p,H_2O},i-1}T_{\mathrm{r},i-1,t} -$$

$$F_{\mathrm{H_2O},i,t}c_{\mathrm{p,H_2O},i}T_{\mathrm{r},i,t} + F_{\mathrm{N_2},i-1,t}c_{\mathrm{p,N_2},i-1}T_{\mathrm{r},i-1,t} - F_{\mathrm{N_2},i,t}c_{\mathrm{p,N_2},i}T_{\mathrm{r},i,t} + \frac{n_{\mathrm{Ca}}}{N}\frac{\mathrm{d}X_i}{\mathrm{d}t}\Delta H_{\mathrm{r}} + \frac{q_{\mathrm{reactor}}}{N}$$

(A.2.16)

$$p_{\mathrm{r},i,t+\mathrm{d}t} = p_{\mathrm{in}} - \rho_{\mathrm{solid}}g\mathrm{d}zi \quad \text{(A.2.17)}$$

$$p_{\mathrm{r},i,t+\mathrm{d}t} = p_{\mathrm{H_2O},i,t+\mathrm{d}t} + p_{\mathrm{N_2},i,t+\mathrm{d}t} \quad \text{(A.2.18)}$$

$$p_{\mathrm{H_2O},i,t+\mathrm{d}t} = c_{\mathrm{H_2O},i,t+\mathrm{d}t}RT_{\mathrm{r},i,t+\mathrm{d}t} \quad \text{(A.2.19)}$$

$$p_{\mathrm{N_2},i,t+\mathrm{d}t} = c_{\mathrm{N_2},i,t+\mathrm{d}t}RT_{\mathrm{r},i,t+\mathrm{d}t} \quad \text{(A.2.20)}$$

$$c_{\mathrm{H_2O},i,t} = \frac{F_{\mathrm{H_2O},i,t}}{F_{\mathrm{N_2},i,t}}c_{\mathrm{N_2},i,t} \quad \text{(A.2.21)}$$

$$\left[\sum_{\mathrm{solid}}\left(n_{\mathrm{solid}}c_{\mathrm{p}}\right) + \sum_{i=1}^{N}\left\{\sum_{\mathrm{gas}}\left(c_{t,i}A_{\mathrm{B}}\mathrm{d}z v_{\mathrm{g}}c_{\mathrm{p}}\right)\right\}\right]\left(T_{\mathrm{r},i,t+\mathrm{d}t} - T_{\mathrm{r},i,t}\right) =$$

$$\sum_{i=1}^{N}\left[\left\{\sum_{\mathrm{solid}}\left(\frac{n_{\mathrm{solid}}}{N}c_{\mathrm{p}}\right) + \sum_{\mathrm{gas}}\left(c_{i,t}A_{\mathrm{B}}\mathrm{d}z v_{\mathrm{g}}c_{\mathrm{p}}\right)\right\}\left(T_{\mathrm{r},i,t+\mathrm{d}t} - T_{\mathrm{r},i,t}\right)\right] \quad \text{(A.2.22)}$$

These equations were solved. There are twelve variables; $n_{\mathrm{CaO},t+dt}$, $n_{\mathrm{Ca(OH)2},t+dt}$, $n_{\mathrm{Alumina},t+dt}$, $c_{\mathrm{H2O},i,t+dt}$, $c_{\mathrm{N2},i,t+dt}$, $T_{\mathrm{r},i,t+dt}$, $F_{\mathrm{H2O},i,t}$, $F_{\mathrm{N2},i,t}$, $p_{\mathrm{H2O},i,t+dt}$, $p_{\mathrm{N2},i,t+dt}$, $p_{\mathrm{r},i,t+dt}$, $T_{\mathrm{r},t+dt}$. $p_{\mathrm{r},i,t+\mathrm{d}t}$ are constants (eq. (A.2.17)). Eqs. (A.2.11)–(A.2.13) are general differential equations, respectively. Eqs. (A.2.14)–(A.2.22) are simultaneous equations.

To simplify the equations, following variables were used.

$$\alpha = \frac{A_{\mathrm{B}} \mathrm{d}z v_{\mathrm{g}}}{\mathrm{d}t}$$

$$\beta = \frac{\sum_{\mathrm{solid}}(n c_{\mathrm{p}}) + \sum_{\mathrm{gas}}(c A_{\mathrm{B}} \mathrm{d}z v_{\mathrm{g}} c_{\mathrm{p}})}{\mathrm{d}t}$$

$$\gamma = F_{\mathrm{H2O},i-1,t} c_{\mathrm{p,H2O},i-1} T_{\mathrm{r},i-1,t} + F_{\mathrm{N2},i-1,t} c_{\mathrm{p,N2},i-1} T_{\mathrm{r},i-1,t} + n_{\mathrm{r}} \frac{\mathrm{d}X_i}{\mathrm{d}t} \frac{\mathrm{d}z}{H_{\mathrm{B}}} \Delta H_{\mathrm{r}} + \frac{q_{\mathrm{reactor}}}{N}$$

By eq. (A.2.21),

$$F_{\mathrm{H2O},i,t} = \frac{c_{\mathrm{H2O},i,t}}{c_{\mathrm{N2},i,t}} F_{\mathrm{N2},i,t} \qquad \text{(A.2.23)}$$

By eqs. (A.2.17), (A.2.18), (A.2.19),

$$p_{\mathrm{r},i,t+\mathrm{d}t} = \left(c_{\mathrm{H2O},i,t+\mathrm{d}t} + c_{\mathrm{N2},i,t+\mathrm{d}t}\right) R T_{\mathrm{r},i,t+\mathrm{d}t}$$

$$T_{\mathrm{r},i,t+\mathrm{d}t} = \frac{p_{\mathrm{r},i,t+\mathrm{d}t}}{\left(c_{\mathrm{H2O},i,t+\mathrm{d}t} + c_{\mathrm{N2},i,t+\mathrm{d}t}\right) R} \qquad \text{(A.2.24)}$$

By eqs. (A.2.6), (A.2.23), (A.2.24),

$$\beta\left(T_{\mathrm{r},i,t+\mathrm{d}t} - T_{\mathrm{r},i,t}\right) = \gamma - F_{\mathrm{H2O},i,t} c_{\mathrm{p,H2O},i} T_{\mathrm{r},i,t} - F_{\mathrm{N2},i,t} c_{\mathrm{p,N2},i} T_{\mathrm{r},i,t}$$

$$\beta \frac{p_{\mathrm{r},i,t+\mathrm{d}t}}{\left(c_{\mathrm{H2O},i,t+\mathrm{d}t} + c_{\mathrm{N2},i,t+\mathrm{d}t}\right) R} = \gamma + \beta T_{\mathrm{r},i,t} - \left(\frac{c_{\mathrm{H2O},i,t}}{c_{\mathrm{N2},i,t}} c_{\mathrm{p,H2O},i} T_{\mathrm{r},i,t} + c_{\mathrm{p,N2},i} T_{\mathrm{r},i,t}\right) F_{\mathrm{N2},i,t} \qquad \text{(A.2.25)}$$

By eqs. (A.2.14), (A.2.15), (A.2.23),

$$\alpha c_{\mathrm{H2O},i,t+\mathrm{d}t} - \alpha c_{\mathrm{H2O},i,t} = F_{\mathrm{H2O},i-1,t} - \frac{c_{\mathrm{H2O},i,t}}{c_{\mathrm{N2},i,t}} F_{\mathrm{N2},i,t} + n_{\mathrm{r}} \frac{\mathrm{d}X_i}{\mathrm{d}t} \frac{\mathrm{d}z}{H_{\mathrm{B}}}$$

$$\alpha c_{\mathrm{N2},i,t+\mathrm{d}t} - \alpha c_{\mathrm{N2},i,t} = F_{\mathrm{N2},i-1,t} - F_{\mathrm{N2},i,t}$$

These two equations were added.

$$\alpha\left(c_{\mathrm{H2O},i,t+\mathrm{d}t}+c_{\mathrm{N2},i,t+\mathrm{d}t}\right)=\alpha\left(c_{\mathrm{H2O},i,t}+c_{\mathrm{N2},i,t}\right)+F_{\mathrm{H2O},i-1,t}+n_{\mathrm{r}}\frac{\mathrm{d}X_i}{\mathrm{d}t}\frac{\mathrm{d}z}{H_{\mathrm{B}}}+F_{\mathrm{N2},i-1,t}-\left(\frac{c_{\mathrm{H2O},i,t}}{c_{\mathrm{N2},i,t}}+1\right)F_{\mathrm{N2},i,t} \quad \text{(A.2.26)}$$

By eqs. (A.2.25), (A.2.26),

$$\beta\frac{p_{\mathrm{r},i,t+\mathrm{d}t}}{R}\frac{\alpha}{\alpha\left(c_{\mathrm{H2O},i,t}+c_{\mathrm{N2},i,t}\right)+F_{\mathrm{H2O},i-1,t}+n_{\mathrm{r}}\frac{\mathrm{d}X_i}{\mathrm{d}t}\frac{\mathrm{d}z}{H_{\mathrm{B}}}+F_{\mathrm{N2},i-1,t}-\left(\frac{c_{\mathrm{H2O},i,t}}{c_{\mathrm{N2},i,t}}+1\right)F_{\mathrm{N2},i,t}}$$

$$=\gamma+\beta T_{\mathrm{r},i,t}-\left(\frac{c_{\mathrm{H2O},i,t}}{c_{\mathrm{N2},i,t}}c_{\mathrm{p,H2O},i}T_{\mathrm{r},i,t}+c_{\mathrm{p,N2},i}T_{\mathrm{r},i,t}\right)F_{\mathrm{N2},i,t}$$

$$\frac{\alpha\beta p_{\mathrm{r},i,t+\mathrm{d}t}}{R}=\left\{\gamma+\beta T_{\mathrm{r},i,t}-\left(\frac{c_{\mathrm{H2O},i,t}}{c_{\mathrm{N2},i,t}}c_{\mathrm{p,H2O},i}T_{\mathrm{r},i,t}+c_{\mathrm{p,N2},i}T_{\mathrm{r},i,t}\right)F_{\mathrm{N2},i,t}\right\}\left\{\alpha\left(c_{\mathrm{H2O},i,t}+c_{\mathrm{N2},i,t}\right)+F_{\mathrm{H2O},i-1,t}+n_{\mathrm{r}}\frac{\mathrm{d}X_i}{\mathrm{d}t}\frac{\mathrm{d}z}{H_{\mathrm{B}}}+F_{\mathrm{N2},i-1,t}-\left(\frac{c_{\mathrm{H2O},i,t}}{c_{\mathrm{N2},i,t}}+1\right)F_{\mathrm{N2},i,t}\right\}$$

$$\frac{\alpha\beta p_{\mathrm{r},i,t+\mathrm{d}t}}{R}=\left(\gamma+\beta T_{\mathrm{r},i,t}\right)\left\{\alpha\left(c_{\mathrm{H2O},i,t}+c_{\mathrm{N2},i,t}\right)+F_{\mathrm{H2O},i-1,t}+n_{\mathrm{r}}\frac{\mathrm{d}X_i}{\mathrm{d}t}\frac{\mathrm{d}z}{H_{\mathrm{B}}}+F_{\mathrm{N2},i-1,t}-\left(\frac{c_{\mathrm{H2O},i,t}}{c_{\mathrm{N2},i,t}}+1\right)F_{\mathrm{N2},i,t}\right\}$$

$$-\left(\frac{c_{\mathrm{H2O},i,t}}{c_{\mathrm{N2},i,t}}c_{\mathrm{p,H2O},i}T_{\mathrm{r},i,t}+c_{\mathrm{p,N2},i}T_{\mathrm{r},i,t}\right)F_{\mathrm{N2},i,t}\left\{\alpha\left(c_{\mathrm{H2O},i,t}+c_{\mathrm{N2},i,t}\right)+F_{\mathrm{H2O},i-1,t}+n_{\mathrm{r}}\frac{\mathrm{d}X_i}{\mathrm{d}t}\frac{\mathrm{d}z}{H_{\mathrm{B}}}+F_{\mathrm{N2},i-1,t}-\left(\frac{c_{\mathrm{H2O},i,t}}{c_{\mathrm{N2},i,t}}+1\right)F_{\mathrm{N2},i,t}\right\}$$

$$\frac{\alpha\beta p_{\mathrm{r},i,t+\mathrm{d}t}}{R}=\left(\gamma+\beta T_{\mathrm{r},i,t}\right)\left\{\alpha\left(c_{\mathrm{H2O},i,t}+c_{\mathrm{N2},i,t}\right)+F_{\mathrm{H2O},i-1,t}+n_{\mathrm{r}}\frac{\mathrm{d}X_i}{\mathrm{d}t}\frac{\mathrm{d}z}{H_{\mathrm{B}}}+F_{\mathrm{N2},i-1,t}\right\}$$

$$-\left(\gamma+\beta T_{\mathrm{r},i,t}\right)\left(\frac{c_{\mathrm{H2O},i,t}}{c_{\mathrm{N2},i,t}}+1\right)F_{\mathrm{N2},i,t}$$

$$-\left(\frac{c_{\mathrm{H2O},i,t}}{c_{\mathrm{N2},i,t}}c_{\mathrm{p,H2O},i}T_{\mathrm{r},i,t}+c_{\mathrm{p,N2},i}T_{\mathrm{r},i,t}\right)F_{\mathrm{N2},i,t}\left\{\alpha\left(c_{\mathrm{H2O},i,t}+c_{\mathrm{N2},i,t}\right)+F_{\mathrm{H2O},i-1,t}+n_{\mathrm{r}}\frac{\mathrm{d}X_i}{\mathrm{d}t}\frac{\mathrm{d}z}{H_{\mathrm{B}}}+F_{\mathrm{N2},i-1,t}\right\}$$

$$+\left(\frac{c_{\mathrm{H2O},i,t}}{c_{\mathrm{N2},i,t}}c_{\mathrm{p,H2O},i}T_{\mathrm{r},i,t}+c_{\mathrm{p,N2},i}T_{\mathrm{r},i,t}\right)\left(\frac{c_{\mathrm{H2O},i,t}}{c_{\mathrm{N2},i,t}}+1\right)F_{\mathrm{N2},i,t}{}^2$$

$$\left(\frac{c_{\mathrm{H2O},i,t}}{c_{\mathrm{N2},i,t}}c_{\mathrm{p,H2O},i}T_{\mathrm{r},i,t}+c_{\mathrm{p,N2},i}T_{\mathrm{r},i,t}\right)\left(\frac{c_{\mathrm{H2O},i,t}}{c_{\mathrm{N2},i,t}}+1\right){F_{\mathrm{N2},i,t}}^{2}$$
$$-\left[\left(\gamma+\beta T_{\mathrm{r},i,t}\right)\left(\frac{c_{\mathrm{H2O},i,t}}{c_{\mathrm{N2},i,t}}+1\right)\right.$$
$$+\left(\frac{c_{\mathrm{H2O},i,t}}{c_{\mathrm{N2},i,t}}c_{\mathrm{p,H2O},i}T_{\mathrm{r},i,t}+c_{\mathrm{p,N2},i}T_{\mathrm{r},i,t}\right)\left\{\alpha\left(c_{\mathrm{H2O},i,t}+c_{\mathrm{N2},i,t}\right)+F_{\mathrm{H2O},i-1,t}\right.$$
$$\left.\left.+n_{\mathrm{r}}\frac{\mathrm{d}X_i}{\mathrm{d}t}\frac{\mathrm{d}z}{H_{\mathrm{B}}}+F_{\mathrm{N2},i-1,t}\right\}\right]F_{\mathrm{N2},i,t}$$
$$+\left(\gamma+\beta T_{\mathrm{r},i,t}\right)\left\{\alpha\left(c_{\mathrm{H2O},i,t}+c_{\mathrm{N2},i,t}\right)+F_{\mathrm{H2O},i-1,t}+n_{\mathrm{r}}\frac{\mathrm{d}X_i}{\mathrm{d}t}\frac{\mathrm{d}z}{H_{\mathrm{B}}}+F_{\mathrm{N2},i-1,t}\right\}$$
$$-\frac{\alpha\beta p_{\mathrm{r},i,t+\mathrm{d}t}}{R}=0$$

$$A{F_{\mathrm{N2},i,t}}^{2}+BF_{\mathrm{N2},i,t}+C=0$$

$$F_{\mathrm{N2},i,t}=\frac{-B-\sqrt{B^2-4AC}}{2A}$$

The variables were calculated by using eqs. (A.2.23), (A.2.14), (A.2.15), (A.2.24), (A.2.19), (A.2.20), (A.2.22) in turn.

Chapter 3

Design of the TCS System Integrated with a Biomass Power Plant and Evaluation of the Power Generation Flexibility

3.1. Abstract

In this chapter, the TCS system (a fluidized bed reactor using $CaO/Ca(OH)_2$ particles) integrated with a biomass power plant was proposed. In the strategy of power generation in this chapter, ORC was worked by the heat from biomass combustion in normal operation. In charging time, the electricity from the power grid was stored by the dehydration reaction in the daytime although the turbine output was not changed, and the amount of biomass combustion decreased accordingly compared to normal operation time. In discharging time, the heat from the hydration reaction was converted to electricity through the ORC in the evening, and the turbine output increased to respond to the increase of the electricity demand. The designed process was evaluated from energy efficiencies and the flexibility of the power generation by dynamic simulation. Results show that energy storage efficiency and round-trip efficiency equaled 58.5% and 9.79% (only ORC: 11.4%) for base case (the fluidized bed volume = 10 m^3, the scale of ORC = 1 MW_e), respectively. The energy storage efficiency increased by increasing the heat recovery from steam out of the fluidized bed reactor, and it led to the decrease of the biomass fuel consumption in charging time. It was found that the inlet gas flow rate into the reactor had the largest influence on energy efficiencies among the parameters such as fluidized bed volume, inlet gas conditions into the reactor, and heat supply into the reactor. In addition, the increase of the turbine output and discharging time were flexibly changed in discharging time by changing operational parameters. Therefore, it is possible to add flexibility to biomass power plants by integrating the TCS system using a fluidized bed reactor.

3.2. Process Design of the TCS System Integrated with a Biomass Power Plant

3.2.1. Advantages of the TCS System Integrated with a Biomass Power Plant

The advantages and disadvantages of a biomass power plant and the TCS system are summarized in Table 3.1. Biomass is one of the renewable energies, and a biomass power plant is usually utilized as base load power. However, the power output is much lower than a thermal power plant, and there is the difficulty of biomass collection because CO_2 emission increase as the transportation distance is longer [155]. In addition, biomass growth rate is much slower than the rate of utilization (combustion). On the other hand, the energy sources of the TCS system are heat generated from solar and wind power (other heat sources such as biomass combustion, geothermal heat, and exhaust heat from other plants can also be used), and they are abundant. The disadvantage is that dynamic operation (i.e., intermittent charging, discharging, and stop times) is required. The dynamic operation leads to low round-trip efficiency. Thus, integrating the TCS system with a biomass power plant compensate for each disadvantage. A biomass power plant can use the solar and wind power as the heat source by integrating the TCS system, leading to increasing the maximum power output or decreasing the biomass fuel usage for the combustion in a boiler. The operation of the integrated plant is more stable than the operation of only a TCS system. In addition, there are advantages that initial cost decrease and the TCS system add the flexibility of power generation to the biomass power plant [156].

Table 3.1 The advantages and disadvantages of a biomass power plant and the TCS system

	Biomass power plant	TCS system
Advantages	➢ Renewable energy ➢ Operated as base load power (power output is stable)	➢ Abundant energy source (solar, wind, and exhaust heat) ➢ Storage of VRE ➢ Flexible power generation
Disadvantages	➢ Low power output ➢ Difficulty of biomass collection [155] ➢ Biomass growth rate is much slower than the reaction rate of combustion	➢ Dynamic operation (charging, discharging, and stop times are intermittent)

3.2.2. Water Management

In the previous studies, it was reported that high energy efficiency was achieved by using a steam turbine after the TCS reactor because the enthalpy of outlet steam from the reactor was recovered efficiently [132,133] (the details were described in section 1.3.3). However, using a turbine after the TCS reactor has a serious problem that there is a possibility of contamination in the turbine if the turbine inlet steam is the same as the reactant gas. Thus, the author separated the TCS cycle and the biomass power plant cycle based on heat integration concepts. Note, in this study, the author considers energy loss of steam (see stream 5 in Figure 3.1) returning to the water tank after HX1 in the TCS cycle as waste heat although this hot water or low-temperature steam can be used as heat (not for power generation).

3.2.3. Whole Process of the TCS System Integrated with a Biomass Power Plant

Figure 3.1 shows a schematic image of the whole process. In the TCS cycle, water (stream 1) is compressed by a pump (P1). The compressed water (stream 2) is heated by an electrical heater (H1) whose heat source is electricity from renewable energy. The generated steam (stream 3) is used as fluidizing and reactant gas for a fluidized bed reactor (see section 2.2.1). The energy of outlet steam (stream 4) is recovered by a heat exchanger (HX1), which is a preheater of heat medium R245fa. In ORC, the R245fa (stream 6) is compressed by a pump (P2). The R245fa (stream 7) is preheated by HX1 during charging and discharging times and then heated by a heater (H2). In normal operation time, the R245fa after P2 (stream 7') is directly supplied to H2. The heat source of H2 is biomass. The biomass is combusted in a boiler, and the heat is transferred by thermal oil. The R245fa vapor (stream 9) flow in turbines (T2), and the R245fa (stream 10) is, then, cooled by a condenser (C2). In this study, the biomass combustion process (containing thermal oil) was not included, and only the heat duty of H2 was evaluated.

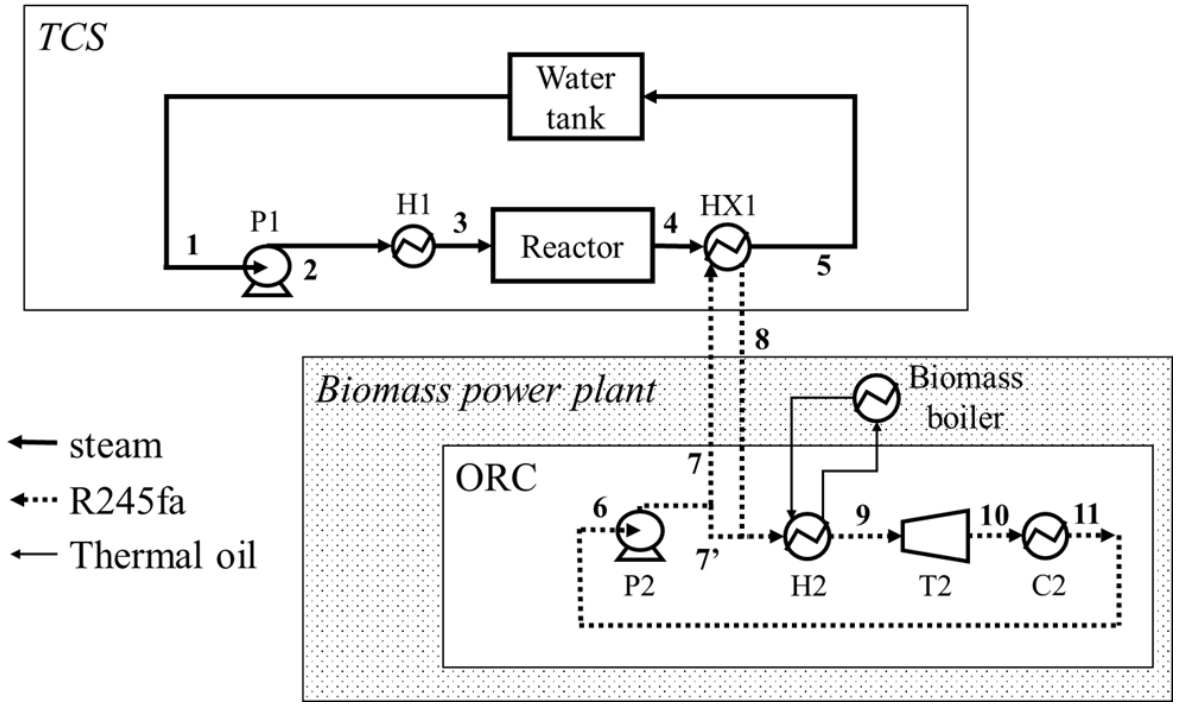

Figure 3.1 The schematic image of the TCS system integrated with a biomass power plant

3.2.4. Power Generation Strategy

Charging and discharging times were divided absolutely because it was assumed that only one reactor was used. Because there is surplus power at daytime due to the increase of solar power generation and high demand in the evening, the author assumed that charging time was daytime and discharging time was evening.

Figure 3.2 shows the image of the power generation strategy. In normal operation (except for charging and discharging times), only the biomass power plant is working, and the output is 1 MW_e. In charging time, the power generation keeps constant, and the heat from HX1 reduces the heat duty of H2 (or biomass combustion). In discharging time, the heat duty of H2 returns to the same values for normal operation. Thus, the output of the turbine increases by the amount of heat duty of HX1. In this study, it was assumed that the energy needed in this TCS system was supplied by surplus power completely, and heat loss from the reactor was negligible. This means that the final temperature of dehydration is the initial temperature of hydration, and the final temperature of hydration is the initial temperature of dehydration. In this study, it was assumed that the final temperature of dehydration was 560 °C, and the final temperature of hydration was 450 °C.

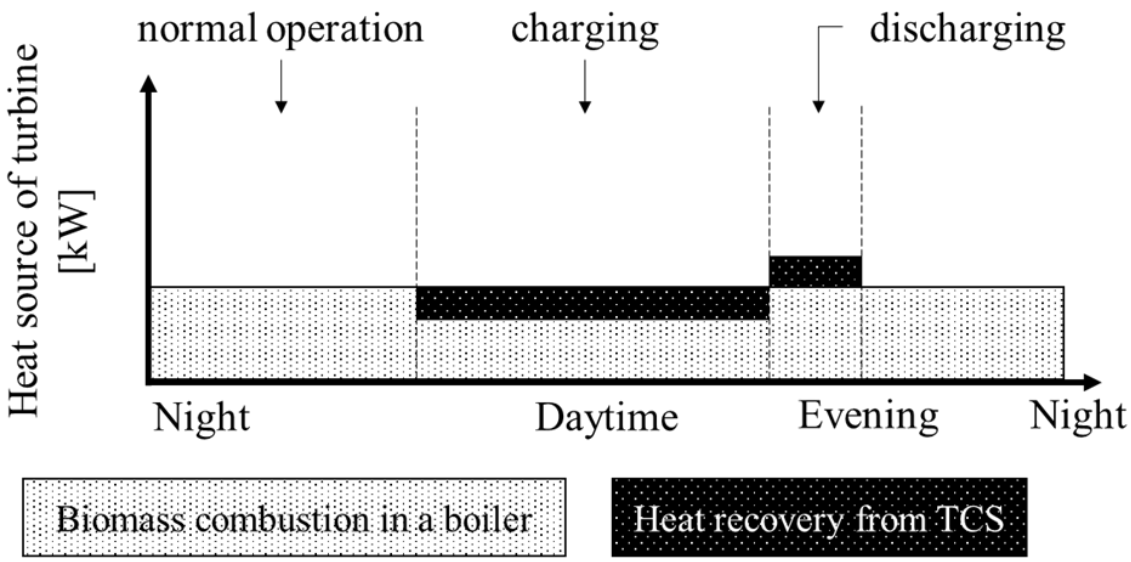

Figure 3.2 The image of the power generation strategy

3.2.5. Calculation Parameters

In this chapter, the capacity of the biomass power plant was assumed to be 1 MW_e-scale. Generally, ORC is used for such small scale plants [134], and R245fa is used for working material (see section 1.3.3). A biomass power plant using ORC of R245fa was investigated [157]. Thus, their temperature and pressure conditions [157] were used in this study although the flow rate was determined so that turbine output was 1 MW_e in normal operation.

The parameters for the base case are summarized in Tables 3.2–3.6. In normal operation and charging time, ORC conditions were the same. On the other hand, in discharging time, turbine output increased because of the increase of heat from HX1. Thus, R245fa flow rate increased so that turbine inlet temperature became 105 °C in discharging time. Table 3.5 shows the coefficient of overall heat transfer between H_2O and R245fa. These values were calculated with fouling factor is 0.0005 m^2·K/W, and the thin of pipes which is stainless is 0.62 mm [158,159].

Table 3.2 The parameters of ORC conditions for normal operation

Parameters	Stream number	Unit	Value
Working fluid [157]	6–11	–	R245fa
Mass flow rate of working fluid	9	kg/s	37.93
Turbine inlet pressure (P2) [157]	9	MPa	1.14
Turbine outlet pressure [157]	10	MPa	0.24
Turbine inlet temperature (H2) [157]	9	°C	96.7
Condenser outlet temperature [157]	11	°C	34.0
Turbine gross output (T2)	–	MW_e	1.00
Isentropic efficiency (T2)	–	%	90

Table 3.3 The parameters of a fluidized bed reactor

Parameters	Unit	Value
Fluidized bed volume	m^3	10
Fluidized bed height [29]	m	0.37
Alumina content [29]	wt%	70
Bed expansion [35]	%	125
Pressure loss of gas distributor [35]	Pa	2.0×10^4
Pressure loss of a filter [35]	Pa	1.0×10^4

Table 3.4 The parameters of process simulation

Parameters	Unit	Charging (Dehydration)	Discharging (Hydration)
Gas pressure at reactor inlet (P1)	MPa	0.15	0.15
Gas temperature at reactor inlet (H1)	°C	600	200
Gas velocity at reactor inlet [29]	m/s	0.087	0.087
Initial bed temperature	°C	450	560
Final bed temperature	°C	560	450
Heat into the reactor, $q_{reactor}$	MW_{th}	0.7	0

Table 3.5 The overall heat transfer coefficient between H_2O and R245fa [158,159]

Hot stream (H_2O)	Cold stream (R245fa)	U [$W/m^2/K$]
Liquid	Liquid	573.5
Liquid	Boiling	827.3
Liquid	Gas	101.2
Condensing	Liquid	626.4
Condensing	Boiling	942.0
Condensing	Gas	102.8
Gas	Liquid	101.6
Gas	Boiling	107.5
Gas	Gas	55.63

Table 3.6 The physical data

Parameters	**Unit**	**$Ca(OH)_2$**	**CaO**	**Alumina**	**H_2O**
True density of particles [29]	kg/m^3	2240	3300	3970	–
Bulk density of particles in the fixed bed [29]	kg/m^3	490	650	736	–
Molecular weight [154]	g/mol	74	56	102	18
Standard enthalpy of formation [154]	kJ/mol	−986.09	−635.09	–	–241.83
Particle size [29]	μm	3.8	3.8	171.7	–

3.2.6. Process Evaluation Methods

The process was evaluated using energy storage efficiency, η_{storage} [%], TCS system efficiency, η_{TCS} [%], and round-trip efficiency, η_{energy} [%] that were defined in eqs. (3.6)–(3.8) and calculated by the following equations.

$$Q_{\text{storage}} = Q_{\text{chemical}} + Q_{\text{sensible}} - \Delta Q_{\text{H2}} \quad (3.1)$$

$$-\Delta Q_{\text{H2}} = q_{\text{H2,n}} t_{\text{c}} - Q_{\text{H2,c}} \left(= Q_{\text{HX1,c}}\right) \quad (3.2)$$

$$H_{\text{in,TCS}} = Q_{\text{P1}} + Q_{\text{H1}} + Q_{\text{reactor}} \quad (3.3)$$

$$H_{\text{out}} = W_{\text{T2}} \quad (3.4)$$

$$H_{\text{in}} = Q_{\text{P1}} + Q_{\text{H1}} + Q_{\text{reactor}} + Q_{\text{P2}} + Q_{\text{H2}} \quad (3.5)$$

$$\eta_{\text{storage}}\ [\%] = \frac{Q_{\text{storage}}}{H_{\text{in,TCS,c}}} \times 100 \quad (3.6)$$

$$\eta_{\text{TCS}}\ [\%] = \frac{Q_{\text{HX1,c}} + Q_{\text{HX1,d}}}{H_{\text{in,TCS,c}} + H_{\text{in,TCS,d}}} \times 100 \quad (3.7)$$

$$\eta_{\text{energy}}\ [\%] = \frac{H_{\text{out,c}} + H_{\text{out,d}}}{H_{\text{in,c}} + H_{\text{in,d}}} \times 100 \quad (3.8)$$

where Q_{storage} is the stored energy [J], Q_{chemical} is the stored energy as reaction heat (i.e., the heat of the endothermic reaction) [J], Q_{sensible} is the stored energy as sensible heat of the solid from 450 to 560 °C [J], ΔQ_{H2} is the decrease of the heat duty in H2 (i.e., the saving of the biomass usage) [J], q is heat [W], Q is heat [J], Q_{HX1} is the heat duty in HX1 [J] (cf. Figure 3.1), $H_{\text{in,TCS}}$ is the input energy into the TCS system (P1, H1, and reactor) [J], Q_{reactor} is the heat supply into the reactor by electrical heaters, H_{out} is the turbine output enthalpy [J], W is work [J], and H_{in} is the input energy into the whole process (P1, H1, reactor, P2, and H2) [J]. Subscripts "n" represents normal operation time, "c" represents charging time, and "d" represents discharging time. These energy values [J] were calculated from the integration of each energy value [W] from 0 min to t_{c} (charging time [min]) or t_{d} (discharging time [min]). Note unit of ΔQ_{H2} can be represented by [%] to compare the performance even if the different charging time. The performance in charging time was evaluated by η_{storage}, which means the ratio of stored energy

and input energy into the TCS system. Biomass saving in charging time was considered as stored energy. The performance of the TCS system (contain charging and discharging time) was evaluated by η_{TCS}, which means the ratio of HX1 duty (during charging and discharging time) and inlet energy into the TCS system. The performance of the whole process was evaluated by η_{energy}. In addition, w is work [W], and A_{HX1} is the heat exchange area of HX1 [m^2]. For the base case (section 3.3.2), A_{HX1} was determined so that ΔQ_{H2} is −20%.

3.3. Results and Discussion

3.3.1. Calculation of the outlet steam flow rates and temperature of the Fluidized Bed Reactor

Figures 3.3 and 3.4 shows the calculated results of the outlet steam flow rates and temperatures of the fluidized bed reactor in charging and discharging time, respectively. The process calculation was carried out at 101 plots from 0 to 67 min (charging time) or 48 min (discharging time), and process conditions for each time were assumed to be steady state. In charging time, bed temperature increased from 450 °C to reaction temperature by heating the reactor at 700 kW_{th}. After 12 min, bed temperature became constant because dehydration reaction proceeds. Dehydration reaction led to the increase of outlet steam flow rate from 0.88 up to 0.99 kg/s. The bed temperature increased slightly during dehydration reaction and increased up to 560 °C dramatically after the reaction finished. The outlet steam flow rate also decreased after that. In discharging time (Figure 3.4), bed temperature decreased from 560 °C to reaction temperature. From 5 min, bed temperature became a constant value because hydration reaction proceeds. Hydration reaction led to the decrease of outlet steam flow rate from 1.61 to 1.45 kg/s. After the reaction, bed temperature decreased to 450 °C, and outlet steam flow rate returned to the initial value. Although the inlet gas velocity was the same between charging and discharging times, inlet steam flow rate (which was the same for outlet steam flow rate at 0 min) was different because the inlet gas temperature was different.

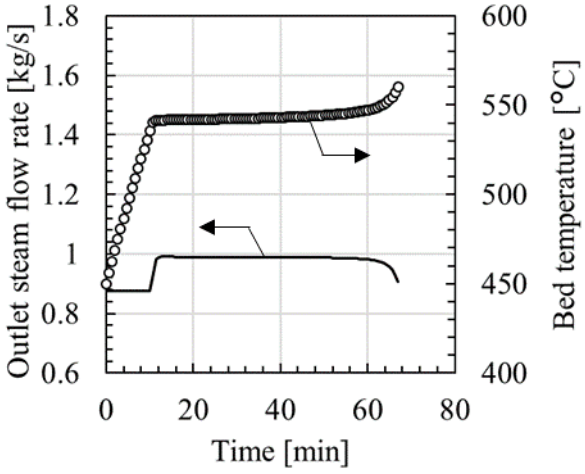

Figure 3.3 The calculated results of the fluidized bed reactor in charging time

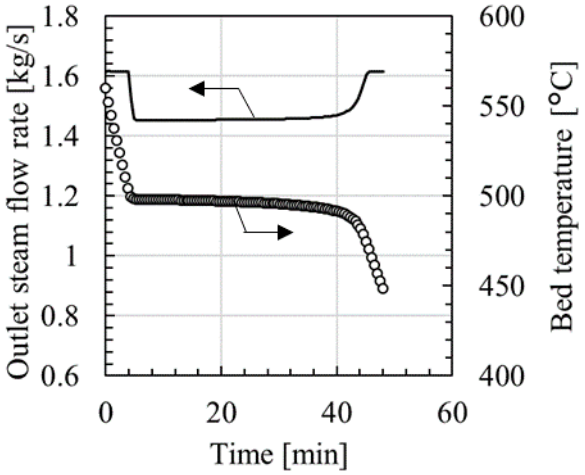

Figure 3.4 The calculated results of the fluidized bed reactor in discharging time

3.3.2. Process Evaluation for Base Case

Tables 3.7–3.9 show the calculated results for the base case. η_{energy} was 9.79% although η_{energy} was 11.4% in normal operation. In previous study, it was reported that storage efficiency was < 87% [46] although $\eta_{storage}$ was 58.5% in this study. The reason is the waste heat of the steam after HX1. Thus, the author proposed an improved process in section 3.3.6 to increase efficiency. The process stream data and main results of devices are presented in Appendix 3.1.

Table 3.7 The calculated results in normal operation (working only ORC)

Parameters	Unit	Value	Note
w_{P2}	kW_e	36.8	Input
q_{H2}	MW_{th}	8.76	Input
w_{T2}	MW_e	1.00	Output
q_{C2}	MW_{th}	7.80	Waste
η_{energy}	%	11.4	

Table 3.8 The calculated results in charging time

Parameters	Unit	Value	Note
t_c	min	67	
W_{P1}	MJ	0.21	Input (TCS)
W_{P2}	GJ	0.146	Input (ORC)
Q_{H1}	GJ	13.0	Input (TCS)
Q_{H2}	GJ	28.1	Input (ORC)
$Q_{reactor}$	GJ	2.81	Input (TCS)
$Q_{chemical}$	GJ	2.05	Storage
$Q_{sensible}$	MJ	124	Storage
$-\Delta Q_{H2}$ (or Q_{HX1})	GJ	7.07	Storage
$Q_{storage}$	GJ	9.24	Storage
W_{T2}	GJ	4.02	Output
The waste steam energy after HX1	GJ	6.78	Waste (TCS)
Q_{C2}	GJ	31.3	Waste (ORC)
$\eta_{storage}$	%	58.5	
A_{HX1}	m^2	67	

Table 3.9 The calculated results in discharging time

Parameters	Unit	Value	Note
t_d	min	48	
W_{P1}	MJ	0.234	Input (TCS)
W_{P2}	GJ	0.140	Input (ORC)
Q_{H1}	GJ	13.4	Input (TCS)
Q_{H2}	GJ	25.2	Input (ORC)
Q_{HX1}	GJ	10.7	
W_{T2}	GJ	4.09	Output
The waste steam energy after HX1	GJ	4.17	Waste (TCS)
Q_{C2}	GJ	32.0	Waste (ORC)
η_{TCS} (contain charging time)	%	61.0	
η_{energy} (contain charging time)	%	9.79	
A_{HX1}	m^2	67	

3.3.3. Relation among Bed Volume, HX1 Heat Exchange Area, and H2 Load Reduction (in charging time)

The author investigated the relation among bed volume, A_{HX1}, and ΔQ_{H2}. Bed volume was changed to 7, 10, and 13 m^3, and the set value of ΔQ_{H2} was changed to −10, −20, and −30%. A_{HX1} was determined to meet each condition. Table 3.10 shows the calculated results of required heat exchange area, ΔQ_{H2} and $\eta_{storage}$ in HX1. Note that for case 7 m^3 and −30%, ΔQ_{H2} did not achieve −30% because temperature differences between hot and cold streams are smaller than 10 °C. In addition, Figure 3.5 shows a *T*-*Q* diagram of HX1 for all cases. For −10% and 13 m^3, A_{HX1} became the lowest value (30 m^2). In the case of 13 m^3, flow rate of steam was higher than that for 7 and 10 m^3, and it led to the slow decrease of steam temperature (cf. Figure 3.5). Thus, there are large temperature differences between hot and cold streams, leading to the lowest A_{HX1}. However, for 7 m^3, A_{HX1} was the second smallest (35 m^2). The reason is that steam was condensed in HX1 (outlet vapor fraction was 0.858 at $t_c/2$). The overall heat transfer coefficient was high value by steam condensing (see Table 3.5). For −20 and −30%, A_{HX1} was larger with the increase of bed volume. The reason is that the effects of condensing were larger than the effects of the temperature differences. $H_{storage}$ was larger with the increase of ΔQ_{H2} or the decrease of bed volume. When bed volume decreases, flow rate also decreases. Thus, the recovery of the steam energy became sufficient when ΔQ_{H2} was constant. Note the remaining amount of heat is supplied by the heat exchanger, H2 (i.e. heat from the biomass boiler).

Table 3.10 The heat exchange area of HX1 with changing bed volume and H2 load reduction

Bed volume	t_c	H2 load change, ΔQ_{H2}		
[m³]	[min]	−10%	−20%	−30%
7	50	35 m² (ΔQ_{H2}: −10.1%) ($\eta_{storage}$: 47.1%)	63 m² (ΔQ_{H2}: −20.0%) ($\eta_{storage}$: 76.5%)	104 m² (ΔQ_{H2}: −27.7%) ($\eta_{storage}$: 99.3%)
10	67	39 m² (ΔQ_{H2}: −10.0%) ($\eta_{storage}$: 36.1%)	67 m² (ΔQ_{H2}: −20.1%) ($\eta_{storage}$: 58.5%)	105 m² (ΔQ_{H2}: −30.2%) ($\eta_{storage}$: 80.9%)
13	83	30 m² (ΔQ_{H2}: −10.1%) ($\eta_{storage}$: 29.6%)	71 m² (ΔQ_{H2}: −20.1%) ($\eta_{storage}$: 47.6%)	107 m² (ΔQ_{H2}: −30.1%) ($\eta_{storage}$: 65.4%)

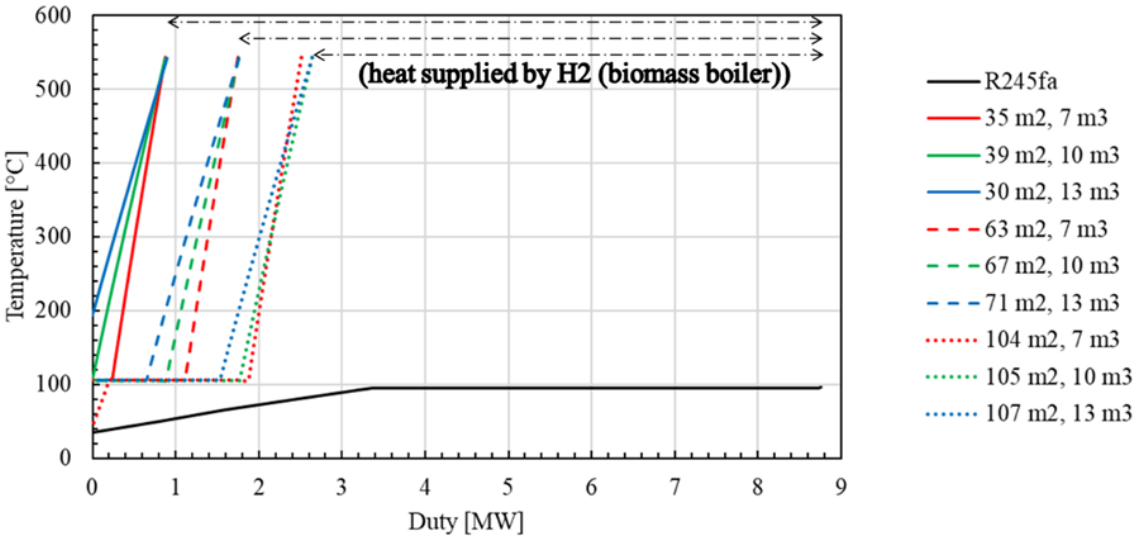

Figure 3.5 *T-Q* diagram of HX1 for all cases at $t_c/2$

3.3.4. Effects of Bed Volume, Inlet Gas Conditions, Heat into the Reactor on Energy Efficiencies

The effects of bed volume, inlet gas conditions (flow rate, pressure, and temperature), and $q_{reactor}$ on energy efficiencies were investigated with fixed A_{HX1} (67 m^2). Tables 3.11 and 3.12 shows the parameters of all cases for calculation in charging and discharging time, respectively. In charging time, low pressure is preferable for fast dehydration reaction. However, because of pressure loss in a fluidized bed, it is necessary to pressurize steam at the bed inlet. Thus, inlet gas pressure during charging time was set to the constant value (0.15 MPa). The results are summarized in Table 3.13. t_c or t_d was short when dehydration or hydration reaction was promoted, respectively. ΔQ_{H2} decreased by increasing inlet steam flow rate in charging time. When inlet steam temperature increased, inlet steam flow rate decreased to keep the same gas velocity, resulting in the increase of ΔQ_{H2}. For C-F1.5 and C-F2, ΔQ_{H2} was almost the same values because the effects of steam condensing for C-F1.5 (vapor fraction at outlet of HX1 was 0.912 at half of t_c) was possibly the same for the effects of larger temperature differences for C-F2. The $\eta_{storage}$ was strongly influenced by ΔQ_{H2} owing to the amount of the waste heat recovery. It was found that heat supply into the reactor was almost no effect on $\eta_{storage}$ although the reaction time is shorter by increasing it. In discharging time, the similar effects of inlet steam flow rate and temperature were observed on the efficiencies. When inlet steam pressure increased, inlet steam flow rate increased to keep constant gas velocity, resulting in the decrease of energy efficiencies. Therefore, it was found that the designed process performances were strongly influenced by the inlet steam flow rate.

Table 3.11 The parameters of all cases in charging time

Case name	Changed parameter	Bed volume [m^3]	Inlet gas flow rate [m/s]	Inlet gas temperature [°C]	$q_{reactor}$ [kW_{th}]
C-base		10	0.087	600	700
C-V7, 10, 13	Bed volume	7, 10, 13	0.087	600	700
C-F1, 1.5, 2	Inlet gas flow rate	10	0.087, 0.129, 0.172	600	700
C-T500, 550, 600	Inlet temperature	10	0.087	500, 550, 600	700
C-q600, 700, 800	Heat supply to reactor	10	0.087	600	600, 700, 800

Table 3.12 The parameters of all cases in discharging time

Case name	Changed parameter	Bed volume [m^3]	Inlet gas flow rate [m/s]	Inlet gas temperature [°C]	Inlet gas pressure [MPa]
D-base		10	0.087	200	0.15
D-V7, 10, 13	Bed volume	7, 10, 13	0.087	200	0.15
D-F1, 1.5, 2	Inlet gas flow rate	10	0.087, 0.129, 0.172	200	0.15
D-T500, 550, 600	Inlet temperature	10	0.087	200, 300, 350	0.15
D-P1.5, 2.0, 2.5	Heat supply to reactor	10	0.087	200	0.15, 0.2, 0.25

Table 3.13 The results of process evaluation for each case

Case	t_c [min]	t_d [min]	ΔQ_{H2} [%]	$\eta_{storage}$ [%]	η_{TCS} [%]	η_{energy} [%]
Only ORC	–	–	–	–	–	11.4
Base case	67	48	−20.1	58.5	61.0	9.79
V7	50	48	−21.2	80.0	84.1	10.8
Base (V10)	67*	48*	−20.1*	58.5*	61.0*	9.79*
V13	83	48	−18.8	45.2	47.3	8.92
Base (C-F1)	67*	–	−20.1*	58.5*	–	–
C-F1.5	62	–	−17.9	38.9	–	–
C-F2	57	–	−17.9	30.8	–	–
C-T500	95	–	−19.7	50.9	–	–
C-T550	78	–	−19.9	54.8	–	–
Base (C-T600)	67*	–	−20.1*	58.5*	–	–
C-q600	76	–	−20.1	58.5	–	–
Base (C-q700)	67*	–	−20.1*	58.5*	–	–
C-q800	60	–	−20.0	58.5	–	–
Base (D-F1)	67*	48*	−20.1*	58.5*	61.0*	9.79*
D-F1.5	67*	32	−20.1*	58.5*	51.8	9.21
D-F2	67*	25	−20.1*	58.5*	47.2	8.85
Base (D-P150)	67*	48*	−20.1*	58.5*	61.0*	9.79*
D-P200	67*	35	−20.1*	58.5*	57.1	9.50
D-P250	67*	27	−20.1*	58.5*	54.2	9.28
Base (D-T200)	67*	48*	−20.1*	58.5*	61.0*	9.79*
D-T300	67*	85	−20.1*	58.5*	69.0	10.2
D-T350	67*	121	−20.1*	58.5*	74.1	10.4

*The same values as the base case

#The results of discharging in the row of the charging cases were filled by "–".

3.3.5. Flexibility of the Power Generation (in discharging time)

The author investigated the flexibility of the power generation in discharging time. Figure 3.6 shows the results by changing the volume or inlet steam conditions. Turbine output was 1000 kW_e at 0 min and increased dramatically up to maximum value. Then, turbine output decreased in two steps (the slowly decrease at first, and then the faster decrease). After the decrease, turbine output became constant because hydration reaction occurred. After the hydration reaction, turbine output slightly increased and then decreased. The discharging time was finished as the bed temperature reached 450 °C. The faster decrease before hydration reaction and the slight increase after hydration reaction were caused by flow rate changes from reaction. When the hydration reaction occurred, the outlet steam flow rate from the reactor decreased. It leads to a decrease of the heat duty in HX1. Thus, turbine output changed rapidly in the time during slight change of turbine output before and after hydration reaction. When the bed volume increased (see Figure 3.6 (a)), turbine output increased because the outlet steam flow rate increased although the discharging time was no change. When inlet gas flow rate increased (see Figure 3.6 (b)) or inlet gas pressure increased (see Figure 3.6 (c)), turbine output increased. However, the discharging time became short. When inlet gas flow rate increased, a larger amount of heat from hydration reaction was used to increase the inlet gas temperature up to reactor temperature, and hydration reaction was promoted to keep the bed temperature. When inlet gas pressure increased, hydration reaction was promoted because steam reacted. Thus, the discharging time became short with the increase of flow rate or pressure. When inlet gas temperature increased (see Figure 3.6 (d)), turbine output decreased slightly and discharging time became longer. The reason is that the hydration reaction became slower because inlet gas has larger energy to keep reaction temperature. Note that there is actually delay time because of discrete steady state calculations. Above all, it was found that flexible power generation can be achieved with any parameter changes.

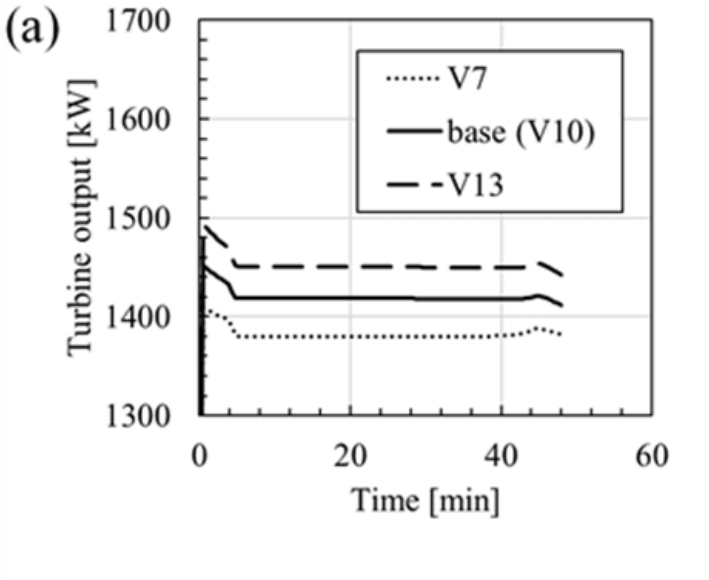
(a)
1700
1600
1500
1400
1300
Turbine output [kW]
V7
base (V10)
V13
0
20
40
60
Time [min]

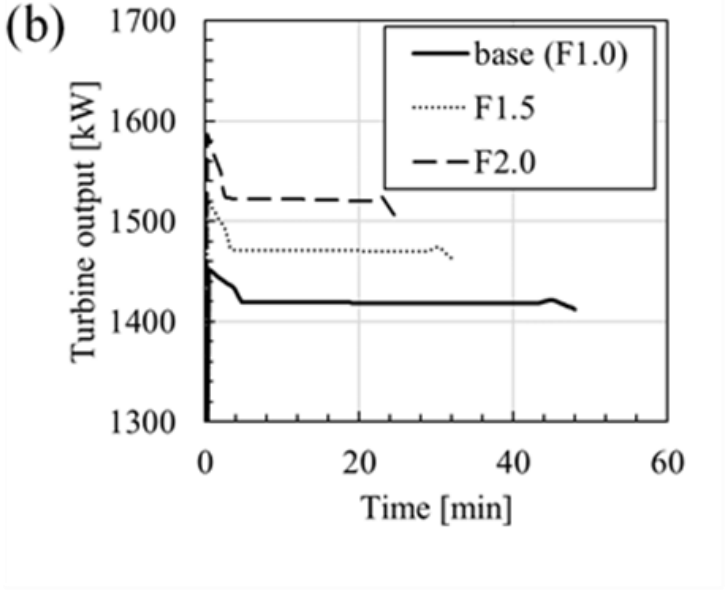
(b)
1700
1600
1500
1400
1300
Turbine output [kW]
base (F1.0)
F1.5
F2.0
0
20
40
60
Time [min]

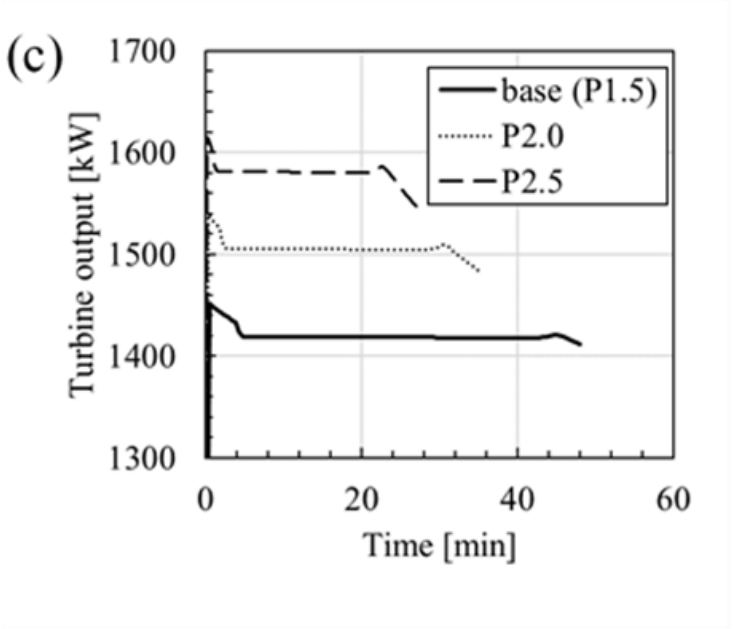

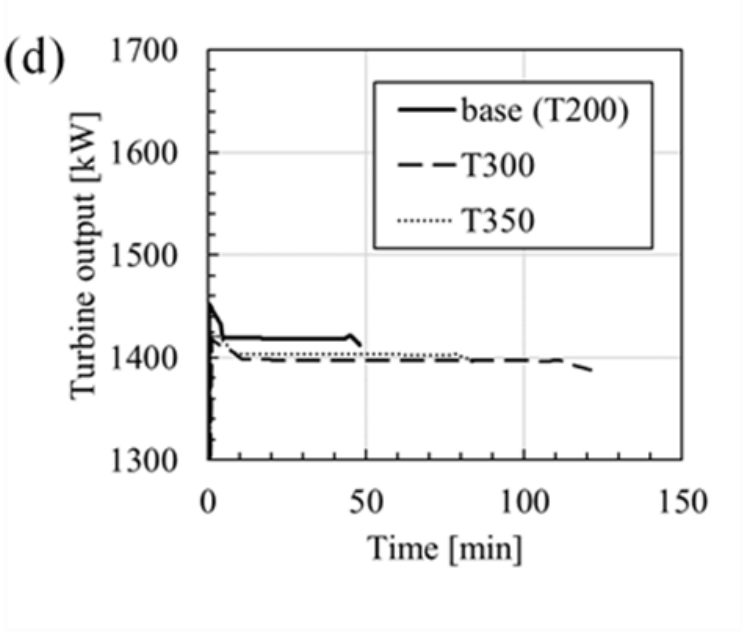

Figure 3.6 The turbine output changes in discharging time by changing (a) bed volume, (b) inlet gas flow rate, (c) inlet gas pressure, and (d) inlet gas temperature

3.3.6. Improved Process

To utilize the steam energy after HX1, the author proposed the improved process. Figure 3.7 shows the image of the improved process. In this process, steam and water after HX1 (stream 5) is separated. Steam (stream 13) is, then, compressed by blower (B1) and recycled (mixed with the water after P1). In charging time, steam flow increased by dehydration reaction. Thus, part of steam after HX1 returns to the water tank although inlet steam becomes recycled steam. The η_{storage} was re-defined by following equation:

$$\eta_{\text{storage}} = \frac{Q_{\text{storage}} + Q_{\text{recycled}}}{H_{\text{in,TCS,c}} + W_{\text{B1}}} \times 100\% \qquad (3.10)$$

where Q_{recycled} is the enthalpy of recycled stream 13 (see Figure 3.7). Table 3.14 shows the results of the energy efficiencies of the improved process (C-F2-improved). From Table 3.14, η_{storage} was dramatically improved from 30.8% to 92.1% by recycling steam after HX1. This clearly indicates that the recycling of the steam after HX1 is very effective. Note the enthalpy of steam is not necessary to be recovered after HX1 because the energy source of the TCS system is renewable.

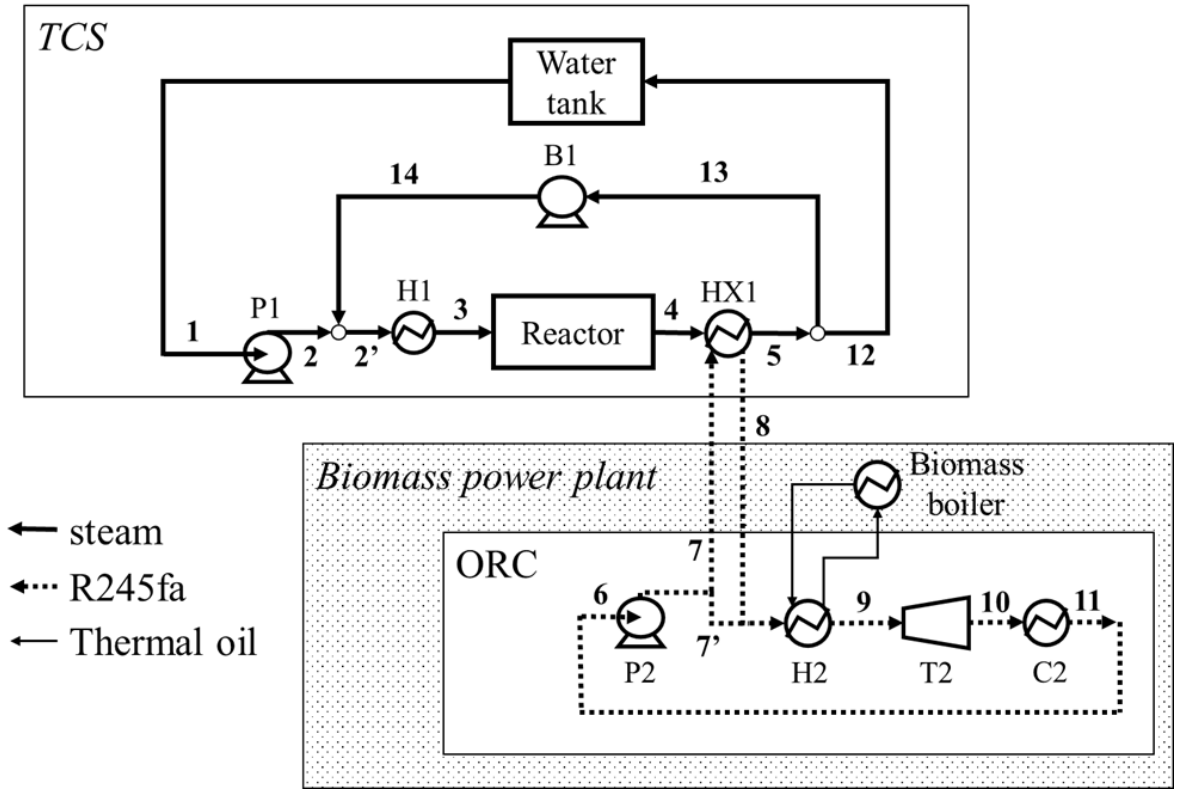

Figure 3.7 The image of the improved process

Table 3.14 The results of the energy efficiency of the improved process

Case	$\eta_{storage}$ [%]
C-F2	30.8
C-F2-improved	92.1

3.4. Conclusions of Chapter 3

This chapter proposed the design of the TCS system using $CaO/Ca(OH)_2$ integrated with a biomass power plant. In charging time, electricity from the power grid was stored in the TCS system, and heat generation by biomass combustion decreased to keep constant turbine output because of the heat recovery from steam after the TCS reactor. In discharging time, the heat from hydration reaction was converted to electricity through the ORC, and the turbine output increased. The designed process was evaluated by energy storage efficiency, TCS system efficiency, and round-trip efficiency. In addition, the flexibility of the power generation was also evaluated by dynamic simulation. The main results were summarized as follows.

(1) For the base case (fluidized bed reactor volume is 10 m^3, heat exchange area of HX1 is 67 m^2, and H2 load reduction is 20%), energy storage efficiency, TCS system efficiency, and round-trip efficiency were 58.5%, 61.0%, and 9.79%, respectively.

(2) The relation of the bed volume, heat exchange area of HX1, and H2 load reduction was investigated. For −10%, the case of 13 m^3 was the lowest heat exchange area of HX1 because of high temperature differences between hot and cold streams. The case of 7 m^3 was the second lowest heat exchange area of HX1 because of steam condensing in HX1. For −20% and −30%, the heat exchange area of HX1 decreased by increasing bed volume because steam condensing had a larger effect than temperature differences between hot and cold streams.

(3) The effects of some parameters on the process performance were investigated. It was found that the steam flow rate has the strongest effect on energy efficiencies because the amount of heat recovery by HX1 was strongly influenced by flow rate.

(4) Turbine output increased with the increase of bed volume, inlet steam flow rate, and inlet steam pressure and the decrease of inlet steam temperature. The discharging time increased with the increase of inlet steam temperature and the decrease of the inlet steam flow rate

and inlet steam pressure. Thus, it was found that flexible power generation is possible.

(5) The improved process was proposed. The steam from HX1 was recycled to inlet by using a blower in the improved process. As a result, energy storage efficiency was increased from 30.8% to 92.1% for the case of C-F2.

Therefore, the TCS system integrated with a biomass power plant was feasible technology. Although the energy storage efficiencies and the round-trip efficiency for base case were lower than the previous study, higher energy efficiencies can be achieved by utilizing waste energy, which is contained in hot water or low temperature steam, as heat (not for power generation).

Appendix 3.1 (process data for the base case)

Table A.3.1 The process stream data in normal operation

Stream number or variables	Material	Temperature [°C]	Pressure [MPa]	Flow rate [kg/s]	Result of device
6	R245fa	34.0	0.24	37.93	–
7, 8	R245fa	34.5	1.14	37.93	–
9	R245fa	96.6	1.14	37.93	–
10	R245fa	55.8	0.24	37.93	–
11	R245fa	34.0	0.24	37.93	–
w_{P2}	–	–	–	–	36.8 kW_e
q_{H2}	–	–	–	–	8.76 MW_{th}
w_{T2}	–	–	–	–	1.00 MW_e
q_{C2}	–	–	–	–	7.80 MW_{th}

Table A.3.2 The process stream data and main results of devices at 33.5 min (t_c/2) in charging time

Stream number or variables	Material	Temperature [°C]	Pressure [MPa]	Flow rate [kg/s]	Result of device
1	Steam	25.0	0.100	0.875	–
2	Steam	25.0	0.150	0.875	–
3	Steam	600	0.150	0.875	–
4	Steam	543	0.118	0.989	–
5	Steam	106	0.118	0.989	–
6	R245fa	34.0	0.240	37.93	–
7	R245fa	34.5	1.14	37.93	–
8	R245fa	68.1	1.14	37.93	–
9	R245fa	96.6	1.14	37.93	–
10	R245fa	55.8	0.240	37.93	–
11	R245fa	34.0	0.240	37.93	–
w_{P1}	–	–	–	–	51.5 W_e
q_{H1}	–	–	–	–	3.23 MW_{th}
q_{HX1}	–	–	–	–	1.75 MW_{th}
w_{P2}	–	–	–	–	36.2 kW_e
q_{H2}	–	–	–	–	7.01 MW_{th}
w_{T2}	–	–	–	–	1.00 MW_e
q_{C2}	–	–	–	–	7.80 MW_{th}

Table A.3.3 The process stream data and main results of devices at 24 min (t_d/2) in discharging time

Stream number or variables	Material	Temperature [°C]	Pressure [MPa]	Flow rate [kg/s]	Result of device
1	Steam	25.0	0.100	1.61	–
2	Steam	25.0	0.150	1.61	–
3	Steam	200	0.150	1.61	–
4	Steam	497	0.118	1.45	–
5	Steam	106	0.118	1.45	–
6	R245fa	34.0	0.240	51.9	–
7	R245fa	34.6	1.14	51.9	–
8	R245fa	84.9	1.14	51.9	–
9	R245fa	105	1.14	51.9	–
10	R245fa	65.0	0.240	51.9	–
11	R245fa	34.0	0.240	51.9	–
w_{P1}	–	–	–	–	81.2 W_e
q_{H1}	–	–	–	–	4.65 MW_{th}
q_{HX1}	–	–	–	–	3.71 MW_{th}
w_{P2}	–	–	–	–	48.4 kW_e
q_{H2}	–	–	–	–	8.76 MW_{th}
w_{T2}	–	–	–	–	1.42 MW_e
q_{C2}	–	–	–	–	11.1 MW_{th}

Chapter 4

Improvement on Environmentally Friendly Process and Economics Evaluations

4.1. Abstract

This chapter focused on the additional performance evaluation of the TCS system integrated with a biomass power plant described in Chapter 3. The power generation strategy was also the same for that of Chapter 3. In this chapter, there were three objectives. First, process performances were compared when R245fa or R1233zd was used as a working fluid of ORC, and influences of ORC parameters such as the turbine inlet temperature, superheat temperature, and the scale of the power generation, were evaluated. In addition, effects of the fluidized bed volume and the reduction of biomass fuel consumption were also investigated. Second, a potential of the proposed process that can absorb the VRE fluctuation was evaluated by the dynamic calculation. Third, economics of the TCS system was evaluated. Results show that the round-trip efficiency of the process using R1233zd was 8.77%, which was slightly lower than that of the process using R245fa (8.84%). However, the differences were small (< 0.1%). The increases of the turbine inlet temperature led to the increase of heat recovery from the outlet steam of the TCS reactor, meanwhile, the round-trip efficiency decreased. The efficiencies of the cases changing the superheat temperature (5 → 15 °C) were slightly changed (< 0.5%). To achieve high energy efficiencies, a large-scale biomass power plant and a small-fluidized bed volume was effective. It was found that the VRE fluctuation was mostly absorbed by the TCS system with a fluidized bed and ORC process. In the economics evaluations, the levelized cost of storage regarding only the TCS system was 0.92–2.37 USD/kWh$_e$ when the charging electricity cost is 0.05 USD/kWh$_e$. LCOS also decreases to 0.50–1.14 USD/kWh$_e$ if the electricity cost is free during daytime in the future and power output is two times in a day.

4.2. Improvement of the TCS System Integrated with a Biomass Power Plant

4.2.1. Base Case

The whole process is already shown in Figure 3.1. Table 4.1 shows the main parameters of the fluidized bed reactor and process simulation, respectively. Temperature of stream 6 was set to be 40 °C because cooling water is used generally around 30 °C. Pressure of stream 6 was saturated pressure of the organic working fluid at 40 °C. H2 outlet temperature (stream 9) was set to be 90 °C. P2 outlet pressure (stream 7 or 7') was saturated pressure at 85 °C (i.e., 90 – 5 °C) by assuming the superheat temperature was 5 °C for practical operation [135].

Similar to the methods written in Chapter 3, in the normal operation and the charging time, the mass flow rate of R245fa was determined so that the scale of the biomass power plant is 1 MW_e. In the discharging time, H2 duty was set to be the same for the value of normal operation, and the mass flow rate of R245fa was determined so that H2 outlet temperature is 90 °C. The heat exchange area of HX1 (A_{HX1}) was determined so that H2 duty reduction in the charging time ($-\Delta Q_{H2}$) is 20%. the dynamic calculation of the fluidized bed reactor was carried out by using Visual Basic for Application® (version 7.1), and the process simulation was carried out by using Aspen Plus® (version 12).

Table 4.1 The input parameters regarding the process simulation

Parameters	Stream number in Figure 3.1	Unit	Normal operation	Charging	Discharging
TCS					
Working fluid	1–5	–	–	H_2O	H_2O
Mass flow rate	1	kg/s	–	0.875	1.61
Temperature	1	°C	–	25.0	25.0
Pressure	1	MPa	–	0.1	0.1
P1 outlet pressure	2	MPa	–	0.15	0.15
H1 outlet temperature	3	°C	–	600	200
Heat exchange area of HX1	–	m^2	–	80.0	80.0
ORC					
Working fluid	6–11	–	R245fa	R245fa	R245fa
Mass flow rate	6–11	kg/s	45.93	45.93	Variable
Temperature	6	°C	40.0	40.0	40.0
Pressure	6	MPa	0.250	0.250	0.250
P2 outlet pressure	7	MPa	0.89	0.89	0.89
H2 outlet temperature	9	°C	90	90	90
H2 heat duty	–	MW_{th}	–*1	–*1	10.1
T2 outlet pressure	10	MPa	0.250	0.250	0.250
C2 outlet temperature	11	°C	40.0	40.0	40.0

*1: The value is not input parameter.

4.2.2. Changing Parameters of ORC

The influences of the ORC parameters (working fluid, H2 outlet temperature, superheat temperature, T2 power output) on the energy efficiencies were investigated. In the base case, R245fa was used as working fluid of the ORC. R245fa has high GWP (= 858) and high toxicity in spite of no flammability and ODP (= 0) [135]. On the other hand, R1233zd has GWP = 1, ODP = 0, no flammability, and no toxicity [135]. Thus, R245fa and R1233zd were compared in this chapter. The varied parameters are summarized in Table 4.2. The results caused by the different organic material can be obtained by comparing the cases 0–2 (R245fa) and cases 3–5 (R1233zd). In the cases 0–2, H2 outlet temperature was changed, and P2 outlet pressure was set so that the saturated temperature was 5 °C lower than H2 outlet temperature (i.e., the superheat temperature was fixed to be 5 °C in the heater H2). The same comparison in the case of R1233zd was made in cases 3–5. In case 6, the superheat temperature was increased from 5 (case 3) to 15 °C (case 6), leading to the same P2 outlet pressure. T2 power output was changed to 0.5 and 0.2 MW_e in cases 7 and 8, respectively. The overall heat transfer coefficients between H_2O and organic materials (see Table 3.5) were assumed to be the same in each organic material, although the value is influenced by the organic material, the mass flow rate, and the structure of heat exchanger. A_{HX1} was determined so that $-\Delta Q_{H2}$ is 20% in the cases 0–8.

In addition, the effects of the fluidized bed volume were investigated in case the of R1233zd (cases 3, 9–16). The parameters of the case study are summarized in Table 4.3. The fluidized bed volume was changed to 7, 10, and 13 m^3, and the A_{HX1} was determined so that $-\Delta Q_{H2}$ was 10, 20, or 30%.

Table 4.2 The parameters of case study regarding ORC

Case	Working fluid	Pressure of stream 6 [MPa]	Temperature of stream 6 [°C]	P2 outlet pressure [MPa]	H2 outlet temperature [°C]	T2 output [MW_e]
0 (base)	R245fa	0.25	40	0.89	90	1.0
1	R245fa	0.25	40	0.69	80	1.0
2	R245fa	0.25	40	0.53	70	1.0
3	R1233zd	0.22	40	0.74	90	1.0
4	R1233zd	0.22	40	0.58	80	1.0
5	R1233zd	0.22	40	0.45	70	1.0
6	R1233zd	0.22	40	0.74	100	1.0
7	R1233zd	0.22	40	0.74	90	0.50
8	R1233zd	0.22	40	0.74	90	0.20

Table 4.3 The parameters of case study regarding the fluidized bed volume

Case	Organic material	Fluidized bed volume [m^3]	$-\Delta Q_{H2}$ [%]
9	R1233zd	7	10
10	R1233zd	7	20
11	R1233zd	7	30
12	R1233zd	10	10
3	R1233zd	10	20
13	R1233zd	10	30
14	R1233zd	13	10
15	R1233zd	13	20
16	R1233zd	13	30

4.2.3. VRE Fluctuation

In Chapter 2, the absorption of the VRE fluctuation by the fluidized bed reactor was evaluated. In this chapter, the absorption of the VRE fluctuation through the TCS system and the biomass power plant was evaluated. To represent the VRE fluctuation, eq. (2.24) was also used. The parameters are summarized in Table 4.4. R1233zd was used as organic material in this evaluation. The input fluctuation is shown in Figure 4.1. In this calculation, H2 duty (8.16 MW_{th}) and A_{HX1} (80 m^2) was set to be the same for that of the case of the $-\Delta Q_{H2} = 20\%$.

The absorption of the VRE fluctuation was quantitatively evaluated by using the following equations.

$$\Delta q_{\text{total}} = \sum_{t=13.4}^{60.3} \left| q_{\text{heat},t+\text{d}t} - q_{\text{heat},t} \right| \quad (4.1)$$

$$\Delta w_{\text{total}} = \sum_{t=13.4}^{60.3} \left| w_{\text{T2},t+\text{d}t} - w_{\text{T2},t} \right| \quad (4.2)$$

$$\text{absorption ratio [\%]} = \frac{w_{\text{T2,max}} - w_{\text{T2,min}}}{q_{\text{heat,max}} - q_{\text{heat,min}}} \quad (4.3)$$

where Δq_{total} [MW_{th}] and Δw_{total} [kW_e] is the summations of the absolute of the differences of q_{heat} and w_{T2}, respectively. To evaluate the performance during only reaction time, the integral time was set to be from 13.4 to 60.3 min (absorption ratio was also calculated under the same conditions). Note the author confirmed that reaction did not occur during heating from the initial temperature to the target temperature (i.e., from 0 to 13.4 min) and after the completion of the reaction at 60.3 min. By comparing Δq_{total} and Δw_{total} during the charging time, the absorption of the VRE fluctuation by the TCS system can be evaluated. In addition, the absorption of the fluctuation magnitude was evaluated by the absorption ratio.

Table 4.4 The parameters regarding the VRE fluctuation

Case	H2 outlet temperature [°C]	$q_{fluctuation}$ [kW_{th}]	q_{min} [kW_{th}]	Range of q_{heat} [kW_{th}]
3	90	0	700	700
17	90	400	500	500–900
18	90	800	300	300–1100
19	80	400	500	500–900
20	80	800	300	300–1100
21	70	400	500	500–900
22	70	800	300	300–1100

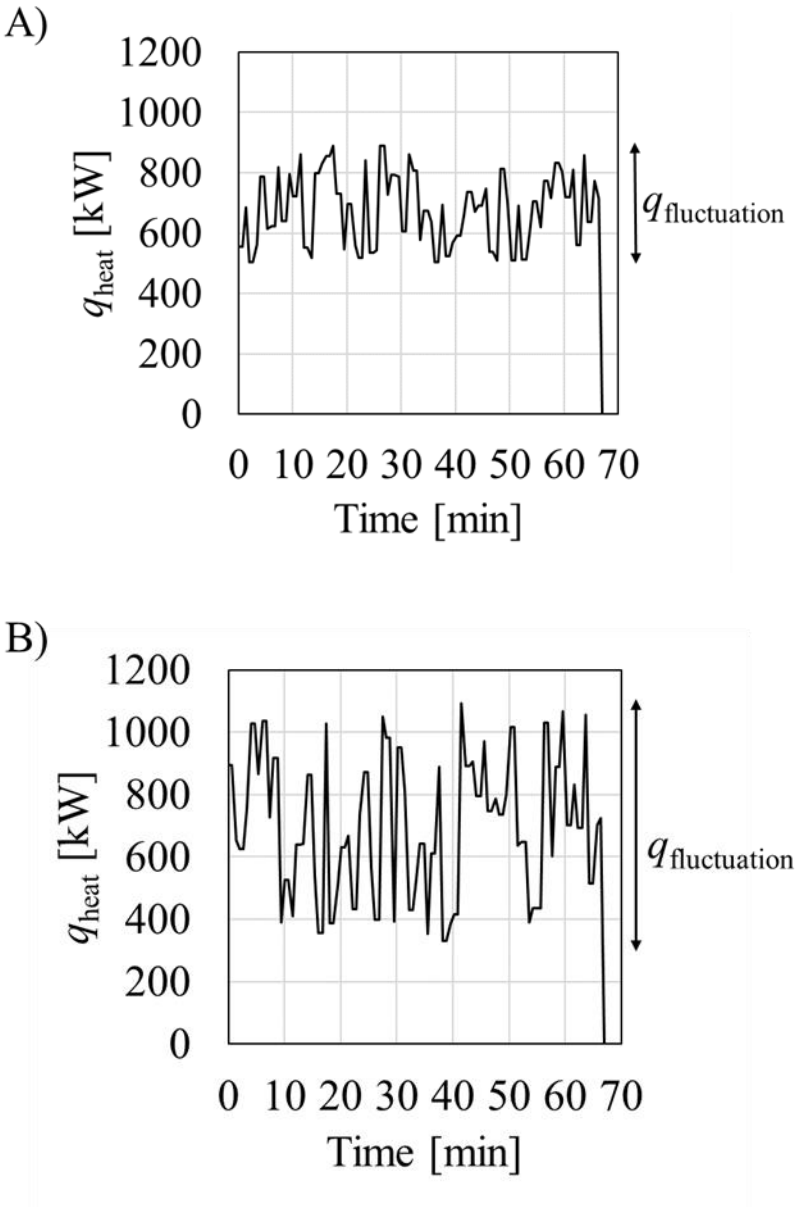

Figure 4.1 Input fluctuation of heat into the reactor (A) $q_{fluctuation}$ = 400 kW_{th}, (B) $q_{fluctuation}$ = 800 kW_{th})

4.2.4. Process Evaluation Methods

The process evaluation methods were the same as written in section 3.2.6.

4.2.5. Economics (cost estimation)

The author calculated capital and operating costs of the TCS system in the cases shown in Table 4.3. Capital cost includes the costs of the fluidized bed reactor, water tank, pump (P1), electric heater (H1), and heat exchanger (HX1). The details are given in Table 4.5. The reactor volume was calculated by 1.5 times of the fluidized bed volume [160]. The equipment cost of gas distributor (trays), cyclone (placed after the reactor to collect the particles), and electric heaters were included in the reactor cost. In the reactor cost calculation, the reactor size was assumed that the ratio of height per diameter (H_B/D_B) was 4. The water tank volume was assumed to be 1 m^3 for all cases in this study. P1 and H1 costs were calculated from the maximum work and duty, respectively. The electric heater cost was estimated with reference to Peters et al. (i.e., 1243 USD for 117 kW_e) [161]. The operating cost contains CaO powder, alumina particles, and maintenance cost. The details are given in Table 4.6. Note that the cost of materials initially used was included in the capital cost, and the replacement frequency of the materials were assumed to be 3 times/year (that was estimated from the cyclability > 100 cycles [28]). The charging electricity cost was assumed to be 0.05 USD/kWh_e. The water cost for the working fluid for the TCS system was not contained because the needed mass cannot be estimated, and it was considered that the water cost is low compared to other equipment (0.26–2.45 USD/t [162]).

The capital cost was calculated by the following equations [135,162].

$$\log C_{\mathrm{p}}^{0} = K_1 + K_2 \log Z + K_3 (\log Z)^2 \quad (4.4)$$

$$F_{BM} = B_1 + B_2 F_{\mathrm{M}} F_{\mathrm{P}} \quad (4.5)$$

$$C_{\mathrm{BM},1} = F_{\mathrm{BM}} C_p^0 \quad (4.6)$$

$$C_{\mathrm{BM},2} = C_{\mathrm{BM},1}\left(\frac{\mathrm{CEPCI}_{\mathrm{year2}}}{\mathrm{CEPCI}_{\mathrm{year1}}}\right) \quad (4.7)$$

$$C_{\mathrm{capital}} = 1.18\sum C_{\mathrm{BM},2} \quad (4.8)$$

where C_{p}^{0} is the purchased cost for base conditions (ambient pressure and temperature, carbon steel), K is the coefficient for C_{p}^{0} calculation [-], Z is the equipment cost attribute [m^2, m^3, or kW], F_{BM} is the bare module cost factor [-], B is the coefficient for considering pressure and material [-], F_{M} is the material factor [-], F_{P} is the pressure factor [-], C_{BM} is the bare module equipment cost, CEPCI is the chemical engineering plant cost index [-], and C_{capital} is the capital cost. Note that K and B of each equipment are different. $\mathrm{CEPCI}_{\mathrm{year2}}$ was 797.6 as of January, 2022 [163]. The main other parameters are summarized in Table 4.7. The total capital cost, the total operating cost, power generation, and levelized cost of storage (LCOS [USD/kWh_e]) attributed to the TCS system were calculated by the following equations [164,165].

$$C_{\mathrm{T,c}} = \sum_{i=1}^{\text{depreciation periods}}\left(\frac{C_{\mathrm{capital}}-\text{residual value}}{\text{depreciation periods}} \times \frac{1}{1+r}^{\,i-1}\right) \quad (4.9)$$

$$C_{\mathrm{T,o}} = \sum_{i=1}^{\text{depreciation periods}}\left(C_{\mathrm{operation}} \times \frac{1}{1+r}^{\,i-1}\right) \quad (4.10)$$

$$E_{\mathrm{T}} = \sum_{i=1}^{\text{depreciation periods}}\left(\int\left(w_{\mathrm{T2},t} - w_{\mathrm{T2,n}}\right)\mathrm{d}t \times \frac{1}{1+r}^{\,i-1}\right) \quad (4.11)$$

$$\mathrm{LCOS}\ [\mathrm{USD/kWh_e}] = \frac{C_{\mathrm{T,C}}+C_{\mathrm{T,O}}}{E_T} \quad (4.12)$$

where $C_{\mathrm{T,c}}$ is the total capital cost [USD], r is the discount factor [-], $C_{\mathrm{T,o}}$ is the total operating cost [USD], E_{T} is the total power output discharged by the TCS system [kWh_e].

Table 4.5 The calculation conditions of the capital cost

Equipment	Configuration	material	*Z*
Fluidized bed reactor	Reactor, Tray, Cyclone	Stainless steel	Volume [m^3], Cross area [m^2], Volume [m^3]
Water tank	Vertical vessels	Carbon steel	Volume [m^3]
P1	Centrifugal	Carbon steel	Work [kW]
H1	Electric immersion heater	–	Heat duty [kW]
HX1	Fixed tube	Stainless steel	Heat exchange area [m^2]

Table 4.6 The calculation conditions of the operating cost

Item	Cost	Ref.
CaO	0.0043 USD/kg	[166]
Alumina	0.55 USD/kg	[167]
Charging electricity	0.05 USD/kWh_e	–
Maintenance cost	5% of the capital cost	[162]

Table 4.7 The other parameters for cost calculation

Parameter	Value
Depreciation periods	20 years
Residual value	10% of the capital cost
Discount factor	7%
Operating days	335 days

4.3. Results and Discussion

4.3.1. Base Case

Table 4.8 shows the results of process simulation for the base case. The $\eta_{storage}$, η_{TCS}, η_{energy} were 65.6%, 68.1%, 8.84%, respectively. In section 3.3.2, $\eta_{storage}$, η_{TCS}, η_{energy} were 58.5, 61.0, 9.79, respectively. Thus, $\eta_{storage}$ and η_{TCS} were higher, and η_{energy} was lower than that of section 3.3.2 although the fluidized bed volume, $-\Delta Q_{H2}$, and T2 output were the same. The main differences were P2 outlet pressure, H2 outlet temperature, and C2 outlet temperature. W_{P2} was lower because P2 outlet pressure was lower (Note 1.14 MPa in section 3.3.2). H2 outlet temperature was lower (96.7 °C in section 3.3.2), and C2 outlet temperature was higher (34.0 °C in section 3.3.2) because of more stringent condition (40 °C) for practical application. Low P2 outlet pressure, low H2 outlet temperature, and high C2 outlet temperature led to high mass flow rate so that T2 output becomes 1 MW_e. Thus, H2 and C2 duty was higher. This is the reason why η_{energy} was lower. However, the high mass flow rate caused the increase of the heat recovery from the outlet steam of the TCS reactor (this leads to higher HX1 duty). Thus, $\eta_{storage}$ and η_{TCS} increase. Note that superheat temperature was 5 °C, and this effect was not significant.

Table 4.8 The results of base case

Parameters	Normal operation	Charging	Discharging
Reaction time	–	67 min	48 min
A_{HX1}	–	80 m^2	80 m^2
Input			
W_{P1}	–	0.23 MJ	0.23 MJ
W_{P2}	25.2 kW_e	0.099 GJ	0.102 GJ
Q_{H1}	–	13.0 GJ	13.4 GJ
Q_{H2}	10.1 MW_{th}	32.5 GJ	26.2 GJ
Q_{heat}	–	2.81 GJ	–
Storage			
$Q_{chemical}$	–	2.05 GJ	–
$Q_{sensible}$	–	124 MJ	–
Q_{HX1}	–	8.20 GJ	11.7 GJ
$-\Delta Q_{H2}$	–	8.20 GJ	–
$Q_{storage}$	–	10.4 GJ	–
Output			
W_{T2}	1.00 MW_e	4.02 GJ	4.04 GJ
Waste			
The waste steam energy after HX1	–	5.66 GJ	3.19 GJ
Q_{C2}	9.16 MW_{th}	36.8 GJ	36.9 GJ
Efficiency			
$\eta_{storage}$	–	65.6%	–
η_{TCS}	–	–	68.1%
η_{energy}	9.85%	11.4%	8.84%

4.3.2. Changing ORC Parameters

Table 4.9 shows the calculated results for cases 0–8 (case 0 is the base case). The trends of cases 0–2 were the same for those of cases 3–5. Figure 4.2 shows the *T*-*Q* diagram of HX1 for cases 3–5. The results of cases 3–5 shows that $\eta_{storage}$ and η_{TCS} increase as H2 outlet temperature decreases. The low H2 outlet temperature leads to high mass flow rate so that T2 output is kept 1 MW_e. A_{HX1} increases to increase H2 duty ($-\Delta Q_{H2}$ [MJ]) although $-\Delta Q_{H2}$ [%] was constant. As H2 outlet temperature decreases, the $-\Delta Q_{H2}$ [MJ] approaches the energy contained in the outlet steam from the TCS reactor. Thus, $\eta_{storage}$ and η_{TCS} increase as H2 outlet temperature decreases. H2 and C2 duty increases due to the increasing mass flow rate. This leads to the decrease of η_{energy} as H2 outlet temperature decreases. Figure 4.3 shows T2 output change for cases 0–5. Although the mass flow rate increases, T2 output during discharging time decreases. The reasons are low H2 outlet temperature and low P2 outlet pressure. Thus, η_{energy} decreases as H2 outlet temperature decreases. The behavior of T2 output during discharging time was the same behavior reported in section 3.3.5.

Next, the results for R245fa (cases 0–2) and R1233zd (cases 3–5) were compared (cf. Table 4.9). η_{energy} of R1233zd was slightly lower than that of R245fa for all cases. $\eta_{storage}$ and η_{TCS} of R1233zd was slightly higher than that of R245fa (cases 1, 2, 4, 5). The density of R245fa is 1.32 t/m^3, and that of R1233zd is 1.24 t/m^3 at 40 °C (calculated by using Aspen Plus). In addition, the saturated pressure of R1233zd (0.74 MPa at 85 °C) is lower than that of R245fa (0.89 MPa at 85 °C), and this leads to the lower P2 outlet pressure. Thus, the mass flow rate of R1233zd is larger than that of R245fa under the conditions of the same H2 outlet temperature to keep T2 output 1 MW_e in the normal operation. The large mass flow rate causes the increase of heat recovery from the outlet steam of TCS reactor, leading to high $\eta_{storage}$ and η_{TCS}. In addition, it causes the increase of H2 and C2 duty that leads to low η_{energy}. However, $\eta_{storage}$ and η_{TCS} of case 3 is lower than that of case 0 although the mass flow rate and A_{HX1} of case 3 was

higher. The specific heat capacity of R245fa and R1233zd were 1.34 and 1.22 kJ/kg/K at 40 °C (calculated by using Aspen Plus), respectively. The lower specific heat capacity leads to the higher HX1 outlet temperature. However, the temperature differences become small in HX1. Thus, the heat duty was small, leading to lower $\eta_{storage}$ and η_{TCS}. Figure 4.3 shows the differences of T2 output between R245fa (cases 0–2, solid lines) and R1233zd (cases 3–5, dotted lines) are small.

The results of cases 3 and 6 show the effects of superheat temperature. The mass flow rate decreases, and A_{HX1} increases as the superheat temperature increases because T2 output was kept 1 MW_e. This causes high $\eta_{storage}$, and low η_{energy} for case 6. However, the differences of three efficiencies were small (< 0.5%), and it was found that the superheat temperature has small effects on these efficiencies.

The results of cases 3, 7, and 8 show that the effects of the scale of the biomass power plant (0.20 and 0.50 MW_e). T2 output was controlled by changing the mass flow rate although $-\Delta Q_{H2}$ was fixed (20%) in this study. The energy efficiencies dramatically decreased as T2 output decreases. The reason is that H2 duty decreases as T2 output decreases, and this results in the lower required energy so that $-\Delta Q_{H2}$ approaches 20%. Thus, the energy recovered from the outlet steam of the TCS reactor decreases, and the energy efficiencies decreased.

In summary, the differences of the efficiencies between R245fa and R1233zd were small. Thus, R1233zd is preferable to R245fa because of lower GWP, lower ODP, no flammability, and no toxicity. In addition, energy efficiencies were influenced by various parameters such as P2 outlet pressure, H2 outlet temperature, T2 output, A_{HX1}, and $-\Delta Q_{H2}$. If the energy from VRE is infinite (or abundant), the importance of $\eta_{storage}$ and η_{TCS} are lower than that of η_{energy}. Thus, η_{energy} is the most important parameter.

Table 4.9 The results for cases 0–8

Case	Mass flow rate [kg/s]	A_{HX1} [m^2]	$-\Delta Q_{H2}$ [%]	$\eta_{storage}$ [%]	η_{TCS} [%]	η_{energy} [%]	η_{energy} [%] (normal operation)
0 (base)	45.9	80	20.1	65.6	68.1	8.84	9.85
1	57.7	93	20.0	76.3	79.7	7.63	8.09
2	78.6	120	19.9	96.3	94.4	6.08	6.16
3	46.4	81	19.9	65.4	67.5	8.77	9.79
4	58.5	96	20.0	77.1	80.1	7.57	8.01
5	79.8	125	19.9	97.2	95.1	6.00	6.07
6	44.7	82	19.9	65.7	67.5	8.74	9.75
7	23.2	47	20.2	39.9	40.6	6.97	9.79
8	9.28	11	20.4	24.3	18.9	4.22	9.79

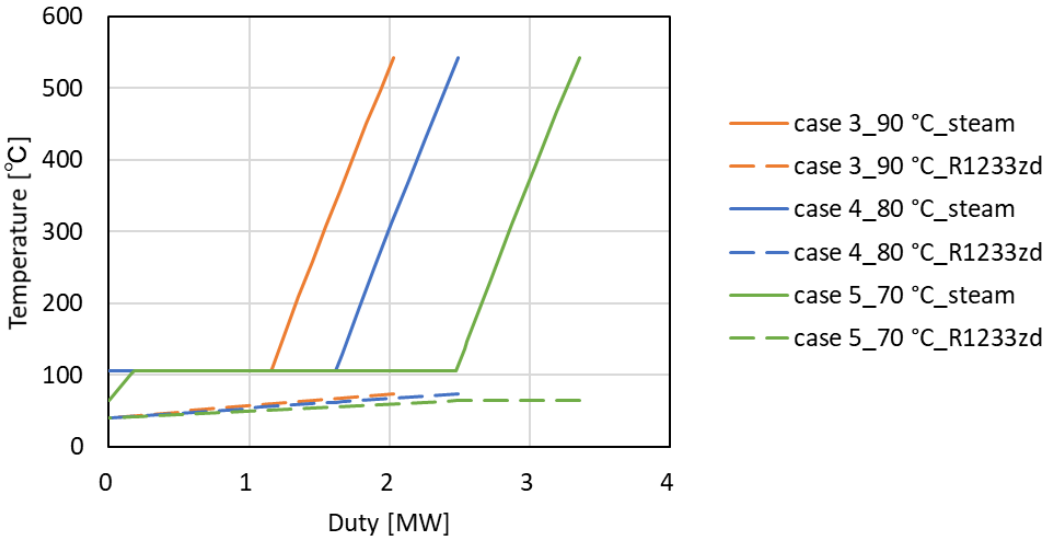

Figure 4.2 *T-Q* diagram of HX1 for cases 3–5 (note that $-\Delta Q_{H2}$ of these cases are 20%)

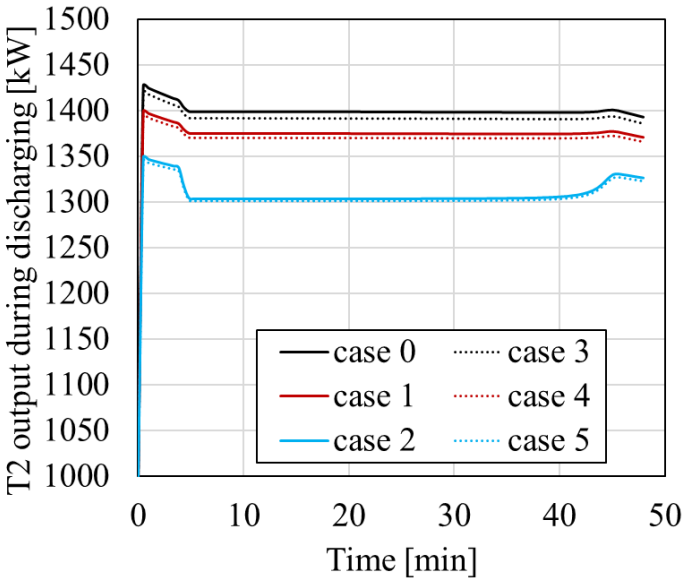

Figure 4.3 T2 output during discharging for cases 0–5

4.3.3. Fluidized Bed Volume Effects

Table 4.10 shows the results for cases 3, 9–16. The energy efficiencies decrease as the fluidized bed volume increases in the cases of the similar $-\Delta Q_{H2}$. The reason is clear that the high steam flow rate leads to low heat transfer amount in HX1 because the heat transfer amount was determined by $-\Delta Q_{H2}$ [%]. A_{HX1} increases as $-\Delta Q_{H2}$ increases in the cases of the same fluidized bed volumes, and this leads to high energy efficiencies for all the cases because the energy of steam can be recovered in HX1. In cases 9, 12, 14, A_{HX1} of case 12 is the largest although A_{HX1} of the case of the largest volume is maximum in case of cases 10, 3, 15 and 11, 13, 16. The reason is the different overall heat transfer coefficients in the case of different fluid state, and the same tendency was reported in section 3.3.3. The differences of the η_{energy} between the case by using the TCS system and the normal operation were 2.34% at the highest for case 14 and 0.11% at the lowest for case 11. The time profiles of T2 output during discharging time are shown in Figure 4.4. When the fluidized bed volume is 7 m^3, T2 output of cases 10 and 11 were almost the same at 5–42 min because the energy of steam can be recovered enough as A_{HX1} is over 78 m^2 during discharging time. T2 output was influenced by the fluidized bed volume (that is related to the steam flow rate) and A_{HX1}.

Table 4.10 The A_{HX1} and energy efficiencies of cases 3, 9–16

Case	Fluidized bed volume [m^3]	$-\Delta Q_{H2}$[*1] [%]	A_{HX1} [m^2]	$\eta_{storage}$ [%]	η_{TCS} [%]	η_{energy} [%]	η_{energy} [%] (normal operation)
9	7	9.8	40	51.1	53.5	8.61	9.79
10	7	19.9	78	85.9	88.3	9.50	9.79
11	7	23.7[*2]	107	98.7	95.6	9.68	9.79
12	10	10.0	45	39.8	42.2	8.06	9.79
3	10	19.9	81	65.4	67.5	8.77	9.79
13	10	30.0	134	91.5	91.2	9.50	9.79
14	13	10.0	43	32.4	33.1	7.45	9.79
15	13	20.1	85	53.5	54.9	8.14	9.79
16	13	30.1	134	74.2	75.2	8.84	9.79

[*1] $-\Delta Q_{H2}$ is not exactly 10, 20, and 30% because $-\Delta Q_{H2}$ is not input value. However, the calculation results were adjusted by changing A_{HX1}

[*2] $-\Delta Q_{H2}$ does not approach 30% because the steam flow rate from the reactor is low, and almost all of the steam energy was recovered by HX1.

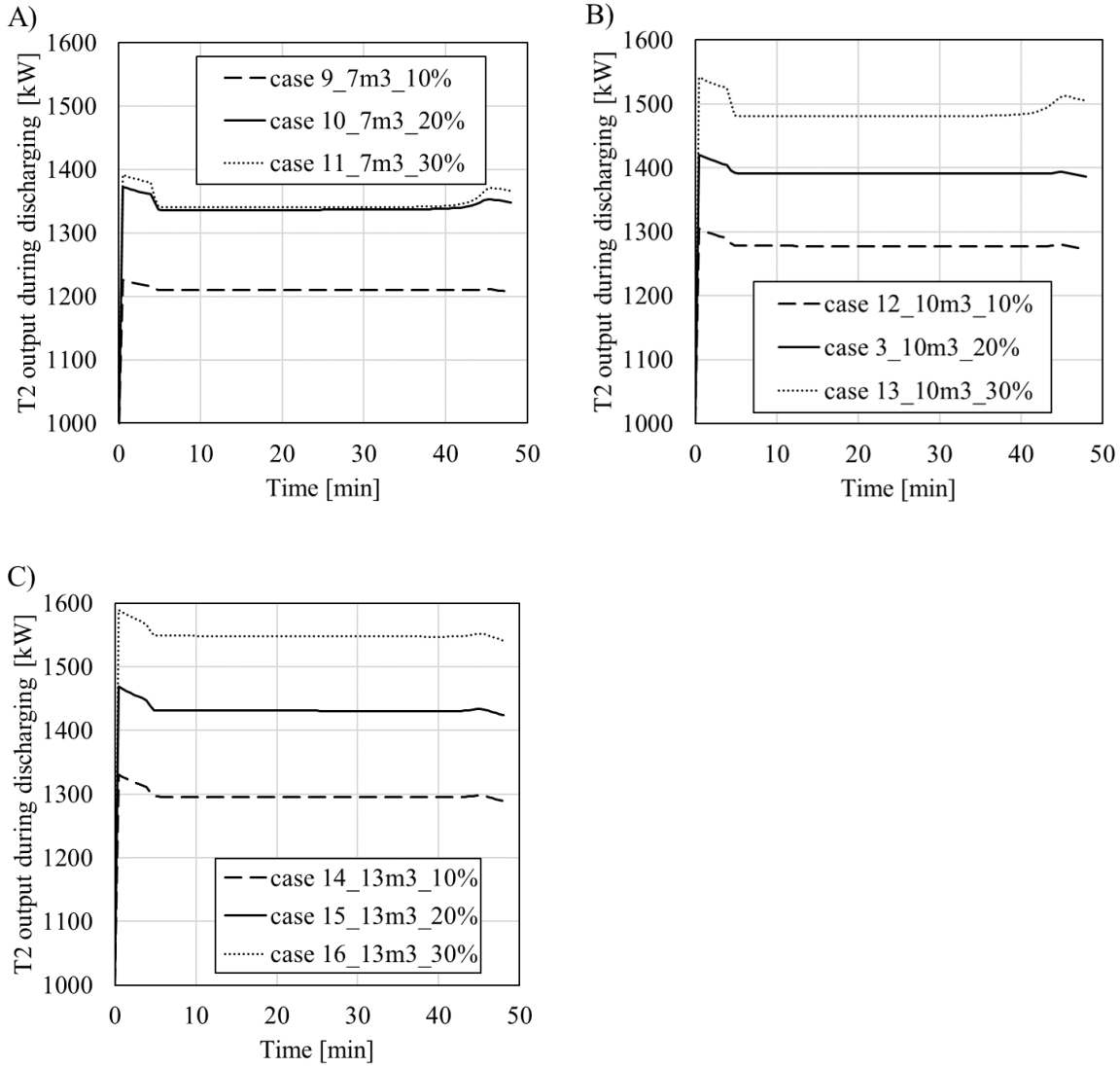

Figure 4.4 Time profiles of T2 output for cases 3, 9–16 during discharging time

4.3.4. Absorption of the VRE Fluctuation by Fluidized Bed TCS System

Figure 4.5 shows the changes of the heat input to the fluidized bed TCS system and T2 output during charging time. Table 4.11 shows the results for the effects of the absorption of the VRE fluctuation. The heat from the VRE was entering in the TCS reactor (q_{heat}). It was found that almost all of the VRE fluctuation was absorbed through the dehydration reaction and heat transfer in the process. The fluctuation was absorbed by the TCS reactor mainly. The fluctuation changed to the steam temperature and flow rate fluctuation, transferred by steam to the ORC through HX1, and the fluctuation comes out from the process by T2 as the electricity fluctuation (w_{T2}). Δw_{total} was much smaller than Δq_{total}, and the absorption ratio was 0.231–1.16%. Thus, the electricity fluctuation can be ignored. Figure 4.6 shows the fluctuation of w_{T2} (cases 18, 20, 22) and q_{heat} when $q_{flctuation}$ was 800 kW_{th} (time was 13.4–40.2 min as an example). In case 22, the fluctuation behavior was the same for q_{heat}. However, interestingly, the fluctuation behavior of cases 18 and 20 was reversed. This tendency was observed in the cases 17, 19, 21. When q_{heat} decreases, the mass flow rate and the temperature of the steam from the TCS reactor decreases. Normally (e.g., case 22), the heat exchange amount also decreases, and T2 output decreases, leading to the same fluctuation tendency. On the other hand, in cases 18 and 20, the steam was condensed slightly faster compared to the case of no fluctuation because the mass flow rate and the temperature was low. As the results, the heat exchange amount increases due to the increase of the overall heat transfer coefficient (U). T2 output, then, increases although q_{heat} decreases. In case 22, the latent heat of the steam was recovered completely (see case 5 in Figure 4.2), and the fluctuation was not reversed (i.e., the heat exchange amount depended on the mass flow rate mainly). When q_{heat} increases, the opposite phenomenon was observed. The cases of H2 outlet temperature of 80 °C (cases 19 and 20) were lowest absorption ratio. Comparing with cases 18 and 20, the mass flow rate of R1233zd of case 20 was higher than that of case 18. The high mass flow rate can alleviate the fluctuation

of steam temperature. Comparing with the results of cases 20 and 22, the temperature difference in HX1 of case 22 is higher than that of case 20 (see cases 4 and 5 in Figure 4.2). If a temperature difference is large, the fluctuation of steam temperature cannot be alleviated in HX1.The same trends were observed in cases 17, 19, 21. Thus, the cases 19 and 20 was lowest absorption ratio. $H_{storage}$ decreases as $q_{fluctuation}$ increases. The tendency may be changed if the fluctuation data are changed. In this study, q_{heat} of cases 17, 19, 21 ($q_{fluctuation}$ = 400 kW_{th}) and cases 18, 20, 22 ($q_{fluctuation}$ = 800 kW_{th}) were the same data. However, if the q_{heat} has different fluctuation, $\eta_{storage}$ may increase as $q_{fluctuation}$ decreases because $\eta_{storage}$ is influenced by the average of q_{heat} (see Figures 2.8 and 2.9). Above all, the VRE fluctuation can be absorbed by the integrated process. However, mechanical performance should be largely influenced by the fluctuation, and the influences must be evaluated in detail. In particular, the influence of the fluctuation on the behavior of electric heaters of the TCS reactor must be evaluated.

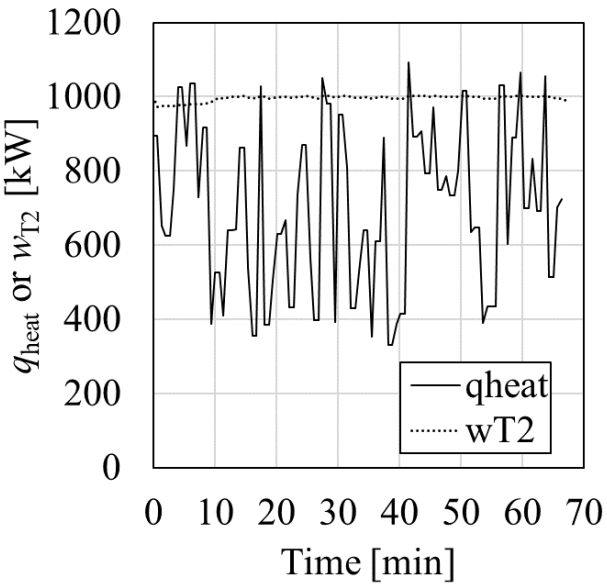

Figure 4.5 The changes of the heat into TCS reactor (q_{heat}) and T2 output (w_{T2}) during charging time for case 22 (T2 output of case 22 is most large fluctuation)

Table 4.11 Results of the absorption of the VRE fluctuation

Case	Δq_{total} [MW_{th}]	Δw_{total} [kW_e]	Fluctuation range of q_{heat} [kW_{th}]	Fluctuation range of w_{T2} [kW_e]	Absorption ratio [%]	$\eta_{storage}$ [%]
3	0	0	0	0	–	65.6
17	5.92	16.3	388	1.47	0.378	65.5
18	11.9	32.4	763	2.20	0.288	65.4
19	5.92	13.1	388	1.18	0.303	77.3
20	11.9	25.9	763	1.76	0.231	77.1
21	5.92	64.4	388	4.50	1.16	99.3
22	11.9	121	763	7.95	1.04	99.0

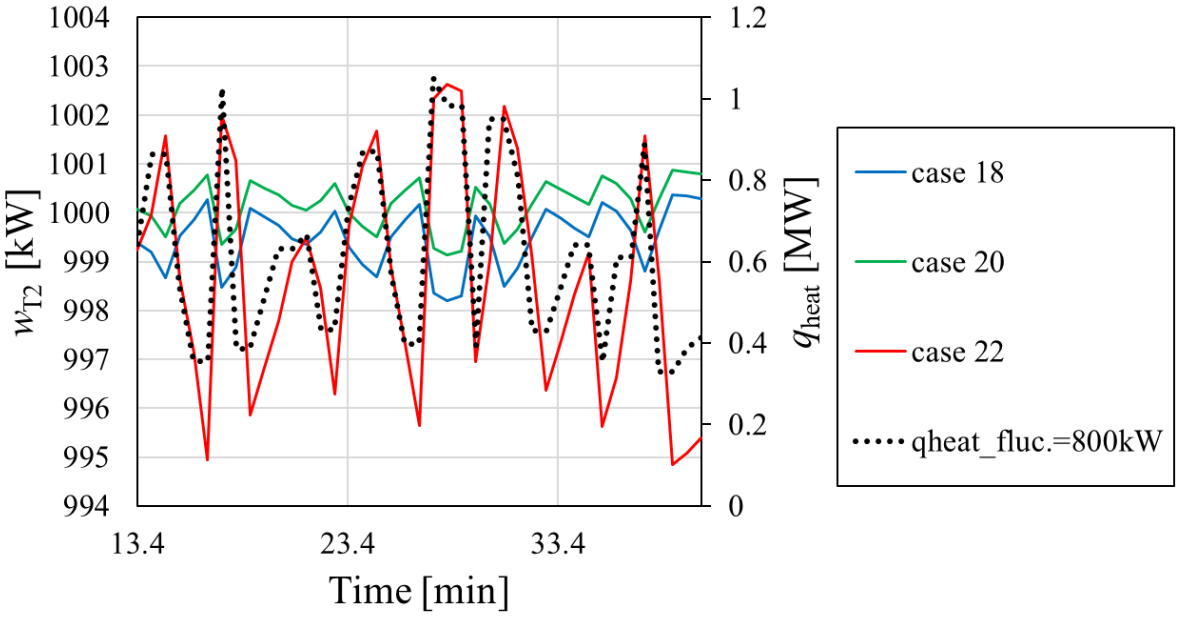

Figure 4.6 The fluctuation of w_{T2} (cases 18, 20, 22) and q_{heat} (Time: 13.4–40.2 min)

4.3.5. Economics Evaluations

Table 4.12 shows the capital cost, operating cost, and LCOS for cases 3, 9–16. The capital cost, operating cost, and LCOS increase as the fluidized bed volume increases. As $-\Delta Q_{H2}$ increases, the capital cost increases because A_{HX1} increases, and it leads to high operating cost that contains maintenance cost (i.e., 5% of the capital cost). However, the LCOS decreases because T2 output during discharging time increases (see Figure 4.4). The LCOS regarding only TCS system was 0.92 USD/kWh$_e$ at the lowest (case 11) and 2.37 USD/kWh$_e$ at the highest (case 14). Figure 4.7 shows the $C_{BM,2}$ of each equipment for cases 3, 9–16. The capital cost of the main equipment was in this order: electric heaters (H1), heat exchanger (HX1), reactor, and the others (alumina, CaO, pump, and water tank costs) for all cases. The others had insignificant effects on the capital cost. The capital cost was 0.42 million USD at the lowest (case 9) and 0.65 million USD at the highest (case 16) because of the effects of the reactor volume and A_{HX1}. Operating cost was also influenced by those parameters because the maintenance cost was set to be 5% of capital cost.

Bayon et al. reported that the total capital cost of the TCS system integrated with CSP plant is 4.78 USD/MJ (100 MW$_e$/294 MW$_{th}$-scale) [137], and the total capital cost in this study was 0.06–0.12 USD/MJ. The main reason is considered that three tanks were necessary in the process proposed in the previous study. Thus, the total capital cost of this study was lower than that of the previous study. Elshurafa et al. [168] summarized the LCOS of various energy storage methods for utility-scale (1–300 MW) that is 0.23–0.37 €/kWh$_e$ (Li ion battery), 0.064 USD/kWh$_e$ (lead acid battery), and 0.32–0.36 USD/kWh$_e$ (vanadium redox flow battery). In this study, the LCOS is 0.92–2.37 USD/kWh$_e$ and higher than that of other energy storage methods. The reasons are 1) the power generation is small, 2) the operating temperature in the TCS is high, 3) the operating temperature of the ORC is low, 4) the power generation is only once in a day (i.e., in the evening) to respond to the rapid changes of net load, 5) stainless steel

is necessary for the material of some devices owing to high reaction temperature of $CaO/Ca(OH)_2$ (up to 600 °C), and 6) usage of alumina particles (70wt%) to promote fluidization causes increases of the material cost and the reactor volume. These lead to high LCOS. In the future, surplus power during daytime will greatly increase because solar power generation has been rapidly increasing. This leads to a decrease in the charging electricity cost, and it is expected that the cost is approaching free during daytime. The estimated total operating cost and LCOS under these conditions are summarized in Table 4.13. The results show that the operating cost and LCOS is 0.78–1.37 million USD and 0.60–1.35 USD/kWh_e, respectively. Thus, the operating cost and LCOS will decrease largely (operating cost: 41–52% reduction, LCOS: 30–43% reduction).

However, the process of this study has a potential of two times output per day (i.e., charging during daytime (mainly from PV) and discharging in the evening, and charging during nighttime (mainly from wind power) and discharging in the morning). If the power generation is two times in a day, LCOS can be decreased dramatically. Table 4.13 shows the estimated LCOS in the case of two times output in a day (no electricity cost during charging time). In these cases, LCOS decreases to 0.50–1.14 USD/kWh_e. However, the LCOS is still higher than the other energy storage method. For further reduction in LCOS, the author considers an increase of the operating temperature of the power generation cycle is effective for further reduction of LCOS of this TCS system.

Table 4.12 LCOS regarding only TCS system for cases 3, 9–16

Case	Fluidized bed volume [m^3]	$-\Delta Q_{H2}$ [%]	Capital cost, $C_{T,c}$ [million USD]	Operating cost, $C_{T,o}$ [million USD][*1]	LCOS [USD/kWh_e]
9	7	9.8	0.42	1.34	1.85
10	7	19.9	0.45	1.36	1.09
11	7	23.7	0.47	1.37	0.92
12	10	10.0	0.51	2.03	2.00
3	10	19.9	0.54	2.04	1.26
13	10	30.0	0.57	2.06	0.95
14	13	10.0	0.59	2.80	2.37
15	13	20.1	0.62	2.82	1.45
16	13	30.1	0.65	2.83	1.07

[*1]total operating cost in 20 years

Table 4.13 LCOS regarding only TCS system for cases 3, 9–16 (no electricity cost during charging time and two times output in a day)

Case	Operating cost, $C_{T,o}$ [million USD] [*1] (no electricity cost during charging time)	LCOS [USD/kWh_e] (no electricity cost during charging time)	LCOS [USD/kWh_e] (two times output in a day)
9	0.78	1.26	1.04
10	0.80	0.75	0.61
11	0.81	0.64	0.52
12	1.06	1.24	1.04
3	1.08	0.79	0.66
13	1.09	0.60	0.50
14	1.34	1.35	1.14
15	1.36	0.84	0.70
16	1.37	0.62	0.52

[*1]total operating cost in 20 years

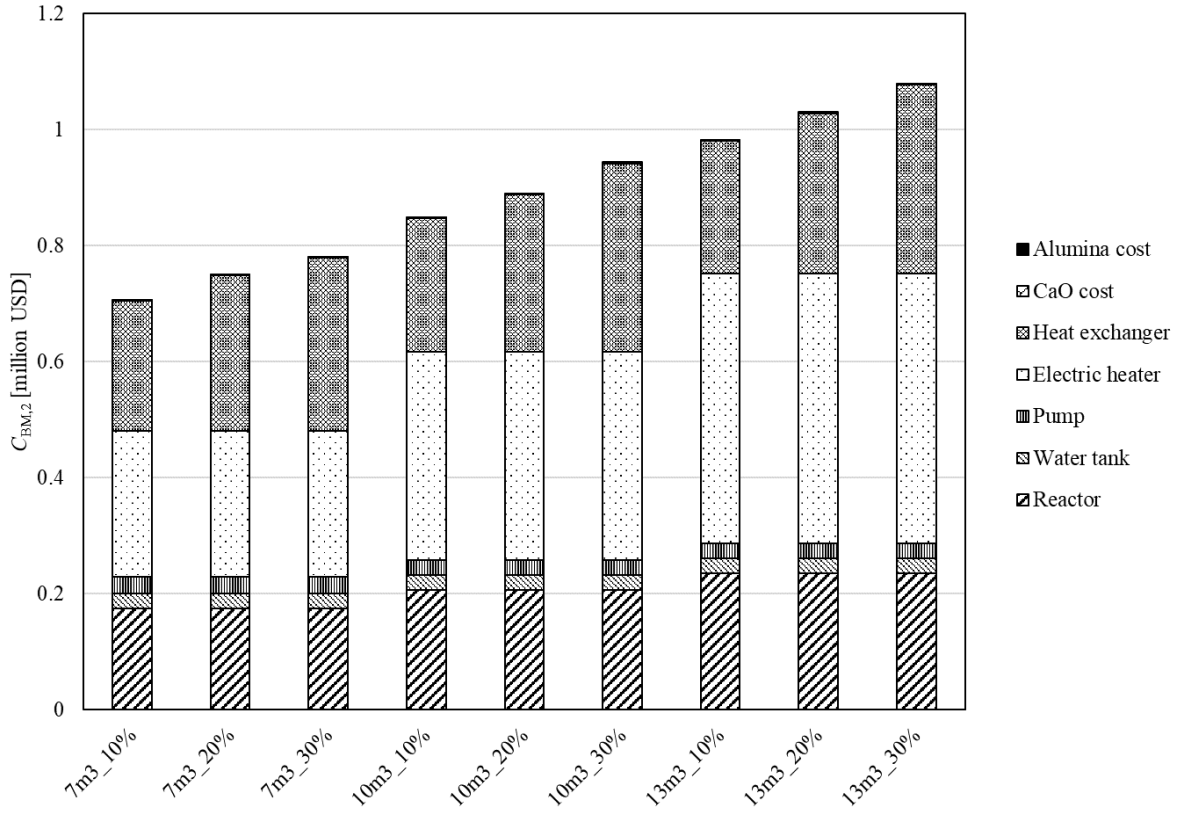

Figure 4.7 $C_{BM,2}$ of each equipment for cases 3, 9–16

4.4. Conclusions of Chapter 4

This chapter investigated the performances of the TCS system (a fluidized bed using $CaO/Ca(OH)_2$/alumina particles) integrated with the biomass power plant (ORC). The dynamic simulation by using a random function to simulate the fluctuating VRE as energy input to the fluidized bed reactor and power output by the turbine of the ORC was carried out. The following performances of the proposed TCS system and biomass power plant were investigated: First, the effects of ORC parameters and the fluidized bed volume on energy storage, second, the absorption of the VRE fluctuation by the proposed process in charging time, and third, the economics of the TCS system. The important results were summarized as follows.

(1) η_{energy} in the case of R1233zd (cases 3–5) was lower than that of R245fa (cases 0–2). However, the differences were small (< 0.1%). The decrease of H2 outlet temperature (cases 0–2 or 3–5) led to the increase of the heat recovery from the outlet steam from the TCS reactor, resulting in high $\eta_{storage}$ and η_{TCS}. On the other hand, η_{energy} decreased because H2 and C2 duty increased. As the superheat temperature was changed from 5 to 15 °C, $\eta_{storage}$ was higher, and η_{energy} was lower although those changes were small (< 0.5%). The lower biomass power plant scale and the larger fluidized bed volume lead to lower energy efficiencies.

(2) It was found that almost all of the VRE fluctuation can be absorbed by the TCS and ORC process. In the cases 21 and 22, the fluctuation behavior was the same for q_{heat}. However, the fluctuation behavior of cases 17–20 was opposite to q_{heat}. The reason was considered that the heat exchange amount was strongly influenced by the effects of the overall heat transfer coefficient in cases 17–20.

(3) In economics evaluations, LCOS of the TCS system were 0.92–2.37 USD/kWh_e. The total capital costs were 0.42–0.65 million USD, and the ratio was electric heater (H1) > heat

exchanger (HX1) > reactor > the others. The total operating costs were 1.34–2.83 million USD in 20 years. If the electricity cost will be free during daytime in the future, the operating costs and LCOS can be decreased dramatically (0.78–1.37 million USD and 0.60–1.35 USD/kWh$_e$, respectively). In addition, if power output is two times in a day, LCOS also decreases to 0.50–1.14 USD/kWh$_e$. However, the LCOS of the proposed process in this study is higher than that of other energy storage methods. The author consider an increase of the operating temperature of the power generation cycle is effective for further reduction of LCOS of this TCS system.

Chapter 5

Conclusions and Future Works

5.1. Conclusions

In this dissertation, the dynamic model of $CaO/Ca(OH)_2$ TCS system with a fluidized bed reactor and the TCS system integrated with a biomass power plant (ORC) were created. The energy efficiencies and LCOS of the proposed TCS system were investigated to store the surplus power generated from VRE and supply electricity at lower cost.

In Chapter 2, the dynamic model of a fluidized bed reactor was successfully created, and the absorption of the VRE fluctuation was evaluated. The model was developed by combining a CSTR model in the solid phase with a series of CSTRs in the gas phase for mass transport. The results show that the TCS efficiency (calculated by considering reaction heat) and energy storage efficiency (calculated by considering reaction heat and sensible heat) equaled 14.1% and 34.1% for steam and 29.9% and 62.7% for nitrogen, respectively. It was found that during dehydration, nitrogen was a suitable choice considering energy storage efficiencies, and steam was a suitable choice considering the usage of VRE as a heat resource.

In Chapter 3, the TCS system integrated with a biomass power plant was created. There are three operation modes; normal operation, charging, and discharging times. In normal operation, only ORC work. In charging time, the electricity from VRE is stored by using the TCS system, and the steam heat from the reactor is used as heat source of ORC. The turbine output is the same for that of normal operation. In discharging time, the stored energy is utilized as the heat source of ORC, and the turbine output increases to respond to the dramatic increase of net load. The results show that for the base case (fluidized bed reactor volume is 10 m^3, heat exchange area of HX1 is 67 m^2, and H2 load reduction is 20%), energy storage efficiency, TCS system efficiency, and round-trip efficiency were 58.5%, 61.0%, and 9.79%, respectively. It was found that flexible power generation is possible. The improved process was proposed, and energy storage efficiency was increased from 30.8% to 92.1% for the case of C-F2.

In Chapter 4, the process using R1233zd was evaluated. The effects of ORC

parameters and the fluidized bed volume on energy storage, the absorption of the VRE fluctuation by the proposed process in charging time, and the economics of the TCS system were evaluated. The results showed that η_{energy} in the case of R1233zd was lower than that of R245fa. However, the differences were small (< 0.1%). Thus, R1233zd was preferable to R245fa for ORC working fluid. It was found that almost all of the VRE fluctuation can be absorbed by the TCS and ORC process. In economics evaluations, LCOS of the TCS system were 0.92–2.37 USD/kWh$_e$. The ratio of the capital costs was electric heater (H1) > heat exchanger (HX1) > reactor > the others. If the electricity cost will be free during daytime in the future, the LCOS can be decreased dramatically (0.60–1.35 USD/kWh$_e$). In addition, if power output is two times in a day, LCOS also decreases to 0.50–1.14 USD/kWh$_e$.

It was found that the proposed TCS system has a potential of promoting VRE utilization because the system can absorb the VRE fluctuation. The integrated process can improve the performance of both the proposed TCS system and a biomass power plant. In addition, the integrated process can generate power flexibly. The integrated process was more improved by designing the recycle flow and/or changing the ORC working fluid (R245fa → R1233zd). The LCOS of the integrated process was higher than other energy storage methods. However, this integrated process has a potential (described in section 5.2). Above all, the proposed TCS system will contribute to the effective energy utilization, alleviation of the global warming, and leading to sustainable society.

5.2. Future Works

The proposed TCS system has potential for practical applications, and the improvement points are described in this section. For practical application, it is necessary that LCOS of TCS system become lower than that of other energy storage technologies such as batteries, hydrogen energy storage, etc. The future works for practical application of the TCS system are summarized from the view of material characteristics, reactor, and process, as shown in Figure 5.1. The main target is to improve performance and evaluate the process. First, regarding material characteristics, it is required to improve the heat transfer rate and material stability. Second, regarding reactor, the aim is to promote mass and heat transfer rate and propose more precise dynamic model for evaluating the intermittent operation. Third, the process integration (not only a biomass power plant) can alleviate the disadvantages of the proposed TCS system, and various process integration methodology should be proposed and evaluated. In addition, dynamic simulation and economics evaluation should be carried out for each proposed process. The power generation strategy should be determined based on power generation flexibility evaluated by accurate dynamic simulation. There are a lot of room for performance improvements, and the practical application in the near future are expected.

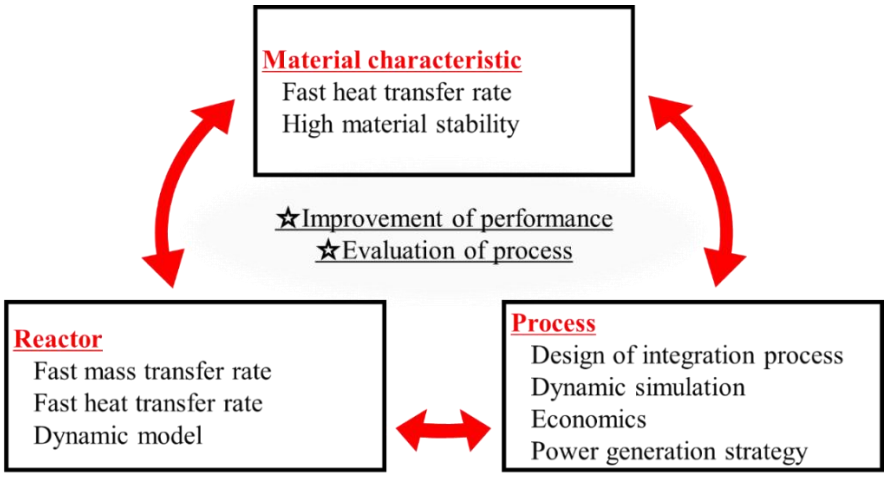

Figure 5.1 Future works for practical application of the TCS system

Nomenclature

A_B	m^2	cross-sectional area of the reactor
A_{HX1}	m^2	heat exchange area of HX1
B	-	coefficient for considering pressure and material
c	mol/m^3	gas concentration
c_p	kJ/kg/K, J/(mol·K)	specific heat capacity
C_p^0	USD	purchased cost for base conditions (ambient pressure and temperature, carbon steel)
C_{BM}	USD	bare module equipment cost
$C_{capital}$	USD	capital cost
$C_{T,c}$	USD	total capital cost
$C_{T,o}$	USD	total operating cost
D_B	M	internal diameter of the reactor (or the fluidized bed)
dX/dt	s^{-1}	reaction rate
dz	M	height of each cell
E_T	kWh_e	total power output discharged by the TCS system
F	mol/s	molar flow rate
F_{BM}	-	bare module cost factor
F_M	-	material factor
F_P	-	pressure factor
g	m/s^2	the gravitational acceleration
H_B	M	height of the fluidized bed
H_{in}	J	input energy into the whole process

$H_{\text{in,TCS}}$	J	input energy into the TCS system
H_{out}	J	output energy into the whole process (= turbine output)
i	-	number of a given individual cell
K	-	coefficient for C_{p}^{0} calculation
N	-	total number of cells
n	mol	molar weight
P_{cr}	kPa	critical pressure
p_{eq}	kPa	pressure at equilibrium
$p_{\text{onset,dehy}}$	bar	onset pressure for dehydration
$p_{\text{onset,hy}}$	bar	onset pressure for hydration
q	W	heat
q_{ave}	W	average of q_{heat}
$q_{\text{fluctuation}}$	W	magnitude of the VRE fluctuation
q_{heat}	W	$q_{\text{reactor}} + q_{\text{preheating}}$ (Chapter 2) or q_{reactor} (Chapters 3 and 4)
q_{min}	W	lowest value of q_{heat}
$q_{\text{preheating}}$	W	heat for preheating the fluidizing gas
q_{reactor}	W	heat supply into the reactor by electrical heaters
Q	J	integrated values of heat
Q_{chemical}	J	heat stored as thermochemical heat
Q_{heat}	J	integral value of q_{heat} from 0 to t_{finish}
Q_{reactor}	J	heat supply into the reactor by electrical heaters
Q_{recycled}	J	enthalpy of recycled stream 13 (see Figure 3.7)
$Q_{\text{s,finish}}$	J	sensible heat of the solid heated from ambient temperature to the final temperature at t_{finish}

$Q_{s,preheat}$	J	sensible heat of preheating solids from the ambient temperature to the initial temperature
$Q_{sensible}$	J	stored energy as sensible heat of the solid from 450 to 560 °C
$Q_{storage}$	J	stored energy
R	J/(mol·K)	the universal gas constant
r	-	discount factor
random	-	random number greater or equal to zero and less than one
t	S	time
t_c	min	charging time
t_{change}	S	interval time that the value of *random* was changed
t_d	min	discharging time
t_{finish}	S	time of reaction completion
T	K	temperature
T_{cr}	K	critical temperature
T_{eq}	K	temperature at equilibrium
U	W/(m^2·K)	coefficient of overall heat transfer between the wall and the bed
v_g	-	voidage
W	J	integrated values of work
w	W	work
X	%, -	conversion ratio
Z	m^2, m^3, kW	equipment cost attribute
ΔH_r	kJ/mol	reaction enthalpy

ΔQ_{H2}	%, J	decrease of the heat duty in H2 (i.e. the saving of the biomass usage)
Δq_{total}	W	summation of the absolute of the differences of q_{heat}
ΔT_{total}	K	summation of the absolute bed temperature changes
Δw_{total}	W	summation of the absolute of the differences of w_{T2}
$\eta_{chemical}$	%	TCS efficiency
η_{energy}	%	round-trip efficiency
$\eta_{storage}$	%	energy storage efficiency
η_{TCS}	%	TCS system efficiency

Subscripts

B	fluidized bed
c	charging time
d	discharging time
e	electricity
eq	equilibrium
g	gas
n	normal operation time
th	thermal

Abbreviations

ASHRAE	American society of heating, refrigerating and air-conditioning engineers
CEPCI	the chemical engineering plant cost index
CSP	concentrated solar power
CSTR	continuously stirred tank reactor
EES	electric energy storage
GWP	global warming potential
LCOE	levelized cost of electricity
LCOS	levelized cost of storage
NBP	normal boiling point
NIST	national institute of standards and technology
ODP	ozone depletion potential
OECD	organization for economic co-operation and development
ORC	organic Rankine cycle
PCM	phase change material
PV	photovoltaics
TCS	thermochemical heat storage
TES	thermal energy storage
USD	United States dollar
VRE	variable renewable energy

Reference List

[1] BP stastical Review of World Energy June 2022. Britich Pet, https://www.bp.com/en/global/corporate/energy-economics/statistical-review-of-world-energy.html (accessed July 25, 2022).

[2] World Population Prospects 2019. United Nations, https://population.un.org/wpp/Download/Standard/Population/ (accessed July 6, 2022).

[3] renewable energy. United Nations, https://www.un.org/en/climatechange/what-is-renewable-energy (accessed July 7, 2022).

[4] Lamsal D, Sreeram V, Mishra Y, Kumar D. Output power smoothing control approaches for wind and photovoltaic generation systems: A review. Renew Sustain Energy Rev 2019;113:109245. https://doi.org/10.1016/j.rser.2019.109245.

[5] The relation between solar power generation and the season and climate. ENECHANGE Ltd, https://enechange.jp/articles/solar-season (accessed July 30, 2022).

[6] IEA_System Integration of Renewables -An update on Best Practice (Japanese version). New Energy Ind Technol Dev Organ, https://www.nedo.go.jp/library/system_integration_of_renewables.html (accessed July 16, 2022).

[7] Guidelines for Power Transmission and Distribution. Organization for Cross-regional Coordination of Transmission Operators, Japan, https://www.occto.or.jp/article/ (accessed July 8, 2022).

[8] Schoenung SM, Keller JO. Commercial potential for renewable hydrogen in California. Int J Hydrogen Energy 2017;42:13321–8. https://doi.org/10.1016/j.ijhydene.2017.01.005.

[9] Salas D, Tapachès E, Mazet N, Aussel D. Economical optimization of thermochemical storage in concentrated solar power plants via pre-scenarios. Energy Convers Manag 2018;174:932–54. https://doi.org/10.1016/j.enconman.2018.08.079.

[10] Tapachès E, Salas D, Perier-Muzet M, Mauran S, Aussel D, Mazet N. The value of thermochemical storage for concentrated solar power plants: Economic and technical conditions of power plants profitability on spot markets. Energy Convers Manag 2019;198:111078. https://doi.org/10.1016/j.enconman.2018.11.082.

[11] Spot Market. Japan Electr Power Exch, http://www.jepx.org/market/index.html (accessed February 2, 2022).

[12] Supply and demand data by the area. TEPCO Power Grid, Inc, https://www.tepco.co.jp/forecast/html/area_data-j.html (accessed February 7, 2022).

[13] Wu S, Zhou C, Doroodchi E, Nellore R, Moghtaderi B. A review on high-temperature thermochemical energy storage based on metal oxides redox cycle. Energy Convers Manag 2018;168:421–53. https://doi.org/10.1016/j.enconman.2018.05.017.

[14] Energy storage Technology. National Institute for Environmental Studies,https://tenbou.nies.go.jp/science/description/detail.php?id=100 (accessed July 7, 2022).

[15] Aneke M, Wang M. Energy storage technologies and real life applications – A state of the art review. Appl Energy 2016;179:350–77. https://doi.org/10.1016/j.apenergy.2016.06.097.

[16] Carnot batteries. Energy Consevation through Energy Storage, https://iea-es.org/annex-36/ (accessed May 7, 2022).

[17] Krese G, Koželj R, Butala V, Stritih U. Thermochemical seasonal solar energy storage for heating and cooling of buildings. Energy Build 2018;164:239–53. https://doi.org/10.1016/j.enbuild.2017.12.057.

[18] Afflerbach S, Trettin R. A systematic screening approach for new materials for

thermochemical energy storage and conversion based on the Strunz mineral classification system. Thermochim Acta 2019;674:82–94. https://doi.org/10.1016/j.tca.2019.02.010.

[19] Richter M, Habermann EM, Siebecke E, Linder M. A systematic screening of salt hydrates as materials for a thermochemical heat transformer. Thermochim Acta 2018;659:136–50. https://doi.org/10.1016/j.tca.2017.06.011.

[20] Alva G, Lin Y, Fang G. An overview of thermal energy storage systems. Energy 2018;144:341–78. https://doi.org/10.1016/j.energy.2017.12.037.

[21] Khosa AA, Xu T, Xia BQ, Yan J, Zhao CY. Technological challenges and industrial applications of $CaCO_3$/CaO based thermal energy storage system – A review. Sol Energy 2019;193:618–36. https://doi.org/10.1016/j.solener.2019.10.003.

[22] Nazir H, Batool M, Bolivar Osorio FJ, Isaza-Ruiz M, Xu X, Vignarooban K, et al. Recent developments in phase change materials for energy storage applications: A review. Int J Heat Mass Transf 2019;129:491–523. https://doi.org/10.1016/j.ijheatmasstransfer.2018.09.126.

[23] Pelay U, Luo L, Fan Y, Stitou D, Rood M. Thermal energy storage systems for concentrated solar power plants. Renew Sustain Energy Rev 2017;79:82–100. https://doi.org/10.1016/j.rser.2017.03.139.

[24] Yan T, Wang RZ, Li TX, Wang LW, Fred IT. A review of promising candidate reactions for chemical heat storage. Renew Sustain Energy Rev 2015;43:13–31. https://doi.org/10.1016/j.rser.2014.11.015.

[25] Dizaji HB, Hosseini H. A review of material screening in pure and mixed-metal oxide thermochemical energy storage (TCES) systems for concentrated solar power (CSP) applications. Renew Sustain Energy Rev 2018;98:9–26. https://doi.org/10.1016/j.rser.2018.09.004.

[26] Sunku Prasad J, Muthukumar P, Desai F, Basu DN, Rahman MM. A critical review of

high-temperature reversible thermochemical energy storage systems. Appl Energy 2019;254:113733. https://doi.org/10.1016/j.apenergy.2019.113733.

[27] Deutsch M, Müller D, Aumeyr C, Jordan C, Gierl-Mayer C, Weinberger P, et al. Systematic search algorithm for potential thermochemical energy storage systems. Appl Energy 2016;183:113–20. https://doi.org/10.1016/j.apenergy.2016.08.142.

[28] Schaube F, Koch L, Wörner A, Müller-Steinhagen H. A thermodynamic and kinetic study of the de- and rehydration of $Ca(OH)_2$ at high H_2O partial pressures for thermo-chemical heat storage. Thermochim Acta 2012;538:9–20. https://doi.org/10.1016/j.tca.2012.03.003.

[29] Pardo P, Anxionnaz-Minvielle Z, Rougé S, Cognet P, Cabassud M. $Ca(OH)_2$/CaO reversible reaction in a fluidized bed reactor for thermochemical heat storage. Sol Energy 2014;107:605–16. https://doi.org/10.1016/j.solener.2014.06.010.

[30] Farcot L, Le Pierrès N, Michel B, Fourmigué JF, Papillon P. Numerical investigations of a continuous thermochemical heat storage reactor. J Energy Storage 2018;20:109–19. https://doi.org/10.1016/j.est.2018.08.020.

[31] André L, Abanades S, Flamant G. Screening of thermochemical systems based on solid-gas reversible reactions for high temperature solar thermal energy storage. Renew Sustain Energy Rev 2016;64:703–15. https://doi.org/10.1016/j.rser.2016.06.043.

[32] Pan ZH, Zhao CY. Gas–solid thermochemical heat storage reactors for high-temperature applications. Energy 2017;130:155–73. https://doi.org/10.1016/j.energy.2017.04.102.

[33] Criado YA, Alonso M, Abanades JC, Anxionnaz-Minvielle Z. Conceptual process design of a CaO/$Ca(OH)_2$ thermochemical energy storage system using fluidized bed reactors. Appl Therm Eng 2014;73:1087–94. https://doi.org/10.1016/j.applthermaleng.2014.08.065.

[34] Matsuda H, Ishizu T, Lee SK, Hasatani M. Kinetic Study of $Ca(OH)_2$/CaO Reversible Thermochemical Reaction for Thermal Energy Storage by Means of Chemical Reaction. Kagaku Kogaku Ronbunshu 1985;11:542–548. https://doi.org/10.1252/kakoronbunshu.11.542.

[35] Angerer M, Becker M, Härzschel S, Kröper K, Gleis S, Vandersickel A, et al. Design of a MW-scale thermo-chemical energy storage reactor. Energy Reports 2018;4:507–19. https://doi.org/10.1016/j.egyr.2018.07.005.

[36] Zhang H, Ogura H. Studies on hydration reaction rates of various size CaO particles for chemical heat storage/pump. J Chem Eng Japan 2014;47:587–94. https://doi.org/10.1252/jcej.13we297.

[37] Abliz S, Fujioka O, Ogura H, Kage H. Reaction activity of CaO particles prepared by calcination of some $CaCO_3$ materials. J Chem Eng Japan 2004;37:815–21. https://doi.org/10.1252/jcej.37.815.

[38] Yan J, Zhao CY, Xia BQ, Wang T. The effect of dehydration temperatures on the performance of the CaO/$Ca(OH)_2$ thermochemical heat storage system. Energy 2019;186:115837. https://doi.org/10.1016/j.energy.2019.07.167.

[39] Kito T, Kobayashi N. Evaluation of output power characteristics of chemical heat pump by using CaO-LiCl compound reactant. Kagaku Kogaku Ronbunshu 2012;38:172–5. https://doi.org/10.1252/kakoronbunshu.38.172.

[40] Shkatulov A, Aristov Y. Modification of magnesium and calcium hydroxides with salts: An efficient way to advanced materials for storage of middle-temperature heat. Energy 2015;85:667–76. https://doi.org/10.1016/j.energy.2015.04.004.

[41] Yan J, Zhao CY. Thermodynamic and kinetic study of the dehydration process of CaO/$Ca(OH)_2$ thermochemical heat storage system with Li doping. Chem Eng Sci 2015;138:86–92. https://doi.org/10.1016/j.ces.2015.07.053.

[42] Maruyama A, Kurosawa R, Ryu J. Effect of Lithium Compound Addition on the

Dehydration and Hydration of Calcium Hydroxide as a Chemical Heat Storage Material. ACS Omega 2020. https://doi.org/10.1021/acsomega.9b04444.

[43] Yan J, Zhao CY. First-principle study of $CaO/Ca(OH)_2$ thermochemical energy storage system by Li or Mg cation doping. Chem Eng Sci 2014;117:293–300. https://doi.org/10.1016/j.ces.2014.07.007.

[44] Kariya J, Ryu J, Kato Y. Reaction performance of calcium hydroxide and expanded graphite composites for chemical heat storage applications. ISIJ Int 2015;55:457–63. https://doi.org/10.2355/isijinternational.55.457.

[45] Kariya J, Kato Y. Development of thermal energy storage material using porous silicon carbide and calcium hydroxide. Energy Procedia 2017;131:395–406. https://doi.org/10.1016/j.egypro.2017.09.470.

[46] Schmidt M, Linder M. Power generation based on the $Ca(OH)_2/CaO$ thermochemical storage system – Experimental investigation of discharge operation modes in lab scale and corresponding conceptual process design. Appl Energy 2017;203:594–607. https://doi.org/10.1016/j.apenergy.2017.06.063.

[47] Roßkopf C, Haas M, Faik A, Linder M, Wörner A. Improving powder bed properties for thermochemical storage by adding nanoparticles. Energy Convers Manag 2014;86:93–8. https://doi.org/10.1016/j.enconman.2014.05.017.

[48] Roßkopf C, Afflerbach S, Schmidt M, Görtz B, Kowald T, Linder M, et al. Investigations of nano coated calcium hydroxide cycled in a thermochemical heat storage. Energy Convers Manag 2015;97:94–102. https://doi.org/10.1016/j.enconman.2015.03.034.

[49] Xia BQ, Zhao CY, Yan J, Khosa AA. Development of granular thermochemical heat storage composite based on calcium oxide. Renew Energy 2020;147:969–78. https://doi.org/10.1016/j.renene.2019.09.065.

[50] Afflerbach S, Kappes M, Gipperich A, Trettin R, Krumm W. Semipermeable

encapsulation of calcium hydroxide for thermochemical heat storage solutions. Sol Energy 2017;148:1–11. https://doi.org/10.1016/j.solener.2017.03.074.

[51] Darkwa K. Thermochemical energy storage in inorganic oxides: An experimental evaluation. Appl Therm Eng 1998;18:387–400. https://doi.org/10.1016/S1359-4311(97)00052-5.

[52] Galwey AK, Laverty GM. A kinetic and mechanistic study of the dehydroxylation of calcium hydroxide. Thermochim Acta 1993;228:359–78. https://doi.org/10.1016/0040-6031(93)80304-S.

[53] L'vov B V., Ugolkov VL. Kinetics and mechanism of free-surface decomposition of Group IIA and IIB hydroxides analyzed thermogravimetrically by the third-law method. Thermochim Acta 2004;413:7–15. https://doi.org/10.1016/j.tca.2003.11.008.

[54] Azpiazu MN, Morquillas JM, Vazquez A. Heat recovery from a thermal energy storage based on the $Ca(OH)_2$/CaO cycle. Appl Therm Eng 2003;23:733–41. https://doi.org/10.1016/S1359-4311(03)00015-2.

[55] Matsuda H, Ishizu T, Lee SK, Hasatani M. Kinetic study of $Ca(OH)_2$/CaO reversible thermochemical reaction for thermal energy storage by means of chemical reaction. Kagaku Kogaku Roubunshu 1985; 11:542–8. https://doi.org/10.1252/kakoronbunshu.11.542.

[56] Abliz S, Ogura H, Kage H, Matsuno Y. Kinetic Study of CaO/$Ca(OH)_2$ Reversible Chemical Reaction in Vacuumed Forced Convection for Thermal Energy Storage. Kagaku Kogaku Ronbunshu 2002;28:345–9. https://doi.org/10.1252/kakoronbunshu.28.345.

[57] Abliz S, Ogura H, Kage H. Final conversion and reaction rate of CaO hydration in different experimental systems. Kagaku Kogaku Ronbunshu 2005;31:253–8. https://doi.org/10.1252/kakoronbunshu.31.253.

[58] Nagel T, Shao H, Roßkopf C, Linder M, Wörner A, Kolditz O. The influence of gas-

solid reaction kinetics in models of thermochemical heat storage under monotonic and cyclic loading. Appl Energy 2014;136:289–302. https://doi.org/10.1016/j.apenergy.2014.08.104.

[59] Yuan Y, Li Y, Duan L, Liu H, Zhao J, Wang Z. $CaO/Ca(OH)_2$ thermochemical heat storage of carbide slag from calcium looping cycles for CO_2 capture. Energy Convers Manag 2018;174:8–19. https://doi.org/10.1016/j.enconman.2018.08.021.

[60] Yan J, Zhao CY. Thermodynamic and kinetic study of the dehydration process of $CaO/Ca(OH)_2$ thermochemical heat storage system with Li doping. Chem Eng Sci 2015;138:86–92. https://doi.org/10.1016/j.ces.2015.07.053.

[61] Yan J, Zhao CY. Experimental study of $CaO/Ca(OH)_2$ in a fixed-bed reactor for thermochemical heat storage. Appl Energy 2016;175:277–84. https://doi.org/10.1016/j.apenergy.2016.05.038.

[62] Pan Z, Zhao C. Prediction of the effective thermal conductivity of packed bed with micro-particles for thermochemical heat storage. Sci Bull 2017;62:256–65. https://doi.org/10.1016/j.scib.2016.12.009.

[63] Yan J, Zhao CY, Pan ZH. The effect of CO_2 on $Ca(OH)_2$ and $Mg(OH)_2$ thermochemical heat storage systems. Energy 2017;124:114–23. https://doi.org/10.1016/j.energy.2017.02.034.

[64] Criado YA, Alonso M, Abanades JC. Enhancement of a $CaO/Ca(OH)_2$ based material for thermochemical energy storage. Sol Energy 2016;135:800–9. https://doi.org/10.1016/j.solener.2016.06.056.

[65] Watanabe F, Tsumagari S, Huang H, Hasatani M, Kobayashi N, Tsubouchi O, et al. Performance evaluation of carbonaseous porous solid supported $Ca(OH)_2$ chemical heat storage material. Kagaku Kogaku Ronbunshu 2013;39:378–83. https://doi.org/10.1252/kakoronbunshu.39.378.

[66] Sakellariou KG, Karagiannakis G, Criado YA, Konstandopoulos AG. Calcium oxide

based materials for thermochemical heat storage in concentrated solar power plants. Sol Energy 2015;122:215–30. https://doi.org/10.1016/j.solener.2015.08.011.

[67] Sakellariou KG, Criado YA, Tsongidis NI, Karagiannakis G, Konstandopoulos AG. Multi-cyclic evaluation of composite CaO-based structured bodies for thermochemical heat storage via the CaO/$Ca(OH)_2$ reaction scheme. Sol Energy 2017;146:65–78. https://doi.org/10.1016/j.solener.2017.02.013.

[68] Benitez-Guerrero M, Valverde JM, Perejon A, Sanchez-Jimenez PE, Perez-Maqueda LA. Low-cost Ca-based composites synthesized by biotemplate method for thermochemical energy storage of concentrated solar power. Appl Energy 2018;210:108–16. https://doi.org/10.1016/j.apenergy.2017.10.109.

[69] Sun H, Li Y, Bian Z, Yan X, Wang Z, Liu W. Thermochemical energy storage performances of Ca-based natural and waste materials under high pressure during CaO/$CaCO_3$ cycles. Energy Convers Manag 2019;197:111885. https://doi.org/10.1016/j.enconman.2019.111885.

[70] Benitez-Guerrero M, Sarrion B, Perejon A, Sanchez-Jimenez PE, Perez-Maqueda LA, Manuel Valverde J. Large-scale high-temperature solar energy storage using natural minerals. Sol Energy Mater Sol Cells 2017;168:14–21. https://doi.org/10.1016/j.solmat.2017.04.013.

[71] Fedunik-Hofman L, Bayon A, Hinkley J, Lipiński W, Donne SW. Friedman method kinetic analysis of CaO-based sorbent for high-temperature thermochemical energy storage. Chem Eng Sci 2019;200:236–47. https://doi.org/10.1016/j.ces.2019.02.003.

[72] Sarrión B, Perejón A, Sánchez-Jiménez PE, Pérez-Maqueda LA, Valverde JM. Role of calcium looping conditions on the performance of natural and synthetic Ca-based materials for energy storage. J CO2 Util 2018;28:374–84. https://doi.org/10.1016/j.jcou.2018.10.018.

[73] Lu S, Wu S. Calcination-carbonation durability of nano $CaCO_3$ doped with Li_2SO_4.

Chem Eng J 2016;294:22–9. https://doi.org/10.1016/j.cej.2016.02.100.

[74] Kumar D, Maiti SC, Ghoroi C. Decomposition kinetics of $CaCO_3$ dry coated with nano-silica. Thermochim Acta 2016;624:35–46. https://doi.org/10.1016/j.tca.2015.11.019.

[75] Valverde JM, Sanchez-Jimenez PE, Perejon A, Perez-Maqueda LA. Constant rate thermal analysis for enhancing the long-term CO_2 capture of CaO at Ca-looping conditions. Appl Energy 2013;108:108–20. https://doi.org/10.1016/j.apenergy.2013.03.013.

[76] Khosa AA, Zhao CY. Heat storage and release performance analysis of $CaCO_3$/CaO thermal energy storage system after doping nano silica. Sol Energy 2019;188:619–30. https://doi.org/10.1016/j.solener.2019.06.048.

[77] Pontiga F, Valverde JM, Moreno H, Duran-Olivencia FJ. Dry gas-solid carbonation in fluidized beds of $Ca(OH)_2$ and nanosilica/$Ca(OH)_2$ at ambient temperature and low CO_2 pressure. Chem Eng J 2013;222:546–52. https://doi.org/10.1016/j.cej.2013.02.067.

[78] Chen H, Zhang P, Duan Y, Zhao C. Reactivity enhancement of calcium based sorbents by doped with metal oxides through the sol-gel process. Appl Energy 2016;162:390–400. https://doi.org/10.1016/j.apenergy.2015.10.035.

[79] Da Y, Xuan Y, Teng L, Zhang K, Liu X, Ding Y. Calcium-based composites for direct solar-thermal conversion and thermochemical energy storage. Chem Eng J 2020;382:122815. https://doi.org/10.1016/j.cej.2019.122815.

[80] Yanase I, Maeda T, Kobayashi H. The effect of addition of a large amount of CeO_2 on the CO_2 adsorption properties of CaO powder. Chem Eng J 2017;327:548–54. https://doi.org/10.1016/j.cej.2017.06.140.

[81] Shui M, Yue L, Hua Y, Xu Z. The decomposition kinetics of the SiO_2 coated nano-scale calcium carbonate. Thermochim Acta 2002;386:43–9.

https://doi.org/10.1016/S0040-6031(01)00723-7.

[82] Chen X, Jin X, Liu Z, Ling X, Wang Y. Experimental investigation on the CaO/CaCO3 thermochemical energy storage with SiO_2 doping. Energy 2018;155:128–38. https://doi.org/10.1016/j.energy.2018.05.016.

[83] Jin D, Yu X, Yue L, Wang L. Decomposition kinetics study of AlOOH coated calcium carbonate. Mater Chem Phys 2009;115:418–22. https://doi.org/10.1016/j.matchemphys.2008.12.013.

[84] Benitez-Guerrero M, Valverde JM, Sanchez-Jimenez PE, Perejon A, Perez-Maqueda LA. Calcium-Looping performance of mechanically modified Al_2O_3-CaO composites for energy storage and CO_2 capture. Chem Eng J 2018;334:2343–55. https://doi.org/10.1016/j.cej.2017.11.183.

[85] Jing J ying, Li T yu, Zhang X wei, Wang S dong, Feng J, Turmel WA, et al. Enhanced CO_2 sorption performance of CaO/$Ca_3Al_2O_6$ sorbents and its sintering-resistance mechanism. Appl Energy 2017;199:225–33. https://doi.org/10.1016/j.apenergy.2017.03.131.

[86] Obermeier J, Sakellariou KG, Tsongidis NI, Baciu D, Charalambopoulou G, Steriotis T, et al. Material development and assessment of an energy storage concept based on the CaO-looping process. Sol Energy 2017;150:298–309. https://doi.org/10.1016/j.solener.2017.04.058.

[87] Gao F, Huang J, Sun H, Hu J, Wang M, Mi J, et al. CO_2 capture using mesocellular siliceous foam (MCF)-supported CaO. J Energy Inst 2019;92:1591–8. https://doi.org/10.1016/j.joei.2018.07.015.

[88] Han R, Gao J, Wei S, Su Y, Sun F, Zhao G, et al. Strongly coupled calcium carbonate/antioxidative graphite nanosheets composites with high cycling stability for thermochemical energy storage. Appl Energy 2018;231:412–22. https://doi.org/10.1016/j.apenergy.2018.09.142.

[89] Han R, Gao J, Wei S, Su Y, Su C, Li J, et al. High-performance CaO-based composites synthesized using a space-confined chemical vapor deposition strategy for thermochemical energy storage. Sol Energy Mater Sol Cells 2020;206. https://doi.org/10.1016/j.solmat.2019.110346.

[90] Sánchez Jiménez PE, Perejón A, Benítez Guerrero M, Valverde JM, Ortiz C, Pérez Maqueda LA. High-performance and low-cost macroporous calcium oxide based materials for thermochemical energy storage in concentrated solar power plants. Appl Energy 2019;235:543–52. https://doi.org/10.1016/j.apenergy.2018.10.131.

[91] Shkatulov AI, Kim ST, Miura H, Kato Y, Aristov YI. Adapting the MgO-CO_2 working pair for thermochemical energy storage by doping with salts. Energy Convers Manag 2019;185:473–81. https://doi.org/10.1016/j.enconman.2019.01.056.

[92] Bagherisereshki E, Tran J, Lei F, AuYeung N. Investigation into SrO/$SrCO_3$ for high temperature thermochemical energy storage. Sol Energy 2018;160:85–93. https://doi.org/10.1016/j.solener.2017.11.073.

[93] Müller D, Knoll C, Gravogl G, Artner W, Welch JM, Eitenberger E, et al. Tuning the performance of MgO for thermochemical energy storage by dehydration – From fundamentals to phase impurities. Appl Energy 2019;253:113562. https://doi.org/10.1016/j.apenergy.2019.113562.

[94] Kurosawa R, Ryu J. Effect of LiOH addition on dehydration reaction of $Mg(OH)_2$. J Chem Eng Japan 2019;52:152–8. https://doi.org/10.1252/jcej.18we010.

[95] Shkatulov A, Takasu H, Kato Y, Aristov Y. Thermochemical energy storage by $LiNO_3$ -doped $Mg(OH)_2$: Rehydration study. J Energy Storage 2019;22:302–10. https://doi.org/10.1016/j.est.2019.01.014.

[96] Myagmarjav O, Ryu J, Kato Y. Dehydration kinetic study of a chemical heat storage material with lithium bromide for a magnesium oxide/water chemical heat pump. Prog Nucl Energy 2015;82:153–8. https://doi.org/10.1016/j.pnucene.2014.07.026.

[97] Mastronardo E, Bonaccorsi L, Kato Y, Piperopoulos E, Lanza M, Milone C. Strategies for the enhancement of heat storage materials performances for $MgO/H_2O/Mg(OH)_2$ thermochemical storage system. Appl Therm Eng 2017;120:626–34. https://doi.org/10.1016/j.applthermaleng.2017.04.004.

[98] Piperopoulos E, Mastronardo E, Fazio M, Lanza M, Galvagno S, Milone C. Synthetic strategies for the enhancement of $Mg(OH)_2$ thermochemical performances as heat storage material. Energy Procedia 2018;155:269–79. https://doi.org/10.1016/j.egypro.2018.11.051.

[99] Mastronardo E, Bonaccorsi L, Kato Y, Piperopoulos E, Milone C. Efficiency improvement of heat storage materials for $MgO/H_2O/Mg(OH)_2$ chemical heat pumps. Appl Energy 2016;162:31–9. https://doi.org/10.1016/j.apenergy.2015.10.066.

[100] Tescari S, Agrafiotis C, Breuer S, De Oliveira L, Neises-Von Puttkamer M, Roeb M, et al. Thermochemical solar energy storage via redox oxides: Materials and reactor/heat exchanger concepts. Energy Procedia 2014;49:1034–43. https://doi.org/10.1016/j.egypro.2014.03.111.

[101] Wyttenbach J, Bougard J, Descy G, Skrylnyk O, Courbon E, Frère M, et al. Performances and modelling of a circular moving bed thermochemical reactor for seasonal storage. Appl Energy 2018;230:803–15. https://doi.org/10.1016/j.apenergy.2018.09.008.

[102] Cammarata A, Verda V, Sciacovelli A, Ding Y. Hybrid strontium bromide-natural graphite composites for low to medium temperature thermochemical energy storage: Formulation, fabrication and performance investigation. Energy Convers Manag 2018;166:233–40. https://doi.org/10.1016/j.enconman.2018.04.031.

[103] Gaeini M, Rouws AL, Salari JWO, Zondag HA, Rindt CCM. Characterization of microencapsulated and impregnated porous host materials based on calcium chloride for thermochemical energy storage. Appl Energy 2018;212:1165–77.

https://doi.org/10.1016/j.apenergy.2017.12.131.

[104] Schmidt M, Szczukowski C, Roßkopf C, Linder M, Wörner A. Experimental results of a 10 kW high temperature thermochemical storage reactor based on calcium hydroxide. Appl Therm Eng 2014;62:553–9. https://doi.org/10.1016/j.applthermaleng.2013.09.020.

[105] Linder M, Roßkopf C, Schmidt M, Wörner A. Thermochemical energy storage in kW-scale based on CaO/$Ca(OH)_2$. Energy Procedia 2014;49:888–97. https://doi.org/10.1016/j.egypro.2014.03.096.

[106] Schmidt M, Gutierrez A, Linder M. Thermochemical energy storage with CaO/$Ca(OH)_2$– Experimental investigation of the thermal capability at low vapor pressures in a lab scale reactor. Appl Energy 2017;188:672–81. https://doi.org/10.1016/j.apenergy.2016.11.023.

[107] Wang M, Chen L, He P, Tao WQ. Numerical study and enhancement of $Ca(OH)_2$/CaO dehydration process with porous channels embedded in reactors. Energy 2019;181:417–28. https://doi.org/10.1016/j.energy.2019.05.184.

[108] Schaube F, Kohzer A, Schütz J, Wörner A, Müller-Steinhagen H. De- and rehydration of $Ca(OH)_2$ in a reactor with direct heat transfer for thermo-chemical heat storage. Part A: Experimental results. Chem Eng Res Des 2013;91:856–864. https://doi.org/10.1016/j.cherd.2013.02.019.

[109] Dai L, Long XF, Lou B, Wu J. Thermal cycling stability of thermochemical energy storage system $Ca(OH)_2$/CaO. Appl Therm Eng 2018;133:261–8. https://doi.org/10.1016/j.applthermaleng.2018.01.059.

[110] Nagel T, Shao H, Singh AK, Watanabe N, Roßkopf C, Linder M, et al. Non-equilibrium thermochemical heat storage in porous media: Part 1 - Conceptual model. Energy 2013;60:254–70. https://doi.org/10.1016/j.energy.2013.06.025.

[111] Shao H, Nagel T, Roßkopf C, Linder M, Wörner A, Kolditz O. Non-equilibrium

thermo-chemical heat storage in porous media: Part 2 - A 1D computational model for a calcium hydroxide reaction system. Energy 2013;60:271–82. https://doi.org/10.1016/j.energy.2013.07.063.

[112] Ströhle S, Haselbacher A, Jovanovic ZR, Steinfeld A. Transient discrete-granule packed-bed reactor model for thermochemical energy storage. Chem Eng Sci 2014;117:465–78. https://doi.org/10.1016/j.ces.2014.07.009.

[113] Wang W, Kolditz O, Nagel T. Parallel finite element modelling of multi-physical processes in thermochemical energy storage devices. Appl Energy 2017;185:1954–64. https://doi.org/10.1016/j.apenergy.2016.03.053.

[114] Ranjha Q, Oztekin A. Numerical analyses of three-dimensional fixed reaction bed for thermochemical energy storage. Renew Energy 2017;111:825–35. https://doi.org/10.1016/j.renene.2017.04.062.

[115] Cosquillo Mejia A, Afflerbach S, Linder M, Schmidt M. Experimental analysis of encapsulated CaO/$Ca(OH)_2$ granules as thermochemical storage in a novel moving bed reactor. Appl Therm Eng 2020;169:114961. https://doi.org/10.1016/j.applthermaleng.2020.114961.

[116] Muchi I, Horio M, Mori S. Reaction Engineering of Fluidized Bed. Baihukan; 1984.

[117] Criado YA, Huille A, Rougé S, Abanades JC. Experimental investigation and model validation of a CaO/$Ca(OH)_2$ fluidized bed reactor for thermochemical energy storage applications. Chem Eng J 2017;313:1194–205. https://doi.org/10.1016/j.cej.2016.11.010.

[118] Flegkas S, Birkelbach F, Winter F, Freiberger N, Werner A. Fluidized bed reactors for solid-gas thermochemical energy storage concepts - Modelling and process limitations. Energy 2018;143:615–23. https://doi.org/10.1016/j.energy.2017.11.065.

[119] Levenspiel O. Chemical Reaction Engineering. John Wiley & Sons; 1998.

[120] Wang H, Li Z, Li Y, Cai N. Reduced-order model for CaO carbonation kinetics

measured using micro-fluidized bed thermogravimetric analysis. Chem Eng Sci 2021;229. https://doi.org/10.1016/j.ces.2020.116039.

[121] Tescari S, Singh A, Agrafiotis C, de Oliveira L, Breuer S, Schlögl-Knothe B, et al. Experimental evaluation of a pilot-scale thermochemical storage system for a concentrated solar power plant. Appl Energy 2017;189:66–75. https://doi.org/10.1016/j.apenergy.2016.12.032.

[122] Michel B, Mazet N, Neveu P. Experimental investigation of an open thermochemical process operating with a hydrate salt for thermal storage of solar energy: Local reactive bed evolution. Appl Energy 2016;180:234–44. https://doi.org/10.1016/j.apenergy.2016.07.108.

[123] De Jong AJ, Van Vliet L, Hoegaerts C, Roelands M, Cuypers R. Thermochemical Heat Storage - From Reaction Storage Density to System Storage Density. Energy Procedia 2016;91:128–37. https://doi.org/10.1016/j.egypro.2016.06.187.

[124] Pan ZH, Yan J, Zhao CY. Numerical analyses and optimization of tubular thermochemical heat storage reactors using axisymmetric thermal lattice Boltzmann model. Chem Eng Sci 2019;195:737–47. https://doi.org/10.1016/j.ces.2018.10.019.

[125] Lutz M, Bhouri M, Linder M, Bürger I. Adiabatic magnesium hydride system for hydrogen storage based on thermochemical heat storage: Numerical analysis of the dehydrogenation. Appl Energy 2019;236:1034–48. https://doi.org/10.1016/j.apenergy.2018.12.038.

[126] Singh A, Tescari S, Lantin G, Agrafiotis C, Roeb M, Sattler C. Solar thermochemical heat storage via the Co_3O_4/CoO looping cycle: Storage reactor modelling and experimental validation. Sol Energy 2017;144:453–65. https://doi.org/10.1016/j.solener.2017.01.052.

[127] Zhou X, Mahmood M, Chen J, Yang T, Xiao G, Ferrari ML. Validated model of thermochemical energy storage based on cobalt oxides. Appl Therm Eng

2019;159:113965. https://doi.org/10.1016/j.applthermaleng.2019.113965.

[128] Tregambi C, Salatino P, Solimene R, Montagnaro F. An experimental characterization of Calcium Looping integrated with concentrated solar power. Chem Eng J 2018;331:794–802. https://doi.org/10.1016/j.cej.2017.08.068.

[129] Farcot L, Le Pierrès N, Fourmigué JF. Experimental investigation of a moving-bed heat storage thermochemical reactor with $SrBr_2/H_2O$ couple. J Energy Storage 2019;26:101009. https://doi.org/10.1016/j.est.2019.101009.

[130] Li W, Guo H, Zeng M, Wang Q. Performance of $SrBr_2 \cdot 6H_2O$ based seasonal thermochemical heat storage in a novel multilayered sieve reactor. Energy Convers Manag 2019;198:111843. https://doi.org/10.1016/j.enconman.2019.111843.

[131] Tregambi C, Montagnaro F, Salatino P, Solimene R. A model of integrated calcium looping for CO_2 capture and concentrated solar power. Sol Energy 2015;120:208–20. https://doi.org/10.1016/j.solener.2015.07.017.

[132] Pelay U, Luo L, Fan Y, Stitou D, Castelain C. Integration of a thermochemical energy storage system in a Rankine cycle driven by concentrating solar power: Energy and exergy analyses. Energy 2019;167:498–510. https://doi.org/10.1016/j.energy.2018.10.163.

[133] PELAY U, LUO L, FAN Y, STITOU D. Dynamic modeling and simulation of a concentrating solar power plant integrated with a thermochemical energy storage system. J Energy Storage 2020;28:101164. https://doi.org/10.1016/j.est.2019.101164.

[134] Rahbar K, Mahmoud S, Al-Dadah RK, Moazami N, Mirhadizadeh SA. Review of organic Rankine cycle for small-scale applications. Energy Convers Manag 2017;134:135–55. https://doi.org/10.1016/j.enconman.2016.12.023.

[135] Zhu Y, Li W, Li J, Li H, Wang Y, Li S. Thermodynamic analysis and economic assessment of biomass-fired organic Rankine cycle combined heat and power system integrated with CO_2 capture. Energy Convers Manag 2020;204:112310.

https://doi.org/10.1016/j.enconman.2019.112310.

[136] Li CY, Deethayat T, Wu JY, Kiatsiriroat T, Wang RZ. Simulation and evaluation of a biomass gasification-based combined cooling, heating, and power system integrated with an organic Rankine cycle. Energy 2018;158:238–55. https://doi.org/10.1016/j.energy.2018.05.206.

[137] Bayon A, Bader R, Jafarian M, Fedunik-Hofman L, Sun Y, Hinkley J, et al. Techno-economic assessment of solid–gas thermochemical energy storage systems for solar thermal power applications. Energy 2018;149:473–84. https://doi.org/10.1016/j.energy.2017.11.084.

[138] Pantaleo AM, Camporeale SM, Sorrentino A, Miliozzi A, Shah N, Markides CN. Hybrid solar-biomass combined Brayton/organic Rankine-cycle plants integrated with thermal storage: Techno-economic feasibility in selected Mediterranean areas. Renew Energy 2020;147:2913–31. https://doi.org/10.1016/j.renene.2018.08.022.

[139] Karapekmez A, Dincer I, Javani N. Development of a new integrated energy system with compressed air and heat storage options. J Energy Storage 2020;32:101955. https://doi.org/10.1016/j.est.2020.101955.

[140] Hussain CMI, Norton B, Duffy A. Comparison of hybridizing options for solar heat, biomass and heat storage for electricity generation in Spain. Energy Convers Manag 2020;222:113231. https://doi.org/10.1016/j.enconman.2020.113231.

[141] Stark M, Conti F, Saidi A, Zörner W, Greenough R. Steam storage systems for flexible biomass CHP plants - Evaluation and initial model based calculation. Biomass and Bioenergy 2019;128:105321. https://doi.org/10.1016/j.biombioe.2019.105321.

[142] Zhang X, Zeng R, Deng Q, Gu X, Liu H, He Y, et al. Energy, exergy and economic analysis of biomass and geothermal energy based CCHP system integrated with compressed air energy storage (CAES). Energy Convers Manag 2019;199:111953. https://doi.org/10.1016/j.enconman.2019.111953.

[143] Mahmoudi A, Fazli M, Morad MR. A recent review of waste heat recovery by Organic Rankine Cycle. Appl Therm Eng 2018;143:660–75. https://doi.org/10.1016/j.applthermaleng.2018.07.136.

[144] Fernández R, Ortiz C, Chacartegui R, Valverde JM, Becerra JA. Dispatchability of solar photovoltaics from thermochemical energy storage. Energy Convers Manag 2019;191:237–46. https://doi.org/10.1016/j.enconman.2019.03.074.

[145] Chacartegui R, Alovisio A, Ortiz C, Valverde JM, Verda V, Becerra JA. Thermochemical energy storage of concentrated solar power by integration of the calcium looping process and a CO_2 power cycle. Appl Energy 2016;173:589–605. https://doi.org/10.1016/j.apenergy.2016.04.053.

[146] Alovisio A, Chacartegui R, Ortiz C, Valverde JM, Verda V. Optimizing the CSP-Calcium Looping integration for Thermochemical Energy Storage. Energy Convers Manag 2017;136:85–98. https://doi.org/10.1016/j.enconman.2016.12.093.

[147] Ortiz C, Romano MC, Valverde JM, Binotti M, Chacartegui R. Process integration of Calcium-Looping thermochemical energy storage system in concentrating solar power plants. Energy 2018;155:535–51. https://doi.org/10.1016/j.energy.2018.04.180.

[148] Chen X, Zhang D, Wang Y, Ling X, Jin X. The role of sensible heat in a concentrated solar power plant with thermochemical energy storage. Energy Convers Manag 2019;190:42–53. https://doi.org/10.1016/j.enconman.2019.04.007.

[149] Ortiz C, Chacartegui R, Valverde JM, Alovisio A, Becerra JA. Power cycles integration in concentrated solar power plants with energy storage based on calcium looping. Energy Convers Manag 2017;149:815–29. https://doi.org/10.1016/j.enconman.2017.03.029.

[150] Tesio U, Guelpa E, Ortiz C, Chacartegui R, Verda V. Optimized synthesis/design of the carbonator side for direct integration of thermochemical energy storage in small size Concentrated Solar Power. Energy Convers Manag X 2019;4:100025.

https://doi.org/10.1016/j.ecmx.2019.100025.

[151] Wu S, Zhou C, Doroodchi E, Moghtaderi B. Thermodynamic analysis of a novel hybrid thermochemical-compressed air energy storage system powered by wind, solar and/or off-peak electricity. Energy Convers Manag 2019;180:1268–80. https://doi.org/10.1016/j.enconman.2018.11.063.

[152] Furusawa Y, Taguchi H, Ismail SN, Thangavel S, Matsuoka K, Fushimi C. Estimation of cold gas efficiency and reactor size of low-temperature gasifier for advanced-integrated coal gasification combined cycle systems. Fuel Process Technol 2019;193:304–16. https://doi.org/10.1016/j.fuproc.2019.05.023.

[153] Chemistry WebBook. NIST, https://webbook.nist.gov/chemistry/ (accessed November 27, 2020).

[154] Peter Atkins, Paula J de. Atkins' Physical Chemistry. 8th ed. Tokyo Kagaku Dojin; 2009.

[155] Yazaki M, Fushimi C. Estimation of CO_2 Reduction Potential and Cost of Solid Biomass Fuel Production Process Integrated with a Waste Gasification and Direct Melting System. Energy and Fuels 2020;34:9632–42. https://doi.org/10.1021/acs.energyfuels.0c01361.

[156] Fushimi C. Valorization of Biomass Power Generation System: Noble Use of Coombustion and Integration with Energy Storage. Energy & Fuels 2021;35:3715–3730. https://doi.org/10.1021/acs.energyfuels.0c04414.

[157] Sikarwar SS, Surywanshi GD, Patnaikuni VS, Kakunuri M, Vooradi R. Chemical looping combustion integrated Organic Rankine Cycled biomass-fired power plant – Energy and exergy analyses. Renew Energy 2020;155:931–49. https://doi.org/10.1016/j.renene.2020.03.114.

[158] Miura K. Kagaku Kogaku Binran. maruzen; 2011.

[159] Yoshida K. Heat Exchanger Handbook. The Energy Conservation Center, Japan; 2005.

[160] Flegkas S, Birkelbach F, Winter F, Groenewold H, Werner A. Profitability analysis and capital cost estimation of a thermochemical energy storage system utilizing fluidized bed reactors and the reaction system $MgO/Mg(OH)_2$. Energies 2019;12. https://doi.org/10.3390/en12244788.

[161] Peters MS, Timmerhaus KD, Carberry JJ, Wei J. Plant design and economics for chemical engineers. MCGraw-Hill; 1978.

[162] Turton R, C. Bailie R, B. Whiting W, A. Shaeiwitz J, Bhattacharyya D. Analysis, Synthesis, and Design of Chemical Processes. fourth. PEARSON EDUCATION INTERNATIONAL; 2013.

[163] Cost Indices. Towering Ski, https://www.toweringskills.com/financial-analysis/cost-indices/ (accessed May 7, 2022).

[164] Schmidt O, Melchior S, Hawkes A, Staffell I. Projecting the Future Levelized Cost of Electricity Storage Technologies. Joule 2019;3:81–100. https://doi.org/10.1016/j.joule.2018.12.008.

[165] Steckel T, Kendall A, Ambrose H. Applying levelized cost of storage methodology to utility-scale second-life lithium-ion battery energy storage systems. Appl Energy 2021;300:117309. https://doi.org/10.1016/j.apenergy.2021.117309.

[166] Li Z, Wang Q, Fang M, Luo Z. Thermodynamic and economic analysis of a new 600 MWe coal-fired power plant integrated with CaO-based carbon capture system. Int J Greenh Gas Control 2021;109:103386. https://doi.org/10.1016/j.ijggc.2021.103386.

[167] Product Directry. Made-in-China Connect Buyers with Chinese Suppliers, https://www.made-in-china.com/productdirectory.do?word=alumina+powder&file=&searchType=0&subaction=hunt&style=b&mode=and&code=0&comProvince=nolimit&order=0&isOpenCorrection=1&org=top (accessed February 1, 2022).

[168] Elshurafa AM. The value of storage in electricity generation: A qualitative and

quantitative review. J Energy Storage 2020;32:101872.

https://doi.org/10.1016/j.est.2020.101872.

List of Publications

I. Takayuki Uchino, Chihiro Fushimi, “Fluidized bed reactor for thermochemical heat storage using $Ca(OH)_2/CaO$ to absorb the fluctuations of electric power supplied by variable renewable energy sources: A dynamic model”, *Chemical Engineering Journal*, **419**, 129571, 2021

II. Takayuki Uchino, Takahito Yasui, Chihiro Fushimi, “Design of biomass power plant integrated with thermochemical heat storage using $Ca(OH)_2/CaO$ and evaluating the flexibility of power generation: Dynamic simulation and energy analysis”, *Energy Conversion and Management*, **243**, 114366, 2021

III. Takayuki Uchino, Takahito Yasui, Chihiro Fushimi, “Biomass power plant integrated with a thermochemical heat storage system using a fluidized bed reactor worked by variable renewable energy: Dynamic simulation, energetic and economic analyses”, *Journal of Energy Storage*, **61**, 106720, 2023

Conference Presentations

I. ○Takayuki Uchino, Chihiro Fushimi, “Dynamic model of a fluidized bed reactor for thermochemical heat storage of the electricity from variable renewable energy”, 26th SCEJ Symposium on Fluidization & Particle Processing, Nov. 26–27, 2020 (Gifu University, Online)

II. Takayuki UCHINO, ○Chihiro FUSHIMI, ”A dynamic model of fluidized bed reactor for thermochemical heat storage using $Ca(OH)_2/CaO$ to absorb the fluctuations of electric power supplied by variable renewable energy sources”, 8th Asia Particle Technology Symposium, APT 2021, Oct. 11, 2021, Osaka Japan (Online)

III. 内野貴行、○安井 崇人、伏見　千尋, “化学蓄熱プロセスを統合したバイオマス発電プラントの設計”, 第 52 回　化学工学会　秋季大会, 令和 3 年 9 月 22 日　岡山大学（in Japanese, online）

Acknowledgment

In April 2022, I returned to the Fushimi Lab. at Tokyo University of Agriculture and Technology as a Ph.D. student of Department of Chemical Engineering. Fortunately, I was able to complete the doctoral course early, while working full time at the company. I thank many people, especially, the following people.

For Dr. Chihiro Fushimi; Professor of Department of Chemical Engineering, I appreciate discussing the study and teaching me the many rules that contain not just technical information but also general knowledge regarding research and Ph.D. degree. From 2018 when I joined the Fushimi lab as an undergraduate student, to today, I can grow largely because of his education. In addition, I am grateful for his supports for my early graduation. I am looking forward to his future success.

For Professor. Yoshiyuki Yamashita, Professor. Akihiko Terada, Professor. Makoto Sakurai, and Professor. Hidenori Ohashi, I would like to acknowledge instructive comments and profitable discussion to this dissertation.

For the members of Fushimi laboratory; Mr. Ryu Ukawa-Sato, Mr. Kengo Fuji, Mr. Ryo Murakoshi, Ms. Masayo Koyama, Ms. Mana Yazaki, Mr. Kentaro Yato, Mr. Kenshiro Hasegawa, Ms. Nanami Hirano, Mr. Takahito Yasui, Mr. Masahiro Aoki, Mr. Ryota Kodate, Ms. Riho Okayama, Mr. Naoya Shirota, and Mr. Taiyo Suzuki, I am grateful for helpful advices. I also thank Dr. Yoshiko Yamamura and Ms. Kyoko Kawakatsu for their support for this study.

For two doctoral seniors; Dr. Hiromu Sasaki and Dr. Ryuta X. Suzuki, I am especially thankful for their advices and supports.

I would like to express my sincere gratitude to Ms. Eri Anai and Ms. Aiko Oishi for their great encouragement.

I appreciated the supports for my supervisor at the company that I work. I also appreciate the supports from my seniors; Mr. Masahiro Tanaka and Mr. Shuhei Kusunoki, and

my colleagues; Mr. Kento Iwama, Ms. Guo Lei, and Ms. Eri Takagi.

For my family, I appreciated their support over the years.

Takayuki UCHINO (March, 2023)